



**NEXT-TO-LEADING ORDER QCD
CORRECTIONS TO WJJ PRODUCTION
VIA VECTOR BOSON FUSION**

Master's Thesis of

Belinda Benz

at the
Department of Physics
Institute for Theoretical Physics

Reviewer: Prof. Dr. Dieter Zeppenfeld
Second Reviewer: Prof. Dr. Milada Margarete Mühlleitner

29 October 2018 – 24 October 2019

Declaration

I hereby declare that this thesis is my own work and effort and that it has not been submitted, in whole or in part, in any previous application for a degree. Where other sources of information have been used, they have been acknowledged as references.

Karlsruhe, 24 October 2019

Belinda Benz

“Das ewig Unbegreifliche an der Welt ist ihre Begreiflichkeit.”

ALBERT EINSTEIN

Contents

1	Introduction	1
2	Theoretical Framework	5
2.1	The Standard Model	5
2.1.1	Electroweak Sector	6
2.1.2	Quantum Chromodynamics	9
2.2	Perturbative Quantum Field Theory	11
2.3	Hadronic Cross Sections at NLO	15
2.3.1	Ultraviolet Divergences and Renormalisation	16
2.3.2	Infrared and Collinear Divergences	18
	Parton Evolution	19
	Dipole Subtraction Method	20
2.4	Vector Boson Fusion	22
3	Calculation and Implementation	25
3.1	VBFNLO	25
3.1.1	Monte Carlo Integration and Phase Space Generation	25
3.1.2	Program Structure and Operation	27
3.2	Leading Order	28
3.2.1	Electroweak Currents and Leptonic Tensors	30
3.2.2	Calculation of Matrix Elements	32
3.3	Real Emissions	34
3.3.1	Subprocesses with Two Gluons	34
3.3.2	Subprocesses with Six External Quarks	38
	Inclusion of Bottom Quarks	42
3.3.3	Dipole Subtraction Terms	42
3.4	Virtual Corrections	48
3.4.1	Subtraction of Infrared Singularities	51
3.5	Finite Collinears	52
4	Verification	55
4.1	Matrix Elements	55
4.1.1	Comparison of Matrix Elements with MADGRAPH	55
4.1.2	Virtual Correction Matrix Elements	56

4.2	Integrated LO Cross Section	57
4.3	Dipole Subtraction Terms	57
4.4	Influence of the Photon Virtuality Cut	62
5	Phenomenology	65
5.1	Cuts and Parameters	65
5.2	Differential Cross Section Distributions	67
5.3	Scale Variations	74
5.4	Comparison to H Production via VBF in Association with Three Jets	78
6	Summary	83
	Appendix	87
A	Selected Feynman Rules of the Standard Model	87
A.1	Electroweak Sector	87
A.2	Quantum Chromodynamics	90
B	Notation in Feynman Diagrams	93
C	Colour Factors for the Two-Gluon Subprocesses	95
	Bibliography	103

CHAPTER 1

Introduction

“If nature were not worth knowing, life would not be worth living.”
– Henri Poincaré, [1] –

Since thousands of generations the human mind strives to explain nature, steadily increasing the small amount of existing knowledge by understanding a part of the infinite unknown. “Today we still yearn to know why we are here and where we came from. [...] And our goal is nothing less than a complete description of the universe we live in” (Stephen Hawking, [2]). But we have come a long way since the early days of civilisation. Already over two thousand years ago, philosophers in China, India and Greece gave correct descriptions in mechanics, atomism and astronomy. But from then until the 19th century, when Dalton proposed his atomic theory [3], not much more insight into the deeper nature of matter has been gained.

Finally, in the 20th century, beginning with Rutherford’s scattering experiment [4], the discovery of the quantisation of light [5, 6] and the thereby triggered theory developments aiming to describe the inner structure of atoms and nuclei, particle physics was born. The discovery of many new particles in the 20th century, most of them observed in cosmic rays, raised the need for new theories in which electrons, protons and neutrons could no longer be the fundamental constituents of matter. The idea of quarks was introduced to explain the vast number of newly found baryons and mesons [7, 8]. The further study in the 1960s of the structure of the proton in deep inelastic scattering experiments lead to the parton model [9], which describes nucleons as made up of smaller constituents. Both observations were combined in form of a quantum field theory called Quantum Chromodynamics (QCD) [10]. In parallel, a theory was developed by Steven Weinberg and Abdus Salam [11, 12] which combines electromagnetic and weak interaction, until then described by the Fermi theory, to form the electroweak model. Both theories describing all three of strong, electromagnetic and weak interactions were combined to form the *Standard Model of Particle Physics*. Up to today the Standard Model is the most accurate theory of nature that is known, with all of its particle constituents having been experimentally observed and its predictions being in high agreement with experimental data (see e.g. Reference [13]).

Despite this success, the Standard Model is no complete theory to describe nature. For one thing it does not include gravity, the fourth fundamental force of nature. Gravity is described by General Relativity and could so far not be formulated as a quantum field theory, making it impossible to find a unified theory of all interactions. For another thing, the Standard Model lacks an explanation of cosmological phenomena such as baryon asymmetry and dark matter. The observed baryon asymmetry is much too large to be explained solely by the CP-violating mechanisms of the Standard Model. The second mentioned phenomenon, dark matter, was first proposed by Fritz Zwicky in order to hold galaxy clusters together, followed later on by more evidences observed in rotation curves of spiral galaxies, by gravitational lensing of the Bullet Cluster and in the Cosmic Microwave Background. In addition, if only ordinary baryonic matter would have driven structure formation in the universe, it could not have led to the structure of the sky as it is today. Besides these cosmological problems, the Standard Model suffers under what is called the hierarchy problem due to the small Higgs boson mass of 125 GeV. Theoretically, the Higgs mass is expected to have large quantum corrections that can only be cancelled by excessive fine-tuning in order to result in this small mass. Such a fine-tuning is however not seen as “natural” in physics [14, 15].

Every one of these puzzles drives the necessity to search for physics beyond the Standard Model. Besides proposing and directly searching for new particles, general limits on new physics or extensions of the Standard Model can be found by comparing data with Standard Model predictions. To be able to find significant discrepancies to the Standard Model, its predictions have to be known to very high accuracy. Because cross section calculations of the Standard Model are done perturbatively, higher corrections need to be taken into account for such precise calculations, especially for corrections with respect to the large strong coupling constant.

The most promising particle accelerator to gain the comparison data is the Large Hadron Collider (LHC) at CERN [16]. It has performed proton-proton collisions starting from 2008, having reached 13 TeV center-of-mass energy in its recent run from 2015 to 2018 (Run 2). At the time of this work being written it is paused in order to upgrade and replace damaged detector components in its experiments, amongst which are the ATLAS and CMS experiments [17]. It is planned to resume running from 2021 onwards with higher performance and a center-of-mass energy of 14 TeV. With this large center-of-mass energy the coming run is especially sensitive in phase space regions that are probed by the process classes *vector boson fusion* and *vector boson scattering*, characterised by two high energetic jets in the forward regions and reduced jet activity in the central region of the detector. Vector boson fusion and scattering processes contain interactions between three and four electroweak gauge bosons, making them well suited to probe the electroweak sector of the Standard Model.

The objective of this thesis is to make high precision predictions of the QCD next-to-leading order cross section of W boson production in association with three jets via vector boson fusion. This process has a comparably large cross section and thus a higher sensitivity in comparison to for example $Zjjj$ production, both being important background processes to

Higgs productions at the LHC. The calculation of the cross section is done by implementing the process in the flexible Monte Carlo program VBFNLO [18–21], which allows also for the addition of anomalous gauge couplings in order to analyse the effects of Effective Field Theory approaches.

Chapter 2 aims to recall and explain the fundamentals of perturbative quantum field theory after describing the two sectors of the Standard Model, including its interactions and particle content. In addition, problematic and necessary features of the calculation of hadronic cross sections up to next-to-leading order in perturbation theory are illustrated. Lastly in this chapter, vector boson fusion is explained in more detail.

The need for and principles of Monte Carlo methods for the simulation of hadronic cross sections are depicted in Chapter 3, before the actual calculation of W_{jjj} production for proton-proton as well as antiproton-antiproton collisions is performed. The calculation is split into leading order, real emissions and virtual corrections, with infrared divergences handled by dipole subtraction. The implementation is systematised in a way to remove all redundant steps, thereby assuring an as fast as possible and stable calculation.

The correctness of the calculation is validated in Chapter 4, where the results of various crosschecks verifying all steps of the implementation are presented. These include tests of the matrix elements, the integrated leading order cross section and the dipole subtraction terms.

The phenomenology of W_{jjj} production is discussed in Chapter 5. Specific differential cross section distributions are analysed and the scale dependences of the leading order in comparison to the next-to-leading order calculations are investigated. In addition, the QCD structure of W_{jjj} production is compared to H_{jjj} production via vector boson fusion.

At last, the calculation, results and conclusions are summarised in Chapter 6.

CHAPTER 2

Theoretical Framework

2.1 The Standard Model

The discovery of the Higgs boson in 2012 [22, 23] completed the experimental confirmation of all particle constituents of the *Standard Model of Particle Physics* (SM), which comprises three of the four fundamental forces of nature: the electromagnetic, the weak and the strong force. The SM is a relativistic quantum field theory based on the gauge group $SU(3)_C \times SU(2)_L \times U(1)_Y$. Besides the Higgs boson, the particle content of the SM can be split into gauge bosons, mediating the interactions, and fermions, which make up the matter content of the SM and themselves are divided into colour charged quarks and colourless leptons. All fermions included in the SM are subject to the electroweak interactions described by the $SU(2)_L \times U(1)_Y$ symmetry of the Glashow-Weinberg-Salam model [11, 12, 24]. Only the colour charged ones are additionally affected by Quantum Chromodynamics with its $SU(3)_C$ symmetry that describes strong interactions [8].

Table 2.1: Fermions of the Standard Model and their electroweak quantum numbers.

	Generation			Quantum numbers		
	1st	2nd	3rd	T_3	Y	Q
Leptons	$\begin{pmatrix} \nu_e \\ e^- \end{pmatrix}_L$	$\begin{pmatrix} \nu_\mu \\ \mu^- \end{pmatrix}_L$	$\begin{pmatrix} \nu_\tau \\ \tau^- \end{pmatrix}_L$	$+1/2$	-1	0
	e^-_R	μ^-_R	τ^-_R	$-1/2$	-1	-1
				0	-2	-1
Quarks	$\begin{pmatrix} u \\ d \end{pmatrix}_L$	$\begin{pmatrix} c \\ s \end{pmatrix}_L$	$\begin{pmatrix} t \\ b \end{pmatrix}_L$	$+1/2$	$+1/3$	$+2/3$
				$-1/2$	$+1/3$	$-1/3$
	u_R	c_R	t_R	0	$+4/3$	$+2/3$
	d_R	s_R	b_R	0	$-2/3$	$-1/3$

2.1.1 Electroweak Sector

The fermions of the SM, quarks and leptons, are grouped into three generations, as displayed in Table 2.1. For the quarks, every generation includes an up-type quark, namely up (u), charm (c) and top (t), and a down-type one, namely down (d), strange (s) and bottom (b). For each of these particles a corresponding antiparticle with quantum numbers of opposite sign and opposite handedness exists. All of them are chiral fermions, thus carrying spin $\frac{1}{2}$, with their left- and right-handed field components

$$\psi^{L, R} = \frac{1 \mp \gamma_5}{2} \psi \quad (2.1)$$

transforming differently under the $SU(2)_L$ of weak interactions. The left-handed fermions form doublets of the third component of the weak isospin T_3 , while the right-handed ones are singlets and do not couple to $SU(2)_L$ gauge fields. The hypercharge Y is the quantum number related to $U(1)_Y$ and together with T_3 gives an expression for the electric charge Q of a particle,

$$Q = T_3 + \frac{Y}{2}. \quad (2.2)$$

Since right-handed neutrinos are singlets under $SU(2)_L$ transformations and do not carry electric charge, thus also $Y = 0$, they, if existing, do not interact at all in the SM, which is why they are not included in Table 2.1. The generators of $SU(2)_L$, T^i , and of $U(1)_Y$, Y , correspond to three W_μ^i fields and one B_μ field, respectively, that mediate the interactions. A representation for the T^i are the Pauli matrices, $T^i = \frac{\sigma_i}{2}$, whose non-abelian nature causes the W_μ^i gauge fields to interact with themselves. With the covariant derivatives

$$D_\mu^L = \partial_\mu - igW_\mu^k \frac{\sigma^k}{2} - ig'B_\mu \frac{Y}{2} \quad \text{and} \quad (2.3)$$

$$D_\mu^R = \partial_\mu - ig'B_\mu \frac{Y}{2}, \quad (2.4)$$

acting on left-handed doublets Ψ^L and right-handed singlets ψ^R , respectively, the Lagrangian for these gauge fields, fermions and their interactions is

$$\mathcal{L}_{EW} = \bar{\Psi}_g^L i \not{D}^L \Psi_g^L + \bar{\psi}_f^R i \not{D}^R \psi_f^R - \frac{1}{4} W_{\mu\nu}^k W^{\mu\nu, k} - \frac{1}{4} B_{\mu\nu} B^{\mu\nu}, \quad (2.5)$$

with

$$W_{\mu\nu}^k = \partial_\mu W_\nu^k - \partial_\nu W_\mu^k - g\varepsilon^{kij} W_\mu^i W_\nu^j, \quad (2.6)$$

$$B_{\mu\nu} = \partial_\mu B_\nu - \partial_\nu B_\mu, \quad (2.7)$$

and coupling constants g and g' [25]. The implied sum over index g covers the six fermion generations, as two fermions of one generation (such as electron and electron neutrino or

up and down quarks) form a doublet, while the index f covers all fermions. The first two terms of the Lagrangian include the kinetic terms of the fermions and their interactions with the gauge bosons, while the other two terms give the self-interactions and kinetic terms of the gauge fields. Mass terms of the form

$$m\bar{\psi}\psi = m\left(\bar{\psi}^L\psi^R + \bar{\psi}^R\psi^L\right) \quad \text{and} \quad \frac{m_V^2}{2}V_\mu V^\mu \quad (2.8)$$

are not invariant under an $SU(2)_L$ transformation and would hence break gauge invariance if included in the Lagrangian. In order to still explain the observed massive fermions and gauge bosons, a mechanism of spontaneous symmetry breaking that generates massive gauge fields has been formulated independently by three groups in 1964 [26–29]. This nowadays called *Higgs mechanism* works by introducing a weak isospin doublet

$$\Phi = \begin{pmatrix} \phi_a \\ \phi_b \end{pmatrix}, \quad (2.9)$$

where ϕ_a and ϕ_b are scalar fields under Lorentz transformations and carry hypercharge $Y = 1$. Its Lagrangian

$$\mathcal{L}_H = (D^\mu\Phi)^\dagger (D_\mu\Phi) - \underbrace{\mu^2\Phi^\dagger\Phi - \lambda(\Phi^\dagger\Phi)^2}_{= -V(\Phi^\dagger\Phi)} \quad (2.10)$$

is invariant under $SU(2)_L \times U(1)_Y$ transformations. For $\mu^2 < 0$ and $\lambda > 0$, $V(\Phi^\dagger\Phi)$ takes the form of a mexican hat potential with its minimum at

$$\Phi_0^\dagger\Phi_0 = |\phi_a^0|^2 + |\phi_b^0|^2 = \frac{-\mu^2}{2\lambda} =: \frac{v^2}{2}. \quad (2.11)$$

By choosing without loss of generality

$$\Phi_0 = \begin{pmatrix} 0 \\ \frac{v}{\sqrt{2}} \end{pmatrix} \quad (2.12)$$

one can easily see that this ground state is no longer invariant under $SU(2)_L \times U(1)_Y$, which is called spontaneous symmetry breaking. As the charge of the component ϕ_a is $Q_a = 1$, whereas the one of component ϕ_b is $Q_b = 0$, spontaneous symmetry breaking occurs only in the electrically neutral component of Φ_0 , so the ground state is still invariant under $U(1)_{\text{em}}$ electromagnetic transformations. By expanding the field Φ around the vacuum expectation value and choosing unitary gauge,

$$\Phi = \begin{pmatrix} \phi_1 + i\phi_2 \\ \frac{1}{\sqrt{2}}(v + H) - i\phi_3 \end{pmatrix} \rightarrow \frac{1}{\sqrt{2}} \begin{pmatrix} 0 \\ v + H \end{pmatrix}, \quad (2.13)$$

only one of the formerly four degrees of freedom survives in the form of the physical Higgs field $H(x)$. Inserting this into the scalar field Lagrangian, the potential term gives a Higgs

mass term and Higgs self-couplings, while the kinetic term gives

$$\begin{aligned}\mathcal{L}_{\text{H,kin}} &= \frac{1}{2}(\partial_\mu H)^2 + \frac{1}{8}(v + H)^2 (g^2 (W_{1,\mu}^2 + W_{2,\mu}^2 + W_{3,\mu}^2) + g'^2 B_\mu^2 - 2g'gW_3^\mu B_\mu) \\ &= \frac{1}{2}(\partial_\mu H)^2 + \frac{1}{8}(v^2 + 2vH + H^2) \left(g^2 |W_\mu^-|^2 + g^2 |W_\mu^+|^2 + (g'^2 + g^2) |Z_\mu|^2 \right),\end{aligned}\tag{2.14}$$

with newly defined fields

$$W_\mu^\mp := \frac{1}{\sqrt{2}} (W_{1,\mu} \pm iW_{2,\mu}) \quad \text{and} \quad Z_\mu := c_w W_{3,\mu} - s_w B_\mu,\tag{2.15}$$

where the Weinberg angle θ_w is defined by

$$c_w := \cos \theta_w := \frac{g}{\sqrt{g'^2 + g^2}}, \quad s_w := \sin \theta_w := \frac{g'}{\sqrt{g'^2 + g^2}}.\tag{2.16}$$

The v^2 terms in Equation 2.14 now yield masses for these new fields, namely

$$m_W = \frac{vg}{2} \quad \text{and} \quad m_Z = \frac{vg}{2c_w}.\tag{2.17}$$

The fourth linear independent field

$$A_\mu := s_w W_{3,\mu} + c_w B_\mu,\tag{2.18}$$

the photon, remains massless and does not directly interact with the Higgs field.

Hence, the masses of the weak bosons W^\pm and Z can be incorporated in the theory. Fermion masses on the other hand do not result from spontaneous symmetry breaking, but are introduced via Yukawa couplings of fermion fields with Φ . This leads to a mixing between fermion generations, causing mass eigenstates to differ from weak interaction eigenstates, which is parametrised in the CKM matrix. Since fermion masses (except for the top quark) are neglected here, CKM mixing is irrelevant for the calculations done in this thesis.

By inverting Equations 2.15 and 2.18 for the fields $W_{i,\mu}$ and B_μ , inserting them into the Lagrangian of electroweak interactions of Equation 2.5, and applying the covariant derivatives with correct hypercharge values Y for the specific fields, the interactions between the new fields with fermions as well as with themselves can be seen directly (see Appendix A). To identify the basic properties of the couplings it is enough to consider the leptonic interaction terms,

which take the form

$$\begin{aligned}
\mathcal{L}_{\text{EW,LI}} &= -g' c_w \bar{\psi}_l \not{A} \psi_l - \frac{g}{2c_w} \bar{\psi}_l \not{Z} (1 - 2s_w^2) \psi_l + g' s_w \bar{\psi}_l \not{Z} \psi_l^{\text{R}} \\
&\quad + \frac{g}{2c_w} \bar{\psi}_{\nu_l} \not{Z} \psi_{\nu_l}^{\text{L}} + \frac{g\sqrt{2}}{2} \left(\bar{\psi}_l \not{W}^- \psi_{\nu_l}^{\text{L}} + \bar{\psi}_{\nu_l} \not{W}^+ \psi_l^{\text{L}} \right) \\
&= -g' c_w \bar{\psi}_l \not{A} \psi_l - \frac{g}{4c_w} \bar{\psi}_l \not{Z} (1 - \gamma_5 - 4s_w^2) \psi_l \\
&\quad + \frac{g}{4c_w} \bar{\psi}_{\nu_l} \not{Z} (1 - \gamma_5) \psi_{\nu_l} + \frac{g}{2\sqrt{2}} \left(\bar{\psi}_l \not{W}^- (1 - \gamma_5) \psi_{\nu_l} + \bar{\psi}_{\nu_l} \not{W}^+ (1 - \gamma_5) \psi_l \right),
\end{aligned} \tag{2.19}$$

with $l = e, \mu, \tau$. The first term can be identified with the electromagnetic interaction and defines the elementary charge $e := g' c_w$. The second and third term are the interactions with the Z boson, while the last terms describe the W boson interactions. These terms directly show the imbalance in handedness causing parity violation in weak interactions, as the W boson only couples to the left-handed field components and the Z boson couples differently to left- and right-handed ones.

2.1.2 Quantum Chromodynamics

The discovery of many new hadrons in the mid of the 20th century that could not all be thought of as new fundamental particles, as well as the results of deep inelastic scattering of electrons and protons led to the introduction of quarks as constituents of hadrons [7–9]. In order to further explain the existence of particles like the Δ^{++} , that would formerly have disagreed with the Pauli exclusion principle, a new quantum number, the colour charge, and with this an additional $\text{SU}(3)_C$ symmetry for quarks was introduced [30]. Out of this, *Quantum Chromodynamics* (QCD) [10] was developed, in which quarks form triplets $\psi = (\psi_r \ \psi_g \ \psi_b)^T$ under $\text{SU}(3)_C$, while leptons do not participate in strong interactions and thus are singlets. The eight generators t^a of $\text{SU}(3)_C$ give rise to eight gauge boson fields A_μ^a , the gluons, which themselves carry colour charges. In the fundamental representation of $\text{SU}(3)$, under which the quarks transform, the generators are given by the Gell-Mann matrices, $t^a = \frac{\lambda^a}{2}$, $a = 1, \dots, 8$, and satisfy the relations

$$\text{Tr} \left(t^a t^b \right) = T_R \delta^{ab}, \quad \left[t^a, t^b \right] = i f^{abc} t^c, \quad \text{and} \quad t_{ij}^a t_{kl}^a = T_R \left(\delta_{il} \delta_{jk} - \frac{1}{N} \delta_{ij} \delta_{kl} \right), \tag{2.20}$$

with $N = 3$, $T_R = \frac{1}{2}$, and totally antisymmetric structure constants f^{abc} . The non-vanishing commutator of the generators makes QCD a non-abelian field theory. The Casimir invariant of the fundamental representation is given by

$$C_F = t^a t^a = \frac{N^2 - 1}{2N} = \frac{4}{3}. \tag{2.21}$$

The gluon fields transform under the adjoint representation of $\text{SU}(3)$, whose generators are proportional to the structure constants f^{abc} , giving the Casimir invariant of the adjoint

representation

$$C_A = N = 3, \quad (2.22)$$

and an identity relating Casimir operators of fundamental and adjoint representation,

$$t^a t^b t^a = \left(C_F - \frac{C_A}{2} \right) t^b. \quad (2.23)$$

With the quark triplets Ψ , the covariant derivative

$$D_\mu = \partial_\mu - ig_s t^a A_\mu^a \quad (2.24)$$

with strong coupling constant g_s , and the gluon field strength tensor

$$\begin{aligned} G_{\mu\nu} &= \frac{i}{g_s} [D_\mu, D_\nu] = t^a (\partial_\mu A_\nu^a - \partial_\nu A_\mu^a) - ig \left[t^b A_\mu^b, t^c A_\nu^c \right] \\ &= t^a \left(\partial_\mu A_\nu^a - \partial_\nu A_\mu^a + gf^{abc} A_\mu^b A_\nu^c \right) \\ &= t^a G_{\mu\nu}^a, \end{aligned} \quad (2.25)$$

the Lagrangian of QCD reads [25]

$$\mathcal{L}_{\text{QCD}} = \underbrace{\sum_{\text{quarks } q} \bar{\Psi}_q (i\not{D} - m_q) \Psi_q}_{= \mathcal{L}_{\text{quarks}}} - \underbrace{\frac{1}{4} G_{\mu\nu}^a G^{a,\mu\nu}}_{= \mathcal{L}_{\text{gauge}}}. \quad (2.26)$$

In practice, an additional gauge fixing term \mathcal{L}_{fix} proportional to $(\partial^\mu A_\mu^a)^2$ is added to the Lagrangian, as it does not change the equations of motion but makes the theory quantizable. This is the case for all gauge theories, also the electroweak one above. In addition, another term $\mathcal{L}_{\text{ghost}}$ is needed in non-abelian gauge theories (which is the case both for QCD and weak interactions) to compensate unphysical degrees of freedom, which shall not be explained here further as it is irrelevant for the calculation of this thesis. Interested readers are referred to textbooks on quantum field theory like References [31] and [32]. The additional gauge fixing and ghost terms can be examined as parts of the full gauge invariant and quantizable QCD Lagrangian in Appendix A, but are not explained here in further detail.

2.2 Perturbative Quantum Field Theory

For some readers, the preceding section may have raised two important questions. One is how these Lagrangian densities and symmetry groups that describe Nature have been constructed, the other how experimentally measurable quantities and predictions can be obtained from these, which is certainly necessary for the verification¹ or disproof of the theory. The answers to both questions lie in quantum field theory, which makes use of a computational framework based on the Lagrange and Hamilton formalisms to gain mathematical rules for describing the interactions and propagation of particles from only a Lagrangian density, and with these rules to be able to calculate measurable quantities, such as cross sections. The other question can then be answered similarly, because for known interactions and particles as well as completely new, unobserved particles a Lagrangian can be built (or guessed) which then through the framework of quantum field theory produces observable results. In the following, a short overview over the method of perturbative quantum field theory is given.

The Lagrangian of a quantum field theory can be written as a free Lagrangian (including mass terms and gauge terms) and an interaction Lagrangian, including all terms containing three or more fields,²

$$L = L_0 + L_{\text{int}}. \quad (2.27)$$

The interaction Hamiltonian of the theory is given by

$$H_{\text{int}} = -L_{\text{int}} = - \int d^3x \mathcal{L}_{\text{int}}. \quad (2.28)$$

The equations of motion resulting from the *free* Lagrangian can easily be solved using second quantization to give the free fields

$$\phi(x) = \int \frac{d^3p}{(2\pi)^3 2\omega_p} (a_p e^{-ip \cdot x} + a_p^\dagger e^{ip \cdot x}) \quad (2.29)$$

as a linear combination of creation and annihilation operators. However, most *interacting* field theories are not exactly solvable [31, p. 81], raising the need for approximation methods like perturbation theory. In perturbation theory, the interaction Hamiltonian is treated as a small quantity and thus an expansion can be made. The interacting vacuum Ω and the interacting fields ϕ can be expressed in terms of the free vacuum, the fields in the interaction picture ϕ_I , which have the same form as the free fields in Equation 2.29, and the time evolution operator $U(t, t_0)$. The correlation function of two fields can then be

¹ Or rather “survival”, since no theory can ever be truly verified.

² In quantum field theory, particles are seen as excitations of their respective fields.

brought to the form [31, p. 87]

$$\langle \Omega | T \{ \phi(x) \phi(y) \} | \Omega \rangle = \lim_{t \rightarrow \infty (1-i\epsilon)} \frac{\langle 0 | T \left\{ \phi_I(x) \phi_I(y) \exp \left[-i \int_{-T}^T dt H_I(t) \right] \right\} | 0 \rangle}{\langle 0 | T \left\{ \exp \left[-i \int_{-T}^T dt H_I(t) \right] \right\} | 0 \rangle}, \quad (2.30)$$

with the interaction Hamiltonian H_I given in the interaction picture and $T \{ \dots \}$ implying the time-ordered product of the included fields. Since H_I only consists of fields and a coupling constant λ , the numerator gives a series expansion in λ whose terms are correlation functions of two and more free fields. Using Wick's theorem [33], these can be reduced to time ordered two-point correlation functions of free fields, called *Feynman propagators*, that are Green's functions of the fields' equations of motion. Every term in the expansion thus gives a set of Feynman propagators multiplied by factors of λ , which can be illustrated in Feynman diagrams. The order of the expansion, i.e. the order of λ , gives the number of vertices in this diagram. Diagrams without ending points are cancelled out by the denominator in Equation 2.30.

The last step to make this formalism applicable to scattering processes, and thus the theory experimentally tangible, is to relate these correlation functions of the fields ϕ_I to the amplitudes between incoming and outgoing states in scattering experiments, i.e. to S-matrix elements

$$S_{fi} = {}_{\text{out}} \langle q_1 \dots q_m | p_1 \dots p_n \rangle_{\text{in}} = \langle \Omega | a_{\text{out}}(\vec{q}_1) \dots a_{\text{out}}(\vec{q}_m) a_{\text{in}}^\dagger(\vec{p}_1) \dots a_{\text{in}}^\dagger(\vec{p}_n) | \Omega \rangle \quad (2.31)$$

for n initial and m final state particles. The in- and out-states can be described as one-particle states created by asymptotically free fields in the limit of times long before and long after the interaction, respectively. More explicitly, an in-state is basically a momentum eigenstate created by the full interacting field ϕ from the interacting vacuum Ω and projected on the subspace of one-particle states of the full interacting theory. For the calculation of S-matrix elements however, it is enough to use a weaker relation between $\phi_{\text{in}}(x)$ and $\phi_{\text{out}}(x)$ and the full interacting field $\phi(x)$ in the limit of far past or far future times,

$$\begin{aligned} \langle f | \phi(x) | i \rangle &\xrightarrow{t \rightarrow -\infty} \sqrt{Z} \langle f | \phi_{\text{in}}(x) | i \rangle, \\ \langle f | \phi(x) | i \rangle &\xrightarrow{t \rightarrow \infty} \sqrt{Z} \langle f | \phi_{\text{out}}(x) | i \rangle, \end{aligned} \quad (2.32)$$

where Z is the field strength renormalization.¹ By expressing the creation operator in terms of the field, it is *inside an S-matrix element* possible to write, for the example of

¹ For further information on field strength renormalization and the relation between in-, out- and interacting fields, see text books such as Reference [31].

scalar fields (where free field operators satisfy the Klein-Gordon Equation),

$$\begin{aligned}
a_{\text{out}}^\dagger(\vec{p}) - a_{\text{in}}^\dagger(\vec{p}) &= -i \left(\int d^3\vec{x} e^{-ip\cdot x} \overset{\leftrightarrow}{\partial}_0 \phi_{\text{out}}(x) - \int d^3\vec{x} e^{-ip\cdot x} \overset{\leftrightarrow}{\partial}_0 \phi_{\text{in}}(x) \right) \\
&= \frac{-i}{\sqrt{Z}} \left(\lim_{t \rightarrow \infty} \int d^3\vec{x} e^{-ip\cdot x} \overset{\leftrightarrow}{\partial}_0 \phi_{\text{out}}(x) - \lim_{t \rightarrow -\infty} \int d^3\vec{x} e^{-ip\cdot x} \overset{\leftrightarrow}{\partial}_0 \phi_{\text{in}}(x) \right) \\
&= \frac{-i}{\sqrt{Z}} \int d^4x \partial_0 \left(e^{-ip\cdot x} \overset{\leftrightarrow}{\partial}_0 \phi(x) \right) \\
&= \frac{-i}{\sqrt{Z}} \int d^4x e^{-ip\cdot x} (\partial_0^2 + \omega_p^2) \phi(x) \\
&= \frac{-i}{\sqrt{Z}} \int d^4x e^{-ip\cdot x} (\square + m^2) \phi(x),
\end{aligned} \tag{2.33}$$

where $A \overset{\leftrightarrow}{\partial}_0 B := B(\partial_0 A) - (\partial_0 A)B$ and in the last step $\omega_p^2 = \vec{p}^2 + m^2$ was used followed by two integrations by parts. Using this identity, one a_{in}^\dagger in Equation 2.31 can be replaced by a_{out}^\dagger and a term containing the interacting field $\phi(x)$. The operator a_{out}^\dagger can be permuted to the left to annihilate the vacuum. The commutators give Delta functions and S-matrix elements of $n - 1$ to $m - 1$ particles. These terms are called *disconnected* and do not need to be considered here. By replacing another a_{in}^\dagger , the field $\phi(x)$ now needs to permute with a_{out}^\dagger before this operator can be permuted further left. This can be done using

$$\phi(x) a_{\text{in}}^\dagger(\vec{q}) - a_{\text{out}}^\dagger(\vec{q}) \phi(x) = \frac{i}{\sqrt{Z}} \int d^4y e^{-iq\cdot y} (\square_y + m^2) T \{ \phi(x) \phi(y) \}. \tag{2.34}$$

By further reduction the connected term is in the end given by the *LSZ reduction formula* [34], which for scalar fields reads

$$\begin{aligned}
\{ \text{out} \langle q_1 \dots q_m | p_1 \dots p_n \rangle_{\text{in}} \}_{\text{connected}} &= \left(\frac{i}{\sqrt{Z}} \right)^{n+m} \left[\prod_{j=1}^m \int d^4x_j e^{iq_j \cdot x_j} (\square_{x_j} + m^2) \right] \\
&\cdot \left[\prod_{i=1}^n \int d^4y_i e^{ip_i \cdot y_i} (\square_{y_i} + m^2) \right] \langle \Omega | T \{ \phi(x_1) \dots \phi(x_m) \phi(y_1) \dots \phi(y_n) \} | \Omega \rangle. \tag{2.35}
\end{aligned}$$

All in all that means that S-matrix elements can be expressed by time ordered Green's functions of the interacting theory, which themselves reduce to vacuum expectation values of time ordered free field operators. Every order in perturbation theory of a process can separately be illustrated as Feynman diagrams, with external lines for incoming and outgoing particles, propagators for internal particles and vertices. Feynman rules, which result from the procedure explained above, make it possible to calculate each Feynman diagram of an interacting theory with the same scheme. Selected Feynman rules of electroweak

interactions and QCD are given in Appendix A.¹ From here on, the term *matrix elements* is used for the elements \mathcal{M} resulting from Feynman diagrams using Feynman rules and not containing the overall momentum conservation, which are then related to the total S-matrix element by

$$S = \mathbb{1} + iT, \quad \text{with} \quad \langle f|T|i\rangle := (2\pi)^4 \delta^{(4)}\left(\sum p_f - \sum p_i\right) \mathcal{M}(\{p_f\} \rightarrow \{p_i\}). \quad (2.36)$$

Diagrams involving the smallest possible power of the coupling constant λ for a given process give the *leading order*, LO. The *next-to-leading order*, NLO, is the one with next non-vanishing order of λ , and so on.

Figure 2.1 shows Bhaba scattering, which is electron-positron scattering, at leading order (a) and selected diagrams contributing to its next-to-leading order (b) in Quantum Electrodynamics (QED). For $n \rightarrow n$ processes in QED, terms proportional to odd factors of $\lambda_{\text{QED}} = e$ vanish in the expansion, so the coupling constant normally used in QED is $\alpha_e := e^2/(4\pi)$. There are only two diagrams contributing to Moeller scattering at leading order, which is then proportional to α_e . They are called tree-level diagrams, as they do not include loops. The next-to-leading order diagrams contain loops in the form of vacuum polarisation of the photon, vertex corrections, and box diagrams.

In experiments, it is impossible to detect arbitrarily soft photons or collinear particles and thus specify the final state of a process completely. This necessitates the inclusion of *real emission contributions* to the cross section. For NLO cross section calculations of a process with $n \rightarrow m$ particles, this means to include the tree-level diagrams of the

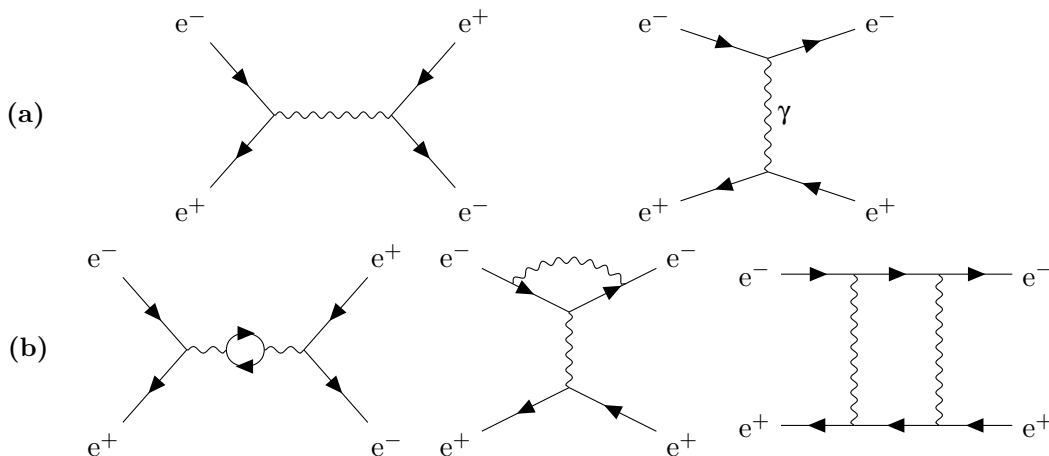


Figure 2.1: All diagrams contributing to Bhaba scattering at LO (a) and some virtual correction diagrams (b).

¹ Especially in the case of QCD, another formalism, path integral quantisation, is needed to obtain the Feynman rules because of its non-abelian nature. See again textbooks such as Reference [31].

process $n \rightarrow m + 1$. These have the same order of the coupling constant as the one-loop virtual corrections, since (for an example where the leading order is of order λ^0 and the loop diagrams, including two more vertices, therefore of order λ^2)

$$|\mathcal{M}_m|^2 = |\mathcal{M}_{\text{LO}} + \mathcal{M}_{1\text{-loop}} + \mathcal{O}(\lambda^4)|^2 = |\mathcal{M}_{\text{LO}}|^2 + 2 \cdot \text{Re}(\mathcal{M}_{\text{LO}}^* \cdot \mathcal{M}_{1\text{-loop}}) + \mathcal{O}(\lambda^4), \quad (2.37)$$

and the real emissions, which include one more vertex than the leading order, give

$$|\mathcal{M}_{m+1}|^2 = |\mathcal{M}_{\text{R}} + \mathcal{O}(\lambda^3)|^2 = |\mathcal{M}_{\text{R}}|^2 + \mathcal{O}(\lambda^4). \quad (2.38)$$

In this work, the process of W boson production via vector boson fusion in association with three jets, which is a $2 \rightarrow 5$ process if including the decay of the W boson, is considered. At leading order it contains one QCD and four electroweak vertices. As the electroweak coupling constants g and $\alpha_e = \frac{1}{137}$ are much weaker than the strong coupling constant $\alpha_s := g_s^2/(4\pi) = 0.1181$ (at the scale of the Z boson mass) [35], the QCD corrections are in general dominating, which is why only these are included for the NLO calculation in this thesis.

2.3 Hadronic Cross Sections at NLO

So far only the calculation of matrix elements contributing to the amplitude of a process $n \rightarrow m$ has been discussed. In order to find the differential cross section, which is a measure for the probability for this explicit process to happen, the amplitude has to be multiplied by a flux factor and the *Lorentz-invariant phase space measure* $d\Phi_m$. For a $2 \rightarrow m$ scattering process with initial momenta q_1 and q_2 it is given by

$$d\hat{\sigma}_{2 \rightarrow m} = \frac{1}{4\sqrt{(q_1 \cdot q_2)^2 - m_1^2 m_2^2}} \overline{\sum} |\mathcal{M}|^2 \cdot \underbrace{\prod_{f=1}^m \frac{d^3 p_f}{(2\pi)^3 2E_f} (2\pi)^4 \delta^{(4)} \left(\sum p_f - \sum p_i \right)}_{= d\Phi_m}. \quad (2.39)$$

Since the particles' polarisations and colour charges are generally not prepared or measured in experiments, the total squared matrix element $|\mathcal{M}|^2$ is averaged over incoming and summed over outgoing polarisations and colour charges, which is denoted above as $\overline{\sum} |\mathcal{M}|^2$, to give the unpolarised cross section. In hadronic scattering processes, the elementary particles involved in the scattering, gluons or quarks, called partons, carry only a fraction of the full hadron momentum P . In the approximation of massless partons, the flux factor can be written as $1/(2\hat{s})$, with the squared center-of-mass energy of the two interacting partons \hat{s} given by

$$\hat{s} = (q_1 + q_2)^2 = 2q_1 \cdot q_2 = x_1 x_2 2 \cdot P_1 \cdot P_2 = x_1 x_2 s, \quad (2.40)$$

where x denotes the fraction of the hadron momentum carried by the parton and s is the total squared center-of-mass energy of the hadrons. The probability to find a parton a with momentum fraction x in the hadron with momentum P is given by the *parton distribution*

function (PDF) $f_{a/P}(x)$. In order to get the full cross section for the hadronic scattering process, the differential cross sections of all possible subprocesses that give the wanted final state have to be integrated over phase space, folded with PDFs, and summed, giving

$$\begin{aligned}\sigma(\text{pp} \rightarrow \text{X}) &= \int d\sigma(\text{pp} \rightarrow \text{X}) \\ &= \sum_{\substack{a,b \\ \text{sub-} \\ \text{proc.}}} \int_0^1 dx_1 \int_0^1 dx_2 f_{a/P_1}(x_1) f_{b/P_2}(x_2) \int d\hat{\sigma}(ab \rightarrow \text{X})\end{aligned}\quad (2.41)$$

for the example of a proton-proton scattering process resulting in a final state observable X. Here, a and b can mean all quark types or gluons if the resulting combination gives a possible subprocess for this final state.

For a calculation up to next-to-leading order, the cross section can be split into contributions from the differential cross section in the Born approximation $d\sigma^{\text{B}}$, which corresponds to the leading order cross section, the virtual corrections $d\sigma^{\text{V}}$ containing the interference term of the Born and one-loop diagrams in Equation 2.37, and the real emission differential cross section $d\sigma^{\text{R}}$ with $m + 1$ final state particles, reading

$$\sigma = \sigma_{\text{LO}} + \sigma_{\text{NLO}} = \int_m d\sigma^{\text{B}} + \int_m d\sigma^{\text{V}} + \int_{m+1} d\sigma^{\text{R}}. \quad (2.42)$$

2.3.1 Ultraviolet Divergences and Renormalisation

During the NLO calculation, singularities appear that have to be handled to get a finite result for the cross section. In the virtual corrections, these originate from the integration over the loop momentum k , which is of the form

$$\int d^4k \frac{k^{\mu_1} \dots k^{\mu_h}}{D_0 \dots D_{n-1}}, \quad D_j := \left(k + \sum_{i=1}^j \pm p_i \right)^2 - m_j^2, \quad (2.43)$$

with p_i being the in- or outgoing momenta (coming with a + or – sign, respectively) of the n external particles coupling to the loop, h the number of fermions in the loop, and m_j the masses of the internal loop particles. If some of these are zero, the mass singularities appearing in the integration for low values of k give infrared divergences that cancel with the real emissions, which will be explained in Section 2.3.2. From the integration over k up to infinity further ultraviolet divergences arise when the numerator of the integrand contains too much powers of k (when $h > 2n - 4$).

To handle these divergences, the loop integrals are regulated to separate finite and divergent parts. A convenient method to do this is dimensional regularisation, where the dimension of spacetime is continued from 4 to $d = 4 - 2\varepsilon$ dimensions during the calculation [36]. The singularities then manifest as poles in ε . Further, as physical observables are always finite

and measurable, the idea is that the parameters of the Lagrangian, such as masses and coupling constants, are bare quantities that are neither observable nor finite. To get a finite, measurable result, these bare quantities, from now on called m_0 , λ_0 , ϕ_0 , etc., are expressed by renormalised quantities m , λ , ϕ , and so on. By expressing the Lagrangian in these quantities, counterterms appear that absorb the infinite but unobservable shifts between bare and renormalised quantities. In this way new Feynman diagrams appear, whose amplitudes can be calculated as functions of the shifting parameters. Using renormalisation conditions at a specific momentum scale, called renormalisation scale μ_R , these are adjusted to give finite amplitudes that are independent of the choice of the regularisation procedure. This procedure to eliminate ultraviolet divergences by a redefinition of parameters is called renormalisation.

There are several renormalisation schemes, for example on-shell renormalisation, where two renormalisation conditions are given by the specification that the renormalised mass m of a particle is the pole of its propagator with residue one, meaning the physical mass of the particle. Another often used scheme is the minimal subtraction scheme, where the counterterms are chosen in a way to exactly cancel the divergent poles in ε appearing after dimensional regularisation, but all remaining finite terms are kept. Independent of the scheme, the renormalisation scale can be chosen arbitrarily, which is why physical, observable quantities must be independent of the choice of this scale. This is equivalent to Green's functions remaining fixed under a shift in μ_R , where Green's functions

$$G^{(n)}(x_1, \dots, x_n) = \langle \Omega | T \{ \phi(x_1) \dots \phi(x_n) \} | \Omega \rangle, \quad (2.44)$$

can be thought of as functions of the renormalisation scale μ_R , coupling constant λ , and particle mass m . As a consequence, there have to be compensating shifts in the renormalized coupling constant, mass and also field strength. For a massless theory, this leads to the Callan-Symanzik equation [37, 38],

$$\left[\mu_R \frac{\partial}{\partial \mu_R} + \beta(\lambda) \frac{\partial}{\partial \lambda} + n\gamma(\lambda) \right] G^{(n)}(\{x_i\}; \mu_R, \lambda) = 0, \quad (2.45)$$

with functions $\beta(\lambda) = \mu_R \cdot d\lambda/d\mu_R$ and $\gamma(\lambda)$ corresponding to the shifts in coupling constant and field strength, respectively. This equation can be solved for the coupling constant as a function of the scale μ_R .

Because of this so-called running of the coupling constant, the choice of the scale μ_R , although arbitrary, affects the precision of the result of a cross section calculation up to a specific order. In the loop corrections at NLO and higher orders, logarithms appear that get large if μ_R is not chosen reasonably. To justify a perturbational approach, these logarithms need to be kept small, which is done by adjusting the scale μ_R to the process energy. This is most important for leading order calculations, where the scale only enters in the scale dependent coupling constant. By choosing μ_R too far off the process energy, perturbation theory loses its accuracy, which is why the calculation only up to LO gets highly unprecise. In the calculation of hadronic cross sections, the fraction of the total

energy involved for the specific considered process is mostly not known exactly. In addition, however reasonable the renormalisation scale is chosen, the error of a calculation up to a specific order due to the missing orders of perturbation theory cannot be eliminated completely by a rational choice of the scale. The scope of this error can however very roughly be estimated by analysing the variation of the cross section with the scale. The error and thus also the scale uncertainties reduce accordingly by including higher-order corrections to the cross section.

The exact dependence of the coupling constant on the energy scale can be found by rewriting Equation 2.45 for Fourier transformed Green's functions of rescaled momenta and solving the resulting differential equation for λ by using the β -function. The evolution of the strong coupling of QCD up to one-loop is then given by [32]

$$\alpha_s(Q^2) = \frac{\alpha_s(\mu_0^2)}{1 + \frac{\alpha_s(\mu_R^2)}{4\pi} \left(\frac{11}{3}N - \frac{4}{3}n_f T_R \right) \ln \frac{Q^2}{\mu_R^2}}, \quad (2.46)$$

with n_f being the number of quark flavours contributing at energy scale Q^2 and μ_R being the renormalisation scale. This formula comprises two kinds of behaviour of strong interactions, known as asymptotic freedom and confinement. For large energies, the coupling approaches zero, which was experimentally discovered in deep inelastic scattering experiments where partons as constituents of hadrons behave like free particles. On the other hand, the coupling diverges for low energies, preventing the use of perturbation theory in this region. As a consequence, colour charged particles cannot be isolated, since their spatial separation leads to new quark-antiquark pairs being produced. In scattering experiments this manifests in the form of parton showers and hadronisation.

2.3.2 Infrared and Collinear Divergences

With the ultraviolet divergences regularised, there are still singularities to be handled during the NLO calculation appearing in the low momentum region. When an effectively massless particle of small momentum k is emitted from a fermion line or gluon, the propagator before emission behaves as

$$\frac{1}{(p^\mu - k^\mu)^2 - m^2} \xrightarrow{k \rightarrow 0} \infty, \quad (2.47)$$

where p and m are the momentum and mass of the on-shell particle after emitting the soft particle. If the emitter is also a massless particle, the propagator diverges not only if a soft particle is emitted, but for any k that obeys $k \parallel p$, since

$$\frac{1}{(p^\mu - k^\mu)^2} = \frac{1}{-2p \cdot k} = \frac{1}{-2|\vec{p}||\vec{k}|(1 - \cos \theta)} \xrightarrow{\theta \rightarrow 0} \infty. \quad (2.48)$$

Such soft and collinear divergences appear both in the virtual corrections and in the real emission part of the cross section. Kinoshita and Lee/Nauenberg independently showed

that by summing over all degenerate states, that means over virtual corrections, real emissions and absorptions, these soft and collinear divergences cancel out completely at all orders of perturbation theory (KLN theorem) [39, 40].

In QCD the use of perturbation theory is justified only for short-distance interactions because of asymptotic freedom (see Section 2.3.1). However, real emissions can take place in the whole range of a detector. In order to still use the KLN theorem to cancel infrared singularities, only so-called infrared safe observables are considered, meaning observables that are independent of the number of collinear and soft particles in the final state and thus do not depend on long distance physics. The fully inclusive cross section for example is such a quantity. For infrared safe quantities, the sum over all final state configurations is taken to cancel soft and collinear final state singularities. If partons appear in the initial state, there are additional collinear initial state singularities that do not cancel, but can be factorized into splitting functions and absorbed in the PDFs.

Parton Evolution

Partons as constituents of hadrons are confined in bound states. In this low energy range the strong coupling is very large, so that no perturbative calculation of the PDFs is possible. Instead, they are obtained by fitting experimental data. In the early days of deep inelastic scattering experiments, James Bjorken proposed that the structure functions of nucleons are only dependent on the momentum fraction x of the parton and not on the energy scale of the scattering, which is called Bjorken scaling [9]. However, further experiments showed a violation of this scaling behaviour, meaning a dependence on the energy scale, of the structure functions. This scaling violation could be explained with the introduction of QCD, since it originates from the above mentioned additional collinear singularities appearing in higher order corrections to cross sections with initial state partons.

From the viewpoint of a perturbative higher-order calculation of a partonic cross section, an incoming quark can itself, when resolved to very small scales, be seen as a quark constituent along with further gluons and quark-antiquark pairs, all of which carry a specific momentum fraction and can enter a so-called *hard* scattering process [31]. Singularities arising from the collinear emission of initial partons are thus associated with their PDFs and not the hard scattering cross section. This, however, makes the PDFs dependent on the momentum scale of the hard scattering process. In contrast to the PDFs themselves, their evolution with momentum scale can be determined perturbatively and is given by the DGLAP equations [41–43]. The momentum scale at which the PDFs $f_{a/P} = f_{a/P}(x, \mu_F)$ are evaluated is called the *factorisation scale* μ_F and qualitatively marks the edge between *soft* long-distance and *hard* short-distance physics. Analogously to the renormalisation scale μ_R it is an unphysical scale in the sense that all observables are independent of this scale. The sum of all orders of perturbation theory should thus be independent of both the renormalisation and factorisation scale. However, just as the renormalisation scale the factorisation scale can be chosen in a rational way to reduce the error of a calculation only up to a specific order in perturbation theory. If the considered process has a specific momentum scale Q , this would be a rational choice for both scales.

Dipole Subtraction Method

The left infrared and collinear final state divergences cancel according to the KLN theorem when taking the sum over all contributions to the cross section. In analytic calculations, this sum can be taken before phase space integration to cancel the singularities at the integrand level.

For Monte Carlo techniques this is not possible, because real emission and virtual contributions are calculated and integrated separately and numerically. A solution for numerical calculations is to subtract a local counterterm $d\sigma^A$ from the real emission differential cross section $d\sigma^R$, which matches its singular behaviour in d dimensions. This counterterm should furthermore be analytically integrable over the one additional subspace of the $(m+1)$ -process to give a contribution proportional to the Born matrix elements which contains poles that exactly cancel the ones of the virtual contribution. As a result, ε can be set to zero in both integrals of

$$\sigma^{\text{NLO}} = \int_{m+1} \left[\left(d\sigma^R \right)_{\varepsilon=0} - \left(d\sigma^A \right)_{\varepsilon=0} \right] + \int_m \left[d\sigma^V + \int_1 d\sigma^A \right]_{\varepsilon=0}, \quad (2.49)$$

which can then be integrated numerically over four-dimensional phase space by Monte Carlo integration [44].

Catani and Seymour show in Reference [44] that the subtraction term $d\sigma^A$ can be constructed with process independent dipole factors dV_{dipole} , symbolically written as

$$d\sigma^A = \sum_{\text{dipoles}} d\sigma^B \otimes dV_{\text{dipole}}. \quad (2.50)$$

The operation \otimes denotes a properly defined phase space convolution of a colour and spin projection of the Born cross section with the universal factors dV_{dipole} . With the insertion operator

$$\mathcal{J} = \sum_{\text{dipoles}} \int_1 dV_{\text{dipole}} \quad (2.51)$$

the NLO part of a cross section without initial hadrons can be written in the form

$$\sigma^{\text{NLO}} = \int_{m+1} \left[d\sigma^R - \sum_{\text{dipoles}} d\sigma^B \otimes dV_{\text{dipole}} \right] + \int_m \left[d\sigma^V + d\sigma^B \otimes \mathcal{J} \right]. \quad (2.52)$$

As mentioned above, the additional initial state singularities for a process with incoming partons are factorised and absorbed in a redefinition of the process-independent PDFs. The finite terms that remain after cancelling all infrared and collinear divergences are

summarised in the finite collinear remainder $d\sigma^C$. Then the NLO cross section gets

$$\begin{aligned}
\sigma^{\text{NLO}} &= \int_{m+1} d\sigma^{\text{R}} + \int_m d\sigma^{\text{V}} + \int_m d\sigma^{\text{C}} \\
&= \sum_{a,b} \int_0^1 dx_1 \int_0^1 dx_2 f_{a/P_1}(x_1, \mu_{\text{F}}) f_{b/P_2}(x_2, \mu_{\text{F}}) \\
&\quad \cdot \left[\int_{m+1} \left(d\hat{\sigma}_{a,b}^{\text{R}} - \sum_{\text{dipoles}} d\hat{\sigma}_{a,b}^{\text{B}} \otimes \left[dV_{\text{dipole}}^{a,b} + d\tilde{V}_{\text{dipole}}^{a,b} \right] \right) \right. \\
&\quad \left. + \int_m \left(d\hat{\sigma}_{a,b}^{\text{V}} + d\hat{\sigma}_{a,b}^{\text{B}} \otimes \mathcal{J} \right) + \int_m \int dz \left(d\hat{\sigma}^{\text{B}} \otimes [\mathcal{P}(z) + \mathcal{K}(z)] \right)_{a,b} \right], \tag{2.53}
\end{aligned}$$

where a and b denote the initial state partons of the partonic subprocesses. The term $d\tilde{V}_{\text{dipole}}$ includes the dipole terms corresponding to initial-final collinearity, while dV_{dipole} includes the soft and collinear final state dipole splittings. The construction of the specific dipole subtraction terms is explained in Section 3.3.3, where they are needed to subtract the singularities in the real emission amplitudes. The integral over the dipole splittings does not depend on the specific kind of subprocesses, meaning it has the same structure for processes with only final hadrons, one initial hadron or two initial hadrons. It is given by the insertion operator, which itself can be written universally as [44]

$$\mathcal{J}(\{p\}; \varepsilon) = -\frac{\alpha_s}{2\pi} \frac{1}{\Gamma(1-\varepsilon)} \sum_I \frac{1}{\mathbf{T}_I^2} \mathcal{V}_I(\varepsilon) \sum_{J \neq I} \mathbf{T}_I \mathbf{T}_J \left(\frac{4\pi\mu}{2p_I \cdot p_J} \right)^\varepsilon, \tag{2.54}$$

with indices I and J running over all partons (initial and final). In dimensional regularisation, the functions \mathcal{V}_I are given by

$$\mathcal{V}_I(\varepsilon) = \mathbf{T}_I^2 \left(\frac{1}{\varepsilon^2} - \frac{\pi^2}{3} \right) + \gamma_I \frac{1}{\varepsilon} + \gamma_I + K_I + \mathcal{O}(\varepsilon), \tag{2.55}$$

with constants γ_I and K_I depending on the particle being a quark/antiquark or a gluon,

$$\gamma_{\text{q}} = \gamma_{\bar{\text{q}}} = \frac{3}{2} C_{\text{F}}, \quad \gamma_{\text{g}} = \frac{11}{6} C_{\text{A}} - \frac{2}{3} T_{\text{R}} n_f, \tag{2.56}$$

and

$$K_{\text{q}} = K_{\bar{\text{q}}} = \left(\frac{7}{2} - \frac{\pi^2}{6} \right) C_{\text{F}}, \quad K_{\text{g}} = \left(\frac{67}{18} - \frac{\pi^2}{6} \right) C_{\text{A}} - \frac{10}{9} T_{\text{R}} n_f, \tag{2.57}$$

with the number of quark flavours n_f . The operator \mathbf{T}_I is a colour-charge operator of

parton I , defined as in Reference [44] and satisfying

$$\mathbf{T}_I \cdot \mathbf{T}_J = \mathbf{T}_J \cdot \mathbf{T}_I, \quad \mathbf{T}_I^2 = C_I, \quad \sum_{I,J} \mathbf{T}_I \mathbf{T}_J = 0, \quad (2.58)$$

with $C_I = C_A$ for gluons and $C_I = C_F$ for quarks and antiquarks. The third relation follows directly from colour conservation, $\sum_I \mathbf{T}_I = 0$. The calculation and application of the insertion operator to cancel infrared divergences of the virtual correction amplitudes is explained in detail in Section 3.4.1, as are the finite collinear remainder terms including the operators \mathcal{P} and \mathcal{K} in Section 3.5.

2.4 Vector Boson Fusion

In *Vector Boson Fusion* (VBF) processes, an electroweak gauge boson (W , Z or γ) is exchanged between a pair of quarks, antiquarks or a quark and an antiquark, which then emits another gauge boson or Higgs particle. To produce a W boson via vector boson fusion, the two quark lines have to radiate different kinds of bosons, one neutral Z boson or photon and one W boson, that fuse to a charged W boson, as in Figure 2.2(a). By also considering the leptonic decay of the W boson, non-resonant diagrams as in Figure 2.2(c), with the same final state signature but no intermediate boson, also contribute. These as well as diagrams like the one in Figure 2.2(b), where the final state boson is emitted from one of the quark legs, need to be included in a calculation in addition to the “true” VBF diagrams in order to preserve gauge invariance. All of these diagrams resemble an electroweak t -channel exchange, with the Mandelstam variables for a $2 \rightarrow 2$ process with incoming momenta p_1 and p_2 and outgoing momenta p_3 and p_4 defined as

$$\begin{aligned} s &= (p_1 + p_2)^2, \\ t &= (p_3 - p_1)^2, \\ u &= (p_4 - p_1)^2, \end{aligned} \quad (2.59)$$

see also Figure 2.3. In the VBF approximation, s -channel diagrams giving the same final state are neglected by reasoning that these contributions are highly suppressed in phase space regions where VBF processes are observed. These regions are characterised by two

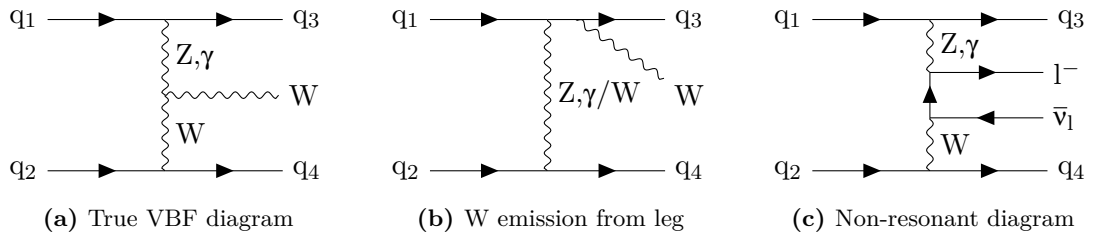


Figure 2.2: Some example diagrams contributing to W boson production via vector boson fusion.

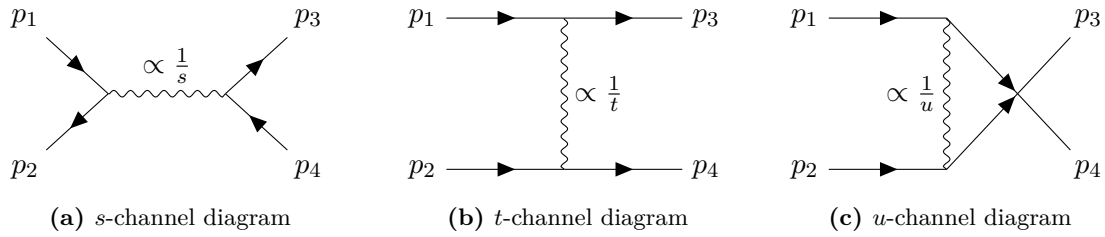


Figure 2.3: The three different channels for a $2 \rightarrow 2$ process defining the Mandelstam variables s , t and u .

high-energetic, widely rapidity separated final jets, called tagging jets, and a reduced jet activity in the central region. In addition, interferences between t - and u -channel diagrams are neglected because of colour suppression, meaning the interference terms are suppressed by a factor of $1/N = 1/3$, since only quarks with identical colour give a non-zero interference term. The justification of these approximations is demonstrated in Reference [45] exemplary for the process $pp \rightarrow Wjj/Zjj$.

CHAPTER 3

Calculation and Implementation

This chapter presents the calculation of W production in association with three jets via vector boson fusion up to NLO in α_s . The processes W^-jjj and W^+jjj are handled in parallel, as they are highly similar to each other. Both have been implemented in the parton-level Monte Carlo program VBFNLO [18–21], whose general structure and performance is described in Section 3.1. Subsequently, the calculation and implementation of the LO process of $Wjjj$ is explained first before the real emission and virtual correction contributions are depicted in detail.

3.1 VBFNLO

VBFNLO [18–21] provides simulations of vector boson fusion as well as double and triple vector boson production in collisions of proton and/or antiproton beams at QCD NLO with up to three additional jets. The program includes beyond the Standard Model physics, for example anomalous couplings, and is fully flexible in respect to the possibility of choosing between different scales, set individual cuts, and select from all available PDF sets. Another benefit of VBFNLO is its speed, which arises to some extent from the precalculation of reusable parts of matrix elements, which is explained in detail for the special case of $Wjjj$ in Section 3.2. The VBF approximations mentioned in Section 2.4 further simplify the calculations in VBFNLO, as besides neglecting the interference of t - and u -channel diagrams no loops connecting both quark lines are considered for the NLO calculations. Additionally, quark masses are approximated by zero. Since this approximation is not valid for top quarks, they are not considered in VBFNLO, and bottom quarks are only included in processes where no top quark can appear in an intermediate state.

3.1.1 Monte Carlo Integration and Phase Space Generation

The total cross section formula for a $pp \rightarrow X$ process as in Equation 2.41 has to be modified with the application of cuts to

$$\sigma = \sum_{\substack{\text{sub-} \\ \text{proc.}}} \int_0^1 dx_1 \int_0^1 dx_2 f_{a/P_1}(x_1) f_{b/P_2}(x_2) \frac{1}{2\hat{s}} \int d\Phi_m \Theta_{\text{cuts}} \overline{\sum |\mathcal{M}_{ab}|^2}. \quad (3.1)$$

Besides the difficulties due to the high dimensional integral and the unavailability of analytic PDFs, the cuts Θ -function makes it in general impossible to solve these integrals analytically and a naive direct numerical integration would be highly time consuming. In VBFNLO, the integration is performed numerically via Monte Carlo integration. The idea, adapted from Reference [46], is to express the integral of the integrand function $f(\vec{x})$ over the n -dimensional volume Ω as

$$I = \int_{\Omega} d^n \vec{x} f(\vec{x}) = \int_{\Omega} d^n \vec{x} \frac{f(\vec{x})}{g(\vec{x})} g(\vec{x}), \quad (3.2)$$

where $g(\vec{x})$ is a normalised distribution function of points in Ω ,

$$\int_{\Omega} d^n \vec{x} g(\vec{x}) = 1. \quad (3.3)$$

By choosing M points $\vec{x}_i \in \Omega$ according to this distribution, the integral I can be approximated by

$$I_M = \frac{1}{M} \sum_{i=1}^M \frac{f(\vec{x}_i)}{g(\vec{x}_i)}. \quad (3.4)$$

which converges to I in the limit of $M \rightarrow \infty$. The error of this estimate,

$$\delta_{\text{MC}}^2 = \frac{1}{M(M-1)} \left[\sum_{i=1}^M \frac{f^2(\vec{x}_i)}{g^2(\vec{x}_i)} - \frac{1}{M} \left(\sum_{i=1}^M \frac{f(\vec{x}_i)}{g(\vec{x}_i)} \right)^2 \right], \quad (3.5)$$

is independent of the dimension of the integration, making Monte Carlo integration especially convenient for high dimensional phase space integrals.

Importance sampling further reduces the error by choosing the random points according to a distribution $g(\vec{x})$ that resembles the integrand $f(\vec{x})$, causing more points to be chosen in regions where f is large. In VBFNLO this is done by *Monaco*, an algorithm based on VEGAS [46]. It performs the integration in several iterations, factorising the distributions $g(\vec{x})$ in step functions, called grids, $g_j(x_j)$ for each dimension j ,

$$g(\vec{x}) = \prod_{j=1}^n g_j(x_j). \quad (3.6)$$

For each step in the g_j the same number of sampling points is chosen. In the first iteration, all grids are chosen uniformly, meaning that the steps of g_j have the same width. During each iteration, the integrand values at the sampled points are written in histograms to be used to adjust the boundaries of the grid steps and thus the $g_j(x_j)$ for the next iteration.

In addition to the importance sampling done by *Monaco*, VBFNLO contains phase space generators for the various classes of implemented processes. These use knowledge about the

shape of resonances in the amplitudes, such as Breit-Wigner resonances for the propagators of massive gauge bosons, in order to convert the random numbers x_i in a sensible way to external particle momenta.

3.1.2 Program Structure and Operation

VBFNLO is written in FORTRAN and has a modular structure, containing various subroutines calculating for example bras, kets, and currents, that can be used in all amplitude calculations. Before running the program, desired parameters for the calculation can be set in input files, such as physics parameters, cuts and anomalous couplings, as well as adjustments for the output in form of histograms, root files etc. The file **vbfno.dat** contains general regulations for the calculation, which besides the selection of the process to calculate are switches for LO or NLO, selection of final state leptons and the number of phase space points and Monte Carlo iterations that shall be performed.

The main routine of VBFNLO reads these parameters when being executed, before initialising the phase space for the chosen process, the random number generator *Monaco* and the histograms. The program then starts with the first Monte Carlo iteration and converts the first generated random number vector \vec{x} to the momenta of the external particles. The routine *cuts* then checks if this produced phase space point passes the cut criteria, or if it is skipped to continue with the next random number vector. If it passes, the factorisation and renormalisation scales μ_F and μ_R for this point in phase space are calculated, before the function *Amplitude* is called. Here, the actual calculation of the squared matrix element $|\mathcal{M}|^2$ for the requested process is called. This is described in detail in the following sections for the Wjjj process. After this calculation, the amplitude $|\mathcal{M}|^2$ is multiplied by the phase space factor before being returned to the integration and added to the previous calculated amplitudes at different phase space points. In the last iteration, the results of each phase space point are written in histograms and the total cross section including errors is returned. Details about the histograms that are to be created can be defined and changed in the file **histograms.F**. The whole operation flow is shown in compact form in Figure 3.1.

In the case of an NLO calculation, separate calculations are done for the virtual contribution and real emission cross section, for which a separate phase space is constructed. For the virtual corrections the grid of the last LO iteration is used as starting Monte Carlo grid, while the real emission calculation needs to perform separate iterations beginning again with a uniform starting grid due to the differing phase space. It is also possible in VBFNLO to only calculate real emission amplitudes, which resemble the LO of a process containing one additional jet.

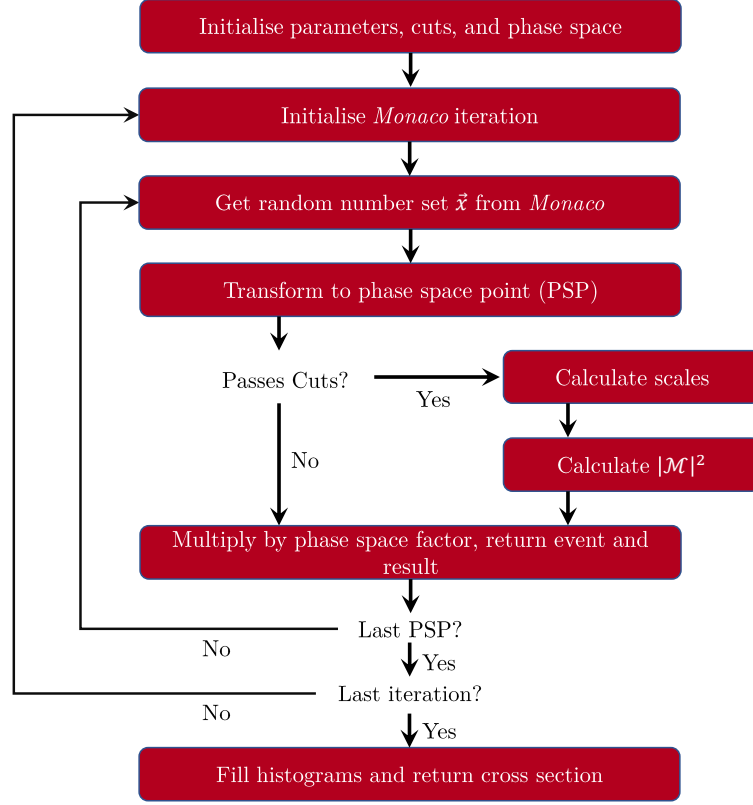


Figure 3.1: Schematic diagram of the operation sequence in VBFNLO [partially adapted from 47, p. 24].

3.2 Leading Order

The considered process of two partons interacting via vector boson fusion to give the final state observable $Wjjj$ – three jets in addition to a lepton-antineutrino pair for the case of W^- and an antilepton and corresponding neutrino for the case of W^+ , to be precise – is at Born level of electroweak order α_e^4 including the leptonic decay of the W boson and of order α_s in respect to strong interactions. There are several subprocesses that contribute to the overall process, each given by a different constellation of the five involved partons, four of which are quarks and one is a gluon. These subprocesses are related to each other via crossing symmetry. In VBFNLO, the matrix element calculation is implemented for the subprocess

$$q_1(\tilde{p}_1) q_2(\tilde{p}_2) \rightarrow q_3(\tilde{p}_3) q_4(\tilde{p}_4) g(\tilde{p}_5) W(p_W). \quad (3.7)$$

All other subprocesses are calculated by mapping the physical momenta of the particles to the momenta used in the calculation following the formalism of Reference [48]; so for example for the crossing $g(p_1) q_2(p_2) \rightarrow q_3(p_3) \bar{q}_1(p_5) q_4(p_4) W(p_W)$, the incoming physical momentum p_1 is assigned to the gluon, which has outgoing momentum \tilde{p}_5 during the

calculation, so \tilde{p}_5 is set to $-p_1$.

In the VBF approximation, there is no interference between t - and u -channel diagrams and no s -channel diagrams are included. This is realised in the calculation by considering the two quark lines as belonging to different colour algebras, under which the quarks of the opposite line transform as singlets. Thus, diagrams with gluon emitted on the upper quark line, that is to quark q_1 or q_3 (thus this line will also be denoted line q_1q_3), have to be treated separately and the resulting matrix elements have to be squared before being added to the squared matrix elements of the process with gluon emitted on the lower quark line (also denoted line q_2q_4). As of now, diagrams with the gluon coupling to the upper quark line are referred to as *colour structure 1 (cs1) diagrams*, while diagrams with gluon coupled to the lower line are called *colour structure 2 diagrams*. The quarks belonging to the lower line colour algebra will be denoted by upper case letters.

The number of subprocesses contributing to a process of two initial and three final state partons thus reduces to eight in the VBF approximation. In Figure 3.2 the subprocesses that have contributions from cs1 diagrams are shown. The subprocesses (a), (b) and (d), (e) (with no initial gluon) also exist for cs2, while (c) and (f) do not. There are two subprocesses only existing in colour structure 2, which are similar to (c) and (f), but with an initial gluon coupled to the lower line instead of the upper one. Since the amplitudes are integrated over phase space, the inclusion of a subprocess with \bar{q}_1 and q_3 switched in Figures 3.2(c) and (f) would be double counting.

For the W_{jjj} process, the possible subprocesses on the parton level are identical, with the addition of a W observable in the final state. The only possible flavour combinations in

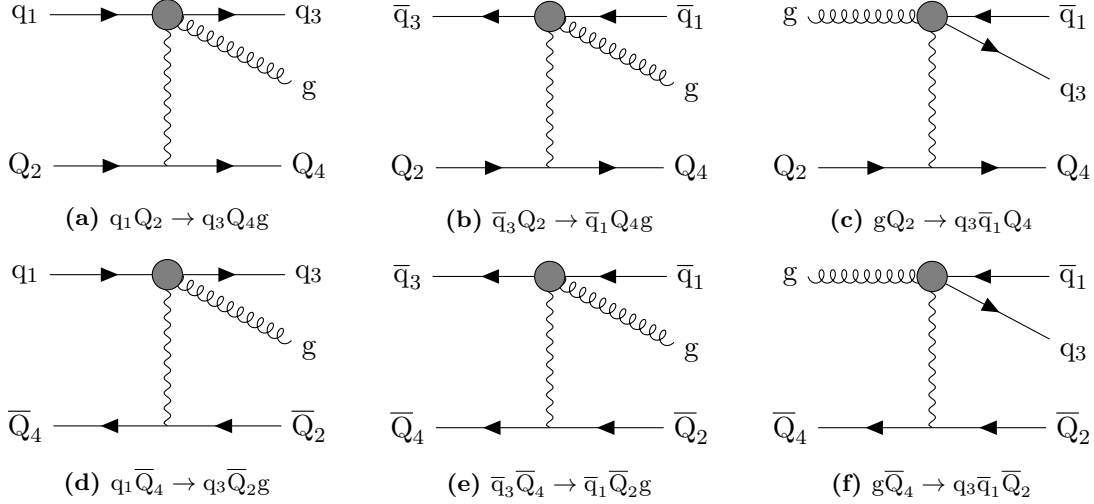


Figure 3.2: All subprocesses that have contributions from colour structure 1. The grey circle indicates that the order of the couplings in this circle is irrelevant, so there are diagrams where the quark line couples to the electroweak current before emitting the gluon and also ones where the gluon is emitted before the line couples to the current. This is part of the notation explained in Appendix B.

the chosen crossing of Equation 3.7 giving this final state are

$$\begin{array}{ll}
 W^- \text{jjj} & W^+ \text{jjj} \\
 d D \rightarrow d U g l^- \bar{\nu}_1, & u U \rightarrow u D g l^+ \nu_1, \\
 u D \rightarrow u U g l^- \bar{\nu}_1, & d U \rightarrow d D g l^+ \nu_1, \\
 d D \rightarrow u D g l^- \bar{\nu}_1, & u U \rightarrow d U g l^+ \nu_1, \\
 d U \rightarrow u U g l^- \bar{\nu}_1, & u D \rightarrow d D g l^+ \nu_1.
 \end{array} \tag{3.8}$$

Here, u/U can be replaced by all up-type quarks except top quarks, and similarly d/D by all down-type ones except for bottom quarks. Yet, as CKM mixing is neglected, quarks of one line belong to the same generation. The matrix elements themselves do not depend on the generation of the involved quarks, so the calculation is implemented only for up and down quarks.

3.2.1 Electroweak Currents and Leptonic Tensors

The W final state observable, (anti-)lepton and (anti-)neutrino, can be produced in two general ways, classifying the diagrams contributing to the process in two groups:

- Emission from one quark leg, as in Figure 2.2(b) for Wjj, and decay \rightarrow diagrams with an *effective polarisation vector*.
- True VBF, as in Figure 2.2(a), and direct lepton-neutrino production, as in Figure 2.2(c) \rightarrow *leptonic tensor* diagrams.

As mentioned in Section 2.4, all of these diagrams have to be included to preserve gauge invariance. In detail, the terms of the boson propagators proportional to $(1 - \xi)k^\mu k^\nu / k^2$ with gauge parameter ξ cancel only by including all of the mentioned diagrams. By thus including them all, only the propagator terms proportional to $g^{\mu\nu}$ have to be implemented in the calculation, since the gauge-dependent ones would eventually cancel anyway.

In any case the intermediate state W boson can have off-shell momentum. The first production mechanism can additionally be split into two categories depending on the kind of electroweak current that is exchanged between the quark lines. For each flavour combination the process contains *neutral current* (NC) diagrams with Z boson or photon exchange, *charged current* (CC) diagrams with W boson exchange, and leptonic tensor (LT) diagrams. The position of the W boson emission depends on the flavour combination and on the type of current. In NC diagrams, the W boson is emitted from the line that changes flavour, while in CC diagrams, it can only be emitted either before or after the emission of the current of the line not changing flavour, depending on the flavour of this line and the kind of W boson considered. Figures 3.3(a) and (b) show the possible NC and CC diagrams for the flavour combination $u D \rightarrow u U g W^-$, with the gluon, which can be emitted from every position on both quark lines, omitted for simplicity. Since the NC can consist either of a Z boson or of a photon, and considering all five different positions

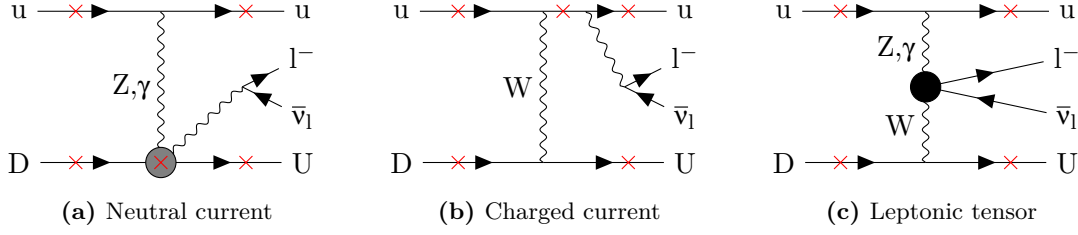


Figure 3.3: Diagrams for the flavour combination $uD \rightarrow uU g l^- \bar{\nu}_l$. The final state gluon is omitted for simplicity, as it can be emitted on each external quark leg or internal quark propagator, which is indicated with red crosses. The grey circle is explained in Appendix B.

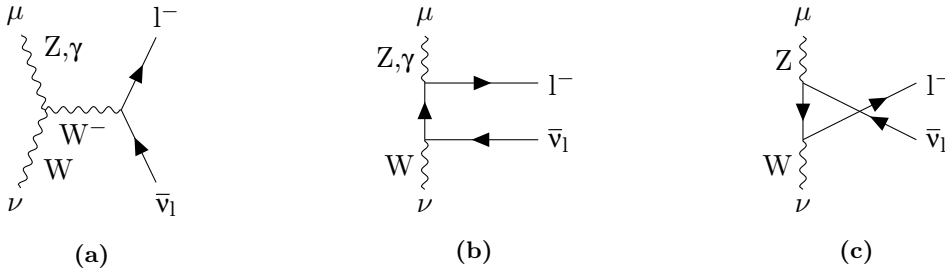


Figure 3.4: Leptonic tensors $\mathcal{L}^{\mu\nu}$ that produce the W^- final state observable. The first two exist for both neutral bosons, the third only for a Z boson.

for gluon emission, there are in total 20 NC and five CC diagrams for this single flavour combination.

Figure 3.3(c) combines the five (times four for the possible position of gluon emission) additional LT diagrams, with leptonic tensor symbolized by the black circle. The five explicit leptonic tensors are shown in Figure 3.4, where (c) only exists for Z bosons, as photons do not couple to the intermediate neutrino propagator.

In VBFNLO, the effective polarisation vector and all leptonic tensors are calculated with HELAS (HELicity Amplitude Subroutines for feynman diagram evaluations)[49]. These are implemented in FORTRAN77 and include routines to compute incoming and outgoing wavefunctions of fermions and vector bosons for fixed helicities, as well as three-particle amplitudes. A subroutine not included in HELAS, but of similar construction, is VCARTX, which computes an effective vector wavefunction for an internal vector boson including its propagator. This routine is especially needed for the leptonic tensor calculation.

The effective polarisation vector and leptonic tensors are the same for all subprocesses and are thus calculated only once per phase space point, which reduces the computing time significantly. While the effective polarisation vector only depends on the momenta of the decaying leptons, the leptonic tensors are calculated for all possible momentum configurations. These are the two possible momentum flows corresponding to the two colour structures, and the two directions corresponding to the position of the flavour changing line.

3.2.2 Calculation of Matrix Elements

The total squared matrix element for a specific flavour combination is given by the average over incoming particles' and sum over outgoing particles' polarisations and colours,

$$\overline{|\mathcal{M}|^2} = \frac{1}{4} f_c \sum_a \sum_{i,j,k} \sum_{s_1,s_2} \sum_{\lambda} |\mathcal{M}_{s_1,s_2,\lambda,i,j,k,a}|^2 \quad (3.9)$$

where $\lambda = 0, 1$ is the gluon polarisation, $s_1, s_2 = -1, 1$ and $i, j, k = 1, \dots, N$ the helicities and colour charges of the quarks, respectively, and $a = 1, \dots, N^2 - 1$ the gluon colour charge. Since quark helicities of the same line are preserved, as is the colour charge of the line not coupling to the gluon, the sums over the missing two final state helicities and one colour charge were eliminated by Kronecker deltas. The factor f_c depends on the incoming particles, since the colour charge average over two incoming quarks gives a factor of $f_c = 1/N^2$, whereas $f_c = 1/(N(N^2 - 1))$ if the incoming particles are a gluon and a quark. All diagrams contain a gluon-fermion vertex proportional to $-ig_s t_{ji}^a$, which in the squared matrix element sum gives a factor of

$$(t_{ji}^a)^* t_{ji}^a = (t_{ij}^a)^\dagger t_{ji}^a = \text{Tr}(t^a t^a) = \frac{N^2 - 1}{2} = C_F N, \quad (3.10)$$

multiplied by the coupling factor $g_s^2 = 4\pi\alpha_s$, which is calculated at a constant or dynamic scale. The left colour charge sum over k only gives an additional factor of N , as the diagrams for different colour charges of the gluon-disconnected line give identical results. In addition, the cs1 and cs2 diagrams do not interfere, so the total squared matrix element can be expressed as

$$\overline{|\mathcal{M}|^2} = \pi\alpha_s C_F N^2 f_c \sum_{s_1,s_2,\lambda} \left(|\mathcal{M}_{s_1,s_2,\lambda}^{\text{cs1}}|^2 + |\mathcal{M}_{s_1,s_2,\lambda}^{\text{cs2}}|^2 \right). \quad (3.11)$$

The $\mathcal{M}_{s_1,s_2,\lambda}^{\text{cs1}}$ themselves contain the sum of all diagrams with gluon emitted from line q1q3, meaning NC, CC, and LT diagrams, for a specific helicity and polarisation combination. Their computation is simplified by computing the currents of upper and lower line \mathcal{J}^1 and \mathcal{J}^2 , respectively, and combining them with the exchanged current or the pre-calculated leptonic tensor. In this way, a large amount of computation time can be saved, because many diagrams share the same currents. Specific factors, such as propagators and couplings for different flavours, can be multiplied in the end. The matrix elements for cs1 can thus be expressed with flavour combination index j and position of gluon emission i as

$$\mathcal{M}_j^{\text{cs1}} = g_V \mathcal{D}_V^{\mu\nu} \mathcal{J}_\nu^2 \sum_{i,l} \mathcal{J}_\mu^{1,i,l} + g_L \mathcal{L}_{j,\text{cs1}}^{\mu\nu} \mathcal{J}_\nu^2 \sum_i \mathcal{J}_\mu^{1,i}, \quad (3.12)$$

where the legs of the W boson emission l for NCs (possible on two legs) and CCs (only one possible leg) depend on the flavour combination j , as explained in Section 3.2.1, and $\mathcal{D}_V^{\mu\nu} \propto g^{\mu\nu}$ is the propagator of the exchanged current, with V going over W, Z, and γ .

The combined electroweak coupling factors $g_{V/L}$ are the only components that are totally diagram specific.

Currents and diagrams for helicity combinations that give zero are not calculated in the first place. These are all diagrams in which right-handed quarks couple to a W boson. Consequently, CC diagrams only give a contribution if all quarks are left-handed, NC and LT diagrams if the quarks of the flavour changing line are left-handed.

The implementation in VBFNLO is done via `braket` routines. These offer the possibility to attach vector bosons to incoming or outgoing spinors (bras and kets) of fermions. Bras and kets can be combined to currents via the routine `curr6`, and then contracted with other currents via `dotcc` or two currents with a leptonic tensor via `contract_Tjj`. The calculation sequence of the total amplitude at one phase-space point can be summarised in the following steps:

1. Calculate effective polarisation vector and leptonic tensors.
2. First subprocess: Map physical momenta to momenta of the chosen crossing, Eq. 3.7.
3. Calculate quark spinors and gluon polarisation vector.
4. Compute all needed currents: Empty quark lines, lines with W boson attached, lines with gluon attached, lines with W boson and gluon attached, in every order.
5. Calculate diagrams by contracting currents and leptonic tensors and multiplying by propagator and/or coupling factors.
6. Sum up diagrams for different positions of W boson emission and leptonic tensors and square the result.
7. Sum over helicities, gluon polarisation and colour structure (if both exist¹), and multiply by factors.
8. Fold with PDFs for all combinations of possible initial state partons for the considered subprocess.
9. Repeat step 2 to 8 for all subprocesses and sum over results.
10. Return squared amplitude to function *Amplitude*.

In step eight the term *all possible initial state partons* refers to up, down, strange and charm quarks, but not to bottom or top quarks, for the reasons explained in Section 3.1. For a combination of charm quark as particle 1 and down quark as particle 2 for example, the squared matrix element for the flavour combination $u\bar{D} \rightarrow uUgW$ is folded with the corresponding PDFs for a charm quark of momentum p_1 and a down quark of momentum p_2 .

¹ Subprocesses with initial state gluon only exist for one colour structure.

3.3 Real Emissions

The real emission contribution contains one additional jet in the final state, so the final state observable is given by $Wjjjj$. The subprocesses leading to this observable can be separated into two general subprocess classes, namely

- (a) subprocesses with six external quarks ($q_1 Q_2 \rightarrow q_3 Q_4 \bar{q}'_5 q'_6$ and crossing related ones with antiquark(s) in the initial state), and
- (b) subprocesses with two external gluons and four external quarks.

The second class can further be separated into

- (i) subprocesses with two final state gluons, e.g. $q_1 Q_2 \rightarrow q_3 Q_4 gg$,
- (ii) subprocesses with one initial state gluon, e.g. $q_1 g \rightarrow q_3 Q_4 \bar{Q}_2 g$ or $g Q_2 \rightarrow q_3 Q_4 \bar{q}_1 g$,
- (iii) subprocesses with two initial state gluons, $gg \rightarrow q_3 Q_4 \bar{q}_1 \bar{Q}_2$,

and for the quark initiated ones the corresponding crossing related subprocesses with antiquark(s) in the initial state.

In analogy to the LO calculation, the leptonic tensors and the effective polarisation vector of the W boson are calculated once per phase space point and reused during the calculation of different subprocesses. The leptonic tensors are needed for four momentum flows, corresponding to p_5 and p_6 being connected either both to the upper line, both to the lower line or one to the upper line and one to the lower line. Only the first two cases are needed for the six-quark subprocesses, since the two additional quarks both couple to the same line.

To reduce calculational effort, all currents needed for the matrix element calculation are calculated before entering the first subprocess, saved, and later on called when needed. Because many currents are needed at least twice, such as an empty line $q_1 q_3$ for both the qQ as well as the $q\bar{Q}$ incoming state, this reduces the computing time considerably. For a sole tree-level calculation of the real emission amplitude, the amount of computing time saved after implementing this precalculation of currents was tested to be 17% for the calculation running over 2^{26} phase space points with 4 grid iterations, of which about 2^{24} passed the cuts in the last iteration.

3.3.1 Subprocesses with Two Gluons

Subprocesses with the same topology but exchanged gluons give the same amplitude at another phase space point. Due to the performed integration over phase space, only one of these configurations has to be calculated per phase space point. As the additional gluon does not affect the flavours of the quarks, the flavour combinations and possible positions of W boson emission are the same as in the leading order calculation. However, there are now more colour structures, which are related to the positions of the two gluons. These shall be explained in detail for the qQ initial state with two final state gluons.

In the following, the amplitude \mathcal{M}^{qQ} for a specific helicity and polarisation combination shall be considered. It can be expressed as the sum of six colour structure subamplitudes multiplied with tensors $\mathcal{T}^{(m)}$,

$$\mathcal{M}^{\text{qQ}} = \sum_{m=1}^6 \mathcal{T}^{(m)} \mathcal{M}^{(m)}. \quad (3.13)$$

If the gluons are emitted from opposite lines, the amplitudes are given by¹

$$\mathcal{T}^{(3)} \mathcal{M}^{(3)} = t_{ji}^a \hat{t}_{lk}^b \mathcal{M}^{(3)} \quad \text{and} \quad (3.14)$$

$$\mathcal{T}^{(4)} \mathcal{M}^{(4)} = t_{ji}^b \hat{t}_{lk}^a \mathcal{M}^{(4)}, \quad (3.15)$$

where $\mathcal{M}^{(3)}$ includes all diagrams with the gluon of colour a being emitted from the upper line and the one with colour b being emitted from the lower one. $\mathcal{M}^{(4)}$ analogously contains the diagrams with contrariwise emissions. The indices i and j label the colour charges of the upper line quarks, k and l the colour charges of the lower line quarks and the hat over t symbolises the different SU(3) algebra. If the two gluons are both emitted from the upper line, there are three possible topologies. They can be emitted one after another, as in Figures 3.5(a) to (c), where either the one corresponding to colour a can be emitted closer

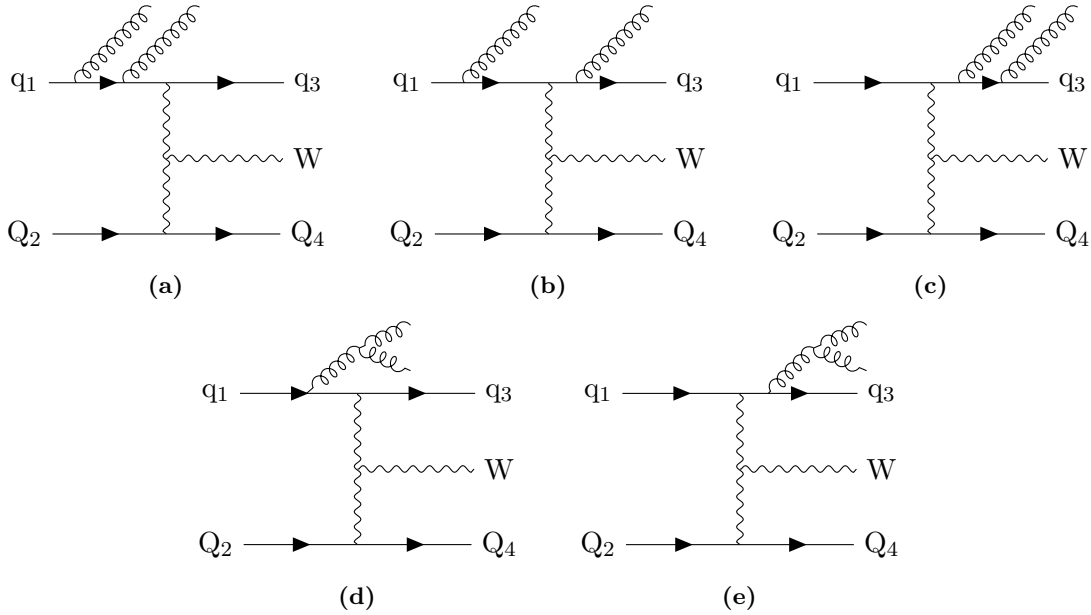


Figure 3.5: Diagrams contributing to colour structures 1 and 2 for a two-gluon subprocess with W boson production as leptonic tensor.

¹ For better readability, the indices of a component of $\mathcal{T}^{(i)}$ will be suppressed here and in the following equations, so instead of $\mathcal{T}_{jilk}^{(m)ab}$, $\mathcal{T}^{(m)}$ will be written.

to the final quark, or the one corresponding to colour b . The matrix elements comprising the corresponding diagrams are called \mathcal{M}_A and \mathcal{M}_B , respectively. The gluons can also be produced in non-abelian diagrams with a three-gluon vertex, like in Figures 3.5(d) and (e), which is denoted by \mathcal{M}_C . Since the generators appearing from the quark-gluon vertices are now of the same colour algebra, they do not commute. This gives three different tensor structures for the three topologies, whose sum gives the first two colour structures of Equation 3.13,

$$\mathcal{T}^{(1)}\mathcal{M}^{(1)} + \mathcal{T}^{(2)}\mathcal{M}^{(2)} = \delta_{lk} \left(t^a t^b \right)_{ji} \mathcal{M}_A + \delta_{lk} \left(t^b t^a \right)_{ji} \mathcal{M}_B + \delta_{lk} \left[t^a, t^b \right]_{ji} \mathcal{M}_C. \quad (3.16)$$

In order to simplify the calculation in such a way that the squared amplitude does not contain interference terms of these different diagram kinds, the $\mathcal{T}^{(m)}$ can be chosen orthogonal. It can easily be shown that all three terms are already separately orthogonal to $\mathcal{T}^{(3)}$ and $\mathcal{T}^{(4)}$, as the preservation of the lower line colour charge leads to the trace over \hat{t}^b or \hat{t}^a , which gives zero. By forming linear combinations of the terms, $\mathcal{T}^{(1)}$ and $\mathcal{T}^{(2)}$ can be chosen as two orthogonal tensors, namely the commutator and anticommutator of t^a and t^b , since

$$\begin{aligned} \left\{ t^a, t^b \right\}_{ji}^* \left[t^a, t^b \right]_{ji} &= \left\{ t^a, t^b \right\}_{ji} \left[t^a, t^b \right]_{ji} \\ &= \text{Tr} \left(t^a t^b t^a t^b + t^b t^a t^a t^b - t^a t^b t^b t^a - t^b t^a t^b t^a \right) = 0, \end{aligned} \quad (3.17)$$

and

$$\left(t^a t^b \right)_{ji} = \frac{1}{2} \left(\left\{ t^a, t^b \right\}_{ji} + \left[t^a, t^b \right]_{ji} \right). \quad (3.18)$$

So

$$\sum_{m=1}^2 \mathcal{T}^{(m)}\mathcal{M}^{(m)} = \frac{1}{2} \delta_{lk} \left(\left\{ t^a, t^b \right\}_{ji} (\mathcal{M}_A + \mathcal{M}_B) + \left[t^a, t^b \right]_{ji} (\mathcal{M}_A - \mathcal{M}_B + 2\mathcal{M}_C) \right). \quad (3.19)$$

The tensors for colour structures five and six, where both gluons are emitted from the lower line, can be derived similarly. Summing up, the colour structure tensors $\mathcal{T}^{(m)}$ in Equation 3.13 are given by

$$\begin{aligned} \mathcal{T}^{(1)} &= \frac{1}{2} \delta_{lk} \left\{ t^a, t^b \right\}_{ji}, & \mathcal{T}^{(2)} &= \frac{1}{2} \delta_{lk} \left[t^a, t^b \right]_{ji}, \\ \mathcal{T}^{(3)} &= t_{ji}^a \hat{t}_{lk}^b, & \mathcal{T}^{(4)} &= t_{ji}^b \hat{t}_{lk}^a, \\ \mathcal{T}^{(5)} &= \frac{1}{2} \delta_{ji} \left\{ \hat{t}^a, \hat{t}^b \right\}_{lk}, & \mathcal{T}^{(6)} &= \frac{1}{2} \delta_{ji} \left[\hat{t}^a, \hat{t}^b \right]_{lk}. \end{aligned} \quad (3.20)$$

With this, the colour sums of the squared amplitude give

$$\begin{aligned} \sum_{a,b} \sum_{i,j,k,l} \left| \mathcal{M}^{\text{qQ}} \right|^2 &= \sum_{a,b} \sum_{i,j,k,l} \sum_{m=1}^6 \left| \mathcal{J}^{(m)} \mathcal{M}^{(m)} \right|^2 \\ &= \sum_{m,n=1}^6 C^{(nm)} \left(\mathcal{M}^{(n)} \right)^* \mathcal{M}^{(m)}, \end{aligned} \quad (3.21)$$

with constants $C^{(nm)}$ calculable with the colour algebra relations of Equation 2.20 to (see Appendix C)

$$\begin{aligned} C^{(11)} = C^{(55)} &= \frac{NC_F}{2} \left(NC_F - \frac{1}{2} \right), & C^{(22)} = C^{(66)} &= \frac{NC_F}{2} \left(NC_F + \frac{1}{2} \right), \\ C^{(33)} = C^{(44)} &= N^2 C_F^2, \\ C^{(15)} = C^{(51)} &= \frac{NC_F}{2}, & C^{(34)} = C^{(43)} &= \frac{NC_F}{2}, \end{aligned} \quad (3.22)$$

and all other interference terms being zero. In the VBF approximation, also the non-zero interference terms are neglected, as due to the approach with two different colour algebras the gluon with colour a has to be identified with either the upper or the lower colour algebra. While for the LO calculation the approximation was justified by a $1/N$ suppression of the neglected terms, the interference terms of the two-gluon subprocesses are colour suppressed by a factor of $1/(N^2 - 1)$ with respect to the other terms. In both cases, the neglected terms are additionally subject to a kinematic suppression when applying standard VBF cuts [50, p. 7].

For other subprocesses than the one with two initial quarks considered so far not all six colour structures exist. Processes with one gluon in the initial state only contain diagrams of colour structure 1, 2 and 3, if the initial gluon is attached to quark line q_1q_3 , or colour structures 4, 5, and 6, if it is attached to line q_2q_4 . Here, only the gluon with colour a is considered as an initial state gluon, since the integration over phase space gives also the process with exchanged gluons. For processes with two initial state gluons only one colour structure exists, which can be either colour structure 3 or 4 depending on which gluon is coupled to which line. It does not matter which of these two colour structures is chosen for the calculation as the phase space integration leads to the same result for both.

The calculation of the matrix elements $\mathcal{M}^{(m)}$ follows the same logic as in the leading order calculation, since the possible flavour combinations giving the expected final state are the same for the two-gluon processes. The main difference is the calculation of the currents contributing to the diagrams for colour structures 1, 2, 5, and 6, where two gluon polarisation vectors have to be added to the bras or kets, or the effective polarisation vectors of the gluon for the non-abelian graphs \mathcal{M}_C have to be built. Another difference are the colour prefactors f_c in the averaged polarisation sum over the squared real emission

matrix element, $\overline{\sum} |\mathcal{M}_R|^2$. The subprocesses with two initial quarks or antiquarks contain an additional factor $1/2$ to take care of the two identical final state particles, the gluons, so in this case $f_c = 1/(2N^2)$. For subprocesses with one initial state gluon, the factor stays the same as in the leading order calculation, so $f_c = 1/(N(N^2 - 1))$. The subprocess with two initial gluons, that did not exist in the leading order, carries a factor of $f_c = 1/(N^2 - 1)^2$ to average over both gluon colour charges.

3.3.2 Subprocesses with Six External Quarks

For processes with the gluon splitting into two quarks, only four subprocesses need to be considered, namely

$$\begin{aligned}
 q_1 Q_2 &\rightarrow q_3 Q_4 \bar{q}'_5 q'_6 W, \\
 q_1 \bar{Q}_4 &\rightarrow q_3 \bar{Q}_2 \bar{q}'_5 q'_6 W, \\
 \bar{q}_3 Q_2 &\rightarrow \bar{q}_1 Q_4 \bar{q}'_5 q'_6 W, \\
 \bar{q}_3 \bar{Q}_4 &\rightarrow \bar{q}_1 \bar{Q}_2 \bar{q}'_5 q'_6 W,
 \end{aligned} \tag{3.23}$$

because all other subprocesses, like ones with q'_5 in the initial state, are then reached by the phase space integration. The third quark pair is denoted with primes, as it can either be coupled to the upper quark line and thus belong to the colour algebra of q_1 and q_3 , which is likewise colour structure 1 in the LO calculation, or it can be connected to the lower line and thus belong to the algebra of Q_2 and Q_4 . While the implementation in VBFNLO was done for the crossing related process $q_1 Q_2 q'_5 \rightarrow q_3 Q_4 q'_6 W$ for reasons of simplicity, the first of the above mentioned subprocesses is chosen for the following explanation of the matrix element calculation.

Because there is now a third quark line to which the electroweak current or the emitted W boson can couple, there are 15 flavour combinations contributing to the W_{jjjj} process, which are given in Table 3.1. Likewise to Equation 3.8, $u/U/u'$ and $d/D/d'$ are representative for all included quark generations. Since there are three quark lines, from which two are coupled by a gluon, the electroweak current connecting the not-gluon-connected line can couple to either one of these two lines. This classifies the two general diagram topologies A and B in Figures 3.6(a), (b) for colour structure 1 and Figures 3.7(a), (b) for colour structure 2. In these Figures the emission of the W boson is omitted for simplicity. It can be emitted from one of the now six quark legs, or as leptonic tensor, where again the possible positions depend on the flavour combination and if the exchanged electroweak current is an NC or CC. For flavour combinations (a) to (l), diagram types A and B exist as NC, CC, and as LT diagrams. In NC diagrams, the W boson can be emitted from both quarks of the flavour changing line, while in CC diagrams it is emitted from one of the quarks of the line not changing flavour but also connected to the electroweak current. Since in the remaining flavour combinations (m) to (o) all three lines in diagram types A and B change flavour, these do only exist as CC.

Table 3.1: Flavour combinations for the real emission subprocesses with six external quarks.

W^-jjjj		W^+jjjj
$d D \rightarrow d U \bar{d}' d' W$	(a)	$u U \rightarrow u D \bar{u}' u' W$
$d D \rightarrow d U \bar{u}' u' W$	(b)	$u U \rightarrow u D \bar{d}' d' W$
$u D \rightarrow u U \bar{d}' d' W$	(c)	$d U \rightarrow d D \bar{u}' u' W$
$u D \rightarrow u U \bar{u}' u' W$	(d)	$d U \rightarrow d D \bar{d}' d' W$
$d D \rightarrow u D \bar{d}' d' W$	(e)	$u U \rightarrow d U \bar{u}' u' W$
$d D \rightarrow u D \bar{u}' u' W$	(f)	$u U \rightarrow d U \bar{d}' d' W$
$d U \rightarrow u U \bar{d}' d' W$	(g)	$u D \rightarrow d D \bar{u}' u' W$
$d U \rightarrow u U \bar{u}' u' W$	(h)	$u D \rightarrow d D \bar{d}' d' W$
$d D \rightarrow d D \bar{d}' u' W$	(i)	$u U \rightarrow u U \bar{u}' d' W$
$d U \rightarrow d U \bar{d}' u' W$	(j)	$u D \rightarrow u D \bar{u}' d' W$
$u D \rightarrow u D \bar{d}' u' W$	(k)	$d U \rightarrow d U \bar{u}' d' W$
$u U \rightarrow u U \bar{d}' u' W$	(l)	$d D \rightarrow d D \bar{u}' d' W$
$d D \rightarrow u U \bar{u}' d' W$	(m)	$u U \rightarrow d D \bar{d}' u' W$
$d U \rightarrow u D \bar{d}' u' W$	(n)	$u D \rightarrow d U \bar{u}' d' W$
$u D \rightarrow d U \bar{d}' u' W$	(o)	$d U \rightarrow u D \bar{u}' d' W$

In contrast to the leading order calculation, two quark lines now belong to the same colour algebra. This means that if they belong to the same flavour generation, there are additional contributions from diagrams of type C and D as in Figures 3.6(c), (d) (cs1) and 3.7(c), (d) (cs2), which interfere with the A and B diagrams. For the chosen reference subprocess, C and D diagrams can basically be obtained from A and B by exchanging q_3 and q'_6 for cs1, or Q_4 and q'_6 for cs2, but keeping the momenta. Thus there are flavour combinations with the same initial and final state particles, giving the same process for another phase space point. For example the process

$$d D \rightarrow u U \bar{u} d W$$

corresponds to flavour combination (m), but also to flavour combination (b), with the only difference that the final u and d quarks carry the momenta p_3 and p_6 in different order. After phase space integration, this process would thus be included twice, which is

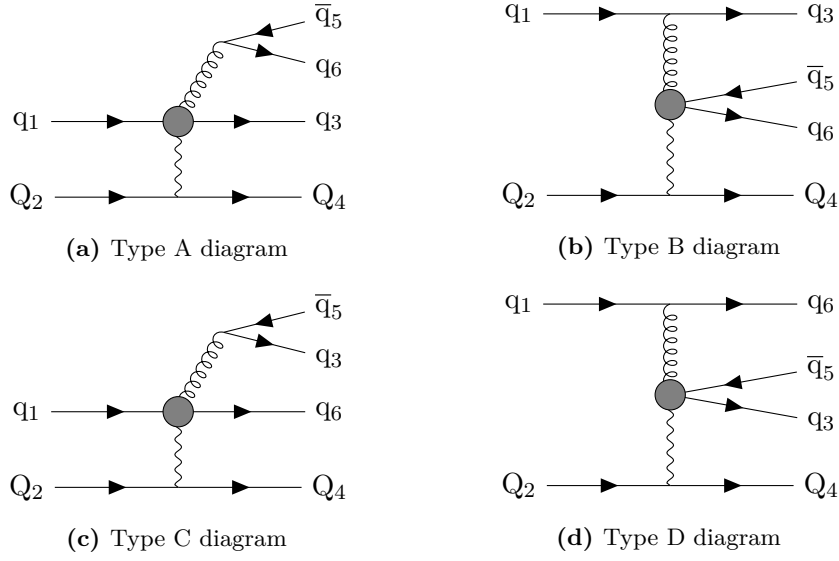


Figure 3.6: Diagram types for six-quark subprocesses for colour structure 1. The final state W boson is omitted for simplicity. The grey circle is explained in Appendix B.

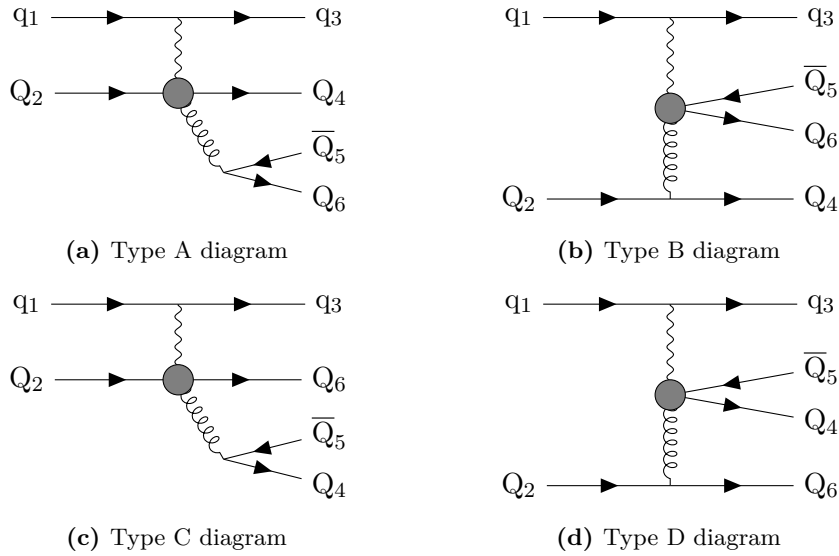


Figure 3.7: Diagram types for six-quark subprocesses for colour structure 2. The final state W boson is omitted for simplicity. The grey circle is explained in Appendix B.

why C and D diagrams in cs1 are calculated only for one of the two flavour combinations. Except for $(b)-(m)$, there are three more flavour combination pairs that are redundant in interference for cs1, which are $(c)-(o)$, $(e)-(i)$, and $(g)-(j)$. For cs2, the redundant interference pairs are $(a)-(i)$, $(c)-(k)$, $(f)-(m)$, and $(g)-(n)$.

However, these pairs are only redundant in the case of the two incoming particles being

quarks, which is the case in the chosen subprocess. For subprocesses with incoming antiquarks, the redundant combinations differ, since then \bar{q}'_5 and \bar{q}_1 or \bar{q}'_5 and \bar{Q}_2 are the exchangeable particles for cs1 or cs2, respectively. The redundant pairs for incoming antiquark and colour structure 1, meaning \bar{q}_3 is incoming, are (b)-(o), (c)-(m), (f)-(k), and (h)-(l). These are independent of the kind of incoming particle on line q_2q_4 . For colour structure 2, meaning \bar{Q}_4 is incoming, the redundant pairs are (b)-(j), (d)-(l), (f)-(n), and (g)-(m).

The calculation of currents is again done with the `braket` routines of VBFNLO, in which now also whole currents are attached to one bra or ket, for example the current of line q_5q_6 to q_1 or q_3 for a cs1 diagram of type A. As stated above, all needed currents are precalculated before the calculation of the first subprocess, as most of them are needed for more than one subprocess. During the calculation of one subprocess, these precalculated currents are accessed, contracted and multiplied by propagator and coupling factors to construct the necessary diagrams. The diagram types A and B are summed and squared separately from the C and D diagrams and summed over helicities. For the amplitude in the interference case,

$$|\mathcal{M}_{\text{int}}|^2 = |\mathcal{M}_{A,B} - \mathcal{M}_{C,D}|^2 = |\mathcal{M}_{A,B}|^2 + |\mathcal{M}_{C,D}|^2 - 2\text{Re}(\mathcal{M}_{A,B}^* \mathcal{M}_{C,D}), \quad (3.24)$$

the interference term $\mathcal{M}_{A,B}^* \mathcal{M}_{C,D}$ is also needed. The minus sign stems from the exchange of two fermions in the final state, which is why the C and D diagrams are also called *Pauli interference* graphs. Since this term is zero if the helicities of the interfering quark lines are not identical,¹ this term is only summed over the helicities of q_1 and q_2 , with the helicity of q_5 set to the one of q_1 for cs1, and to q_2 for cs2 matrix elements.

In all diagram types there are two quark-gluon vertices, that give in the sum over external colours i_k , with $k = 1, \dots, 6$, a factor of

$$(\delta_{i_4 i_2} t_{i_3 i_1}^a t_{i_6 i_5}^a)^* (\delta_{i_4 i_2} t_{i_3 i_1}^b t_{i_6 i_5}^b) = N \text{Tr}(t^a t^b) \text{Tr}(t^a t^b) = \frac{N}{4} (N^2 - 1), \quad (3.25)$$

while the interference term carries a factor of

$$(\delta_{i_4 i_2} t_{i_3 i_1}^a t_{i_6 i_5}^a)^* (\delta_{i_4 i_2} t_{i_6 i_1}^b t_{i_3 i_5}^b) = N \text{Tr}(t^a t^b t^a t^b) = -\frac{1}{4} (N^2 - 1). \quad (3.26)$$

This causes the interference term to be colour suppressed by a factor of $N = 3$. The colour prefactor stemming from the average over incoming colours is always $f_c = 1/N^2$, as the incoming particles are either quarks or antiquarks. In the interference case an additional factor of 1/2 has to be multiplied, which accounts in some cases for identical particles in the final state and in others to not having calculated a process twice after phase space integration.

¹ A cs1 example can be considered to illustrate this. Then $\mathcal{M}_{A,B}$ is only non-zero for $s_1 = s_3$ and $-s_5 = s_6$, while $\mathcal{M}_{C,D}$ is non-zero for $s_1 = s_6$ and $-s_5 = s_3$, with s_i denoting the helicity of quark i . Thus, the only non-zero interference terms are the ones with $s_1 = s_3 = -s_5 = s_6$.

Inclusion of Bottom Quarks

In the LO calculation, only the quark flavours up, down, strange, and charm are considered, as the inclusion of bottom quarks would essentially lead to diagrams where an intermediate top quark is produced, which would violate the approximation of massless partons. For the real emission amplitude, there are flavour combinations for which the third quark line does not change flavour and never couples to a charged electromagnetic current. In cs1, this is the case only if the flavour of line q_1q_3 changes, so for flavour combinations (e) and (g), while for cs2 line q_2q_4 needs to change flavour, which is the case for (a) and (c). For these combinations, the flavour of q_5 and q_6 can also be chosen as bottom, while for all other flavour combinations this would lead to diagrams with intermediate or even external top quarks. In the program this inclusion can be done by simply changing one variable, called “nflVBF”, which incorporates the number of included quark flavours. If this variable is set to 5, the above mentioned diagrams with bottom quarks are included in addition to the diagrams that appear for only first and second generation quarks. It is however disputable if this inclusion would lead to an improvement of the result due to the small portion of additional diagrams that can be included, while experimental measurements can only distinguish between the final observables produced. Since bottom and top quarks produce distinct observables in a detector, it is probably a more correct approach to neglect all diagrams including top and bottom quarks in the first place.

3.3.3 Dipole Subtraction Terms

Divergent terms appear in the real emission cross section if one of the final partons gets soft or two partons are collinear. They can be subtracted before the phase space integration with the dipole subtraction method proposed by Catani and Seymour [44], see Section 2.3.2. The 4-final-parton contribution to the cross section can accordingly be written as

$$\begin{aligned}
 \sigma_4^{\text{NLO}} &= \int \left(d\sigma^{\text{R}} - d\sigma^{\text{A}} \right) \\
 &= \sum_{a,b} \int_0^1 dx_1 \int_0^1 dx_2 f_{a/P_1}(x_1, \mu_{\text{F}}) f_{b/P_2}(x_2, \mu_{\text{F}}) \frac{1}{2\hat{s}} \\
 &\quad \cdot \int d\Phi(p_1, p_2; p_3, p_4, p_5, p_6, p_1, p_\nu) c_s \left\{ \overline{\sum} \left| \mathcal{M}_{\text{R}}^{a,b} \right|^2 - \sum_{m=1}^{n_d} \mathcal{D}(m) \right\},
 \end{aligned} \tag{3.27}$$

with dipole terms $\mathcal{D}(m)$ and symmetry factor $c_s = 1$ for most subprocesses and $c_s = 1/2$ for subprocesses with identical final state particles. Here and in the following, the incoming partons are always numbered 1 and 2. The number of dipole kinematics n_d depends on the subprocess, meaning on the kind of incoming partons. Each kinematic consists of a particle triplet of *emitter*, *emittee* and *spectator*, whereby the collinearity of emitter and emittee produces a singularity in the real emission cross section. With their momenta a

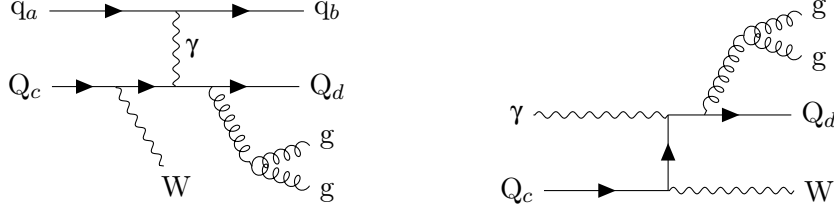


Figure 3.8: If q_a and q_b are collinear, the photon propagator in the diagram on the left diverges. This diagram gives an electroweak correction to the diagram on the right. To handle the singularity, a cut is imposed on the virtuality of the t -channel exchange.

corresponding Born-level momentum configuration is determined, which is

$$\tilde{p}_k^\mu = p_k^\mu + p_j^\mu - (1 - x_{jk,a}) p_a^\mu, \quad \tilde{p}_{aj}^\mu = x_{jk,a} p_a^\mu, \quad x_{jk,a} = 1 - \frac{p_k \cdot p_j}{(p_k + p_j) \cdot p_a}, \quad (3.28)$$

for a kinematic with initial state emitter a and final state spectator k ,

$$\tilde{p}_{ij}^\mu = p_i^\mu + p_j^\mu - (1 - x_{ij,b}) p_b^\mu, \quad \tilde{p}_b^\mu = x_{ij,b} p_b^\mu, \quad x_{ij,b} = 1 - \frac{p_i \cdot p_j}{(p_i + p_j) \cdot p_b}, \quad (3.29)$$

for a kinematic with final state emitter i but initial state spectator b , and

$$\tilde{p}_{ij}^\mu = p_i^\mu + p_j^\mu - \frac{y_{ij,k}}{1 - y_{ij,k}} p_k^\mu, \quad \tilde{p}_k^\mu = \frac{1}{1 - y_{ij,k}} p_k^\mu, \quad y_{ij,k} = \frac{p_i \cdot p_j}{p_i \cdot (p_j + p_k) + p_j \cdot p_k}, \quad (3.30)$$

for a kinematic with both emitter i and spectator k being final state partons [44]. Here the emittee, which is always final, has been labelled with j . For a given triplet the dipole terms are then given by kinematic-dependent factors multiplied by colour and spin-correlated Born matrix elements of this momentum configuration. In general their calculation depends on the kind of dipole, which can be classified according to the emitter and spectator being initial or final state partons. In the limit of soft gluons¹ and collinear partons that cause singularities, these dipole terms exactly cancel the real emission matrix elements.

Dipole terms transcending the VBF approximation are neglected in the calculation. These are all terms for which the triplet of emitter, emittee, and spectator involves partons of both the upper and the lower colour algebra. Examples for such terms are the dipoles \mathcal{D}_4^{13} , $\mathcal{D}_{34,5}$, etc., where the notation is chosen such that initial spectators/splittings are superscripts, whereas final ones are subscripts. Consequently, no kinematics involving both an initial state emitter and an initial state spectator are considered.

Diagrams with emitter and emittee pair being connected to a weak current do not cause singularities, as the denominator of the propagator then contains at least the invariant mass of the current. The propagator of a t -channel photon on the other hand diverges if

¹ In contrast to soft gluons, soft quarks do not cause singularities, since their wavefunctions contain a factor of energy cancelling the one in the denominator of the propagator.

the quarks of a gluonless line coupling to it become collinear. Diagrams involving such a photon correspond to electroweak corrections to processes with an initial photon and one parton going into three partons, as shown in Figure 3.8. They appear for both the six-quark and the two-gluon subprocesses. Following the example of Reference [45, p. 12], this singularity is handled by introducing a cut on the virtuality $Q^2 = -t$ of the exchanged t -channel current at $Q_{\min}^2 = 4 \text{ GeV}^2$. This procedure and the specific choice for the cut are justified in Section 4.4, where the effect on the total cross section is shown. To obtain the small part of the total cross section lost by this procedure, the cross section of the corresponding process $p\gamma \rightarrow WjjjX$ needs to be calculated, which is not done in this work similar to all other electroweak corrections. In the leading order calculation, this situation does not appear because of the required minimum number of identified jets. A jet collinear to the beam line cannot be measured.

The dipole kinematics and calculation of the dipole factors for the two-gluon subprocesses are similar to the one for the process $pp \rightarrow Hjjj$ and demonstrated in detail in Reference [51]. Here, only the general idea shall be pointed out exemplary for the subprocess with two initial gluons,

$$g(p_1) g(p_2) \rightarrow q_b(p_3) Q_d(p_4) \bar{q}_a(p_5) \bar{Q}_c(p_6) W(P_W), \quad (3.31)$$

with $P_W = p_1 + p_2$. In all two-gluon subprocesses, singularities involve at least one gluon, for example a gluon being collinear to the quark it was emitted from. In this specific subprocess, the two gluons belong to different colour algebras, so in addition all dipole terms involving both gluons are colour suppressed. The quarks themselves all couple to an electromagnetic current, so singularities only exist for a quark solely coupling to one of the gluons and becoming collinear to this gluon. This means there are only four dipole terms for this subprocess, all of which subtract singularities caused by the emission of a collinear quark from an initial state gluon. They are given by squared Born amplitudes (summed over polarisations and colours) of the following momentum configurations:

$$\begin{aligned} \mathcal{D}_3^{15} &= \frac{1}{2} \left| \mathcal{M}_B^{\text{qg}} \right|^2 \mathcal{D}_{if,\text{qg}}^{15,3} : & q_a(\tilde{p}_{15}) g(p_2) \rightarrow q_b(\tilde{p}_3) Q_d(p_4) \bar{Q}_c(p_6) W(P_W), \\ \mathcal{D}_5^{13} &= \frac{1}{2} \left| \mathcal{M}_B^{\bar{\text{qg}}} \right|^2 \mathcal{D}_{if,\text{qg}}^{13,5} : & \bar{q}_b(\tilde{p}_{13}) g(p_2) \rightarrow \bar{q}_a(\tilde{p}_5) Q_d(p_4) \bar{Q}_c(p_6) W(P_W), \\ \mathcal{D}_4^{26} &= \frac{1}{2} \left| \mathcal{M}_B^{\text{gQ}} \right|^2 \mathcal{D}_{if,\text{qg}}^{26,4} : & g(p_1) Q_c(\tilde{p}_{26}) \rightarrow q_b(p_3) Q_d(\tilde{p}_4) \bar{q}_a(p_5) W(P_W), \\ \mathcal{D}_5^{13} &= \frac{1}{2} \left| \mathcal{M}_B^{\text{g}\bar{\text{Q}}} \right|^2 \mathcal{D}_{if,\text{qg}}^{13,5} : & g(p_1) \bar{Q}_d(\tilde{p}_{24}) \rightarrow q_b(p_3) \bar{q}_a(p_5) \bar{Q}_c(\tilde{p}_6) W(P_W). \end{aligned}$$

The $\mathcal{D}_{if,\text{qg}}^{ij,k}$ are the dipole prefactors for initial-final splittings, meaning for initial emitter and final spectator, and can be looked up in Reference [51] or constructed following Reference [44].

With the cut on the photon virtuality, singularities in the six-quark subprocesses only appear in the gluon propagator if the quarks of the line not coupling to the electromagnetic

current become collinear. If the two quarks of this line do change flavour, the final state W boson is emitted from one of them and thus no singularity appears. As a consequence, flavour combinations (m), (n) and (o) do not contain diagrams causing singularities and no dipole terms are calculated for those.¹ In the non-interference case, where the flavour generation of \bar{q}'_5 and q'_6 is not the same as the one of either q_1 or Q_2 , up to eight dipole configurations exist. These correspond to the two quarks of each line becoming collinear, so for example if \bar{q}'_5 and q'_6 are collinear and do not change flavour, diagrams of type A are singular, and if q_1 and q_3 are collinear and of same flavour, diagrams of type B are singular. In the interference case, additional dipoles need to be subtracted to treat singularities arising from diagram types C and D, which appear for example if q'_6 and q_1 are collinear and have the same flavour.

All possible dipoles for subprocesses with two initial quarks and two initial antiquarks and their corresponding Born configurations are listed in Tables 3.2 and 3.3, respectively, where for a specific flavour combination only those dipoles contribute for which $q_i = q_j/Q_i = Q_j$ with emitter i and emittee j . This means for the process $dD \rightarrow dD\bar{s}'c'W$ only \mathcal{D}_5^{13} , \mathcal{D}_6^{13} , \mathcal{D}_5^{24} , and \mathcal{D}_6^{24} are subtracted. The dipoles for $q\bar{Q} \rightarrow \dots$ -subprocesses match the cs1 ones of the $qQ \rightarrow \dots$ -subprocess and the cs2 ones of the $\bar{q}\bar{Q} \rightarrow \dots$ -subprocess, and for the $\bar{q}Q \rightarrow \dots$ -subprocess analogously.

¹ Some of the interference graphs of these flavour combinations can contain singularities, but are redundant with the ones of other flavour combinations and their dipole terms handled there.

Table 3.2: Dipoles for $q_a(p_1) Q_c(p_2) \rightarrow q_b(p_3) Q_d(p_4) \bar{q}'_5(p_5) q'_6(p_6) W(P_W)$ processes and the corresponding Born kinematics. Depending on the flavours of the quarks not all dipoles contribute.

Colour structure 1 dipoles	
Dipole	Born kinematic
\mathcal{D}_5^{13} :	$g(\tilde{p}_{13}) Q_c(p_2) \rightarrow Q_d(p_4) \bar{q}_5(\tilde{p}_5) q_6(p_6) W(P_W)$
\mathcal{D}_6^{13} :	$g(\tilde{p}_{13}) Q_c(p_2) \rightarrow Q_d(p_4) \bar{q}_5(p_5) q_6(\tilde{p}_6) W(P_W)$
\mathcal{D}_{56}^1 :	$q_a(\tilde{p}_1) Q_c(p_2) \rightarrow q_b(p_3) Q_d(p_4) g(\tilde{p}_{56}) W(P_W)$
$\mathcal{D}_{56,3}$:	$q_a(p_1) Q_c(p_2) \rightarrow q_b(\tilde{p}_3) Q_d(p_4) g(\tilde{p}_{56}) W(P_W)$
\mathcal{D}_3^{16} :	$g(\tilde{p}_{16}) Q_c(p_2) \rightarrow q_b(\tilde{p}_3) Q_d(p_4) \bar{q}_5(p_5) W(P_W)$
\mathcal{D}_5^{16} :	$g(\tilde{p}_{16}) Q_c(p_2) \rightarrow q_b(p_3) Q_d(p_4) \bar{q}_5(\tilde{p}_5) W(P_W)$
\mathcal{D}_{35}^1 :	$q_a(\tilde{p}_1) Q_c(p_2) \rightarrow Q_d(p_4) g(\tilde{p}_{35}) q_6(p_6) W(P_W)$
$\mathcal{D}_{35,6}$:	$q_a(p_1) Q_c(p_2) \rightarrow Q_d(p_4) g(\tilde{p}_{35}) q_6(\tilde{p}_6) W(P_W)$
Colour structure 2 dipoles	
Dipole	Born kinematic
\mathcal{D}_5^{24} :	$q_a(p_1) g(\tilde{p}_{24}) \rightarrow q_b(p_3) \bar{Q}_5(\tilde{p}_5) Q_6(p_6) W(P_W)$
\mathcal{D}_6^{24} :	$q_a(p_1) g(\tilde{p}_{24}) \rightarrow q_b(p_3) \bar{Q}_5(p_5) Q_6(\tilde{p}_6) W(P_W)$
\mathcal{D}_{56}^2 :	$q_a(p_1) Q_c(\tilde{p}_2) \rightarrow q_b(p_3) Q_d(p_4) g(\tilde{p}_{56}) W(P_W)$
$\mathcal{D}_{56,4}$:	$q_a(p_1) Q_c(p_2) \rightarrow q_b(p_3) Q_d(\tilde{p}_4) g(\tilde{p}_{56}) W(P_W)$
\mathcal{D}_4^{26} :	$q_a(p_1) g(\tilde{p}_{26}) \rightarrow q_b(p_3) Q_d(\tilde{p}_4) \bar{Q}_5(p_5) W(P_W)$
\mathcal{D}_5^{26} :	$q_a(p_1) g(\tilde{p}_{26}) \rightarrow q_b(p_3) Q_d(p_4) \bar{Q}_5(\tilde{p}_5) W(P_W)$
\mathcal{D}_{45}^2 :	$q_a(p_1) Q_c(\tilde{p}_2) \rightarrow q_b(p_3) g(\tilde{p}_{45}) Q_6(p_6) W(P_W)$
$\mathcal{D}_{45,6}$:	$q_a(p_1) Q_c(p_2) \rightarrow q_b(p_3) g(\tilde{p}_{45}) Q_6(\tilde{p}_6) W(P_W)$

Table 3.3: Dipoles for $\bar{q}_a(p_1) \bar{Q}_c(p_2) \rightarrow \bar{q}_b(p_3) \bar{Q}_d(p_4) \bar{q}'_5(p_5) q'_6(p_6) W(P_W)$ processes and the corresponding Born kinematics. Depending on the flavours of the quarks not all dipoles contribute.

Colour structure 1 dipoles	
Dipole	Born kinematic
\mathcal{D}_5^{13}	$g(\tilde{p}_{13}) \bar{Q}_c(p_2) \rightarrow \bar{Q}_d(p_4) \bar{q}_5(\tilde{p}_5) q_6(p_6) W(P_W)$
\mathcal{D}_6^{13}	$g(\tilde{p}_{13}) \bar{Q}_c(p_2) \rightarrow \bar{Q}_d(p_4) \bar{q}_5(p_5) q_6(\tilde{p}_6) W(P_W)$
\mathcal{D}_{56}^1	$\bar{q}_a(\tilde{p}_1) \bar{Q}_c(p_2) \rightarrow \bar{q}_b(p_3) \bar{Q}_d(p_4) g(\tilde{p}_{56}) W(P_W)$
$\mathcal{D}_{56,3}$	$\bar{q}_a(p_1) \bar{Q}_c(p_2) \rightarrow \bar{q}_b(\tilde{p}_3) \bar{Q}_d(p_4) g(\tilde{p}_{56}) W(P_W)$
\mathcal{D}_3^{15}	$g(\tilde{p}_{15}) \bar{Q}_c(p_2) \rightarrow \bar{q}_b(\tilde{p}_3) \bar{Q}_d(p_4) q_6(p_6) W(P_W)$
\mathcal{D}_6^{15}	$g(\tilde{p}_{15}) \bar{Q}_c(p_2) \rightarrow \bar{q}_b(p_3) \bar{Q}_d(p_4) q_5(\tilde{p}_6) W(P_W)$
\mathcal{D}_{36}^1	$\bar{q}_a(\tilde{p}_1) \bar{Q}_c(p_2) \rightarrow g(\tilde{p}_{36}) \bar{Q}_d(p_4) \bar{q}_5(p_5) W(P_W)$
$\mathcal{D}_{36,5}$	$\bar{q}_a(p_1) \bar{Q}_c(p_2) \rightarrow g(\tilde{p}_{36}) \bar{Q}_d(p_4) \bar{q}_5(\tilde{p}_5) W(P_W)$
Colour structure 2 dipoles	
Dipole	Born kinematic
\mathcal{D}_5^{24}	$\bar{q}_a(p_1) g(\tilde{p}_{24}) \rightarrow \bar{q}_b(p_3) \bar{Q}_5(\tilde{p}_5) Q_6(p_6) W(P_W)$
\mathcal{D}_6^{24}	$\bar{q}_a(p_1) g(\tilde{p}_{24}) \rightarrow \bar{q}_b(p_3) \bar{Q}_5(p_5) Q_6(\tilde{p}_6) W(P_W)$
\mathcal{D}_{56}^2	$\bar{q}_a(p_1) \bar{Q}_c(\tilde{p}_2) \rightarrow \bar{q}_b(p_3) \bar{Q}_d(p_4) g(\tilde{p}_{56}) W(P_W)$
$\mathcal{D}_{56,4}$	$\bar{q}_a(p_1) \bar{Q}_c(p_2) \rightarrow \bar{q}_b(p_3) \bar{Q}_d(\tilde{p}_4) g(\tilde{p}_{56}) W(P_W)$
\mathcal{D}_4^{25}	$\bar{q}_a(p_1) g(\tilde{p}_{25}) \rightarrow \bar{q}_b(p_3) \bar{Q}_d(\tilde{p}_4) Q_6(p_6) W(P_W)$
\mathcal{D}_6^{25}	$\bar{q}_a(p_1) g(\tilde{p}_{25}) \rightarrow \bar{q}_b(p_3) \bar{Q}_d(p_4) Q_6(\tilde{p}_6) W(P_W)$
\mathcal{D}_{46}^2	$\bar{q}_a(p_1) \bar{Q}_c(\tilde{p}_2) \rightarrow \bar{q}_b(p_3) g(\tilde{p}_{46}) \bar{Q}_5(p_5) W(P_W)$
$\mathcal{D}_{46,5}$	$\bar{q}_a(p_1) \bar{Q}_c(p_2) \rightarrow \bar{q}_b(p_3) g(\tilde{p}_{46}) \bar{Q}_5(\tilde{p}_5) W(P_W)$

3.4 Virtual Corrections

The virtual corrections for the NLO QCD calculation of the W_{jjj} process are given by diagrams of the form of the Born-level graphs with one additional gluon loop as well as quark loop diagrams. The latter include quark triangle and box graphs and are not considered in this calculation by reasoning that they are suppressed by a factor of $1/N$ compared to the gluon loop diagrams. In addition, most diagrams including a quark triangle cancel when taking the sum over all diagrams. Regarding the gluon loop corrections, no diagrams with the virtual gluon connecting upper and lower line are considered due to the VBF approximation. As a consequence, the virtual amplitude can be divided into two sets, one with the gluon loop being attached to the upper line and one with the gluon loop being attached to the lower line. Analogously to the Born matrix element

$$\mathcal{M}_B = \delta_{lk} t_{ji}^a \mathcal{M}_B^{\text{cs1}} + \delta_{ji} t_{lk}^a \mathcal{M}_B^{\text{cs2}}, \quad (3.32)$$

the virtual one can be written as

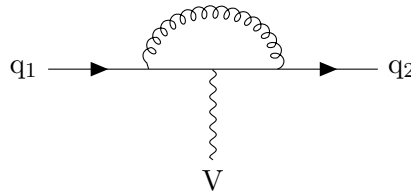
$$\mathcal{M}_V = \delta_{lk} t_{ji}^a \mathcal{M}_V^{\text{cs1}} + \delta_{ji} t_{lk}^a \mathcal{M}_V^{\text{cs2}}, \quad (3.33)$$

with colour charges i, j of quarks 1, 3 and k, l of quarks 2, 4, respectively, and a being the colour index of the external gluon. The calculation of the corrections to one line is identical to the one for the other line, which is why in the following only corrections to the upper line, line $q_1 q_3$ or colour structure 1, are explained in detail.

The one-loop virtual corrections can further be classified into three topologies:

1. Corrections to quark lines with one gauge boson attached;
2. Corrections to quark lines with two gauge bosons attached;
3. Corrections to quark lines with three gauge bosons attached.

In the first case, the considered quark line is an empty line and the attached boson is the electroweak exchange current between the two quark lines. There exists only one correction diagram for this case, which is the vertex correction



For the second topology, the one-loop diagrams in Figure 3.9 contribute independent of the kind of the second boson. If the second boson is the emitted W boson, no further

correction diagrams exist for this case. If it is a gluon, there are additional non-abelian box and gluon vertex correction diagrams as shown in Figure 3.10.

In case 3, both the emitted W boson and the gluon couple to the considered quark line, giving two propagator corrections, three vertex corrections, two box graphs and one pentagon correction, along with non-abelian graphs, all shown in Figure 3.11. The colour algebra of a line with a gluon loop in abelian diagrams gives

$$t_{jl_1}^a t_{l_1 l_2}^c t_{l_2 i}^c = t_{jl_1}^a (t^c t^c)_{l_1 i} = C_F t_{ji}^a \quad (3.34)$$

for a diagram with the external gluon being emitted outside the loop (like the one in Figure 3.11(a)), and

$$t_{jl_1}^c t_{l_1 l_2}^a t_{l_2 i}^c = (t^c t^a t^c)_{ji} = \left(C_F - \frac{C_A}{2} \right) t_{ji}^a \quad (3.35)$$

for a diagram with the external gluon being attached to the loop (like the one in Figure 3.10), meaning an additional factor of C_F or $C_F - C_A/2$, while non-abelian diagrams give

$$i t_{jl}^c t_{li}^b f^{abc} = [t^a, t^b]_{jl} t_{li}^b = \frac{C_A}{2} t_{ji}^a, \quad (3.36)$$

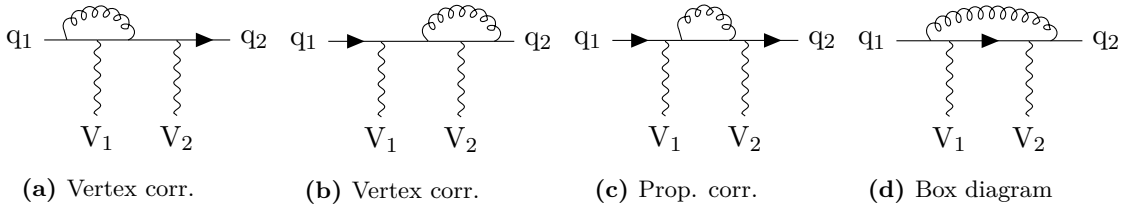


Figure 3.9: Corrections to a line with two electroweak gauge bosons attached. For a line with the electroweak current and gluon attached, the same diagrams appear in addition to the non-abelian diagrams in Figure 3.10.

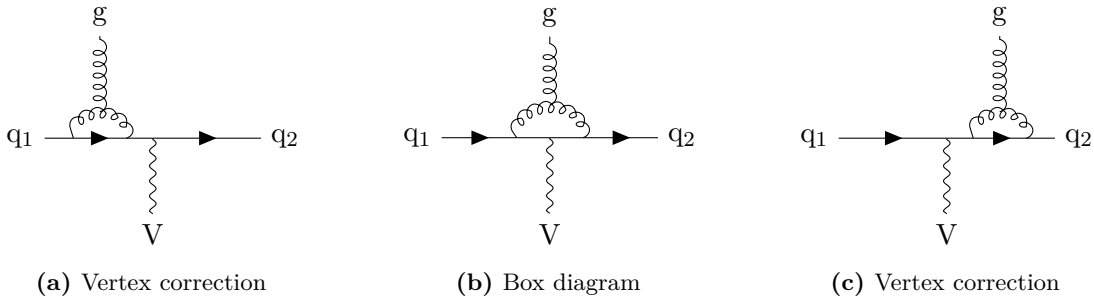


Figure 3.10: Additional non-abelian diagrams for a quark line coupling to a gluon and an electroweak current. These include all non-abelian corrections corresponding to Born graphs with the gluon being emitted before the electroweak current as well as those with the gluon being emitted after the electroweak current.

so an additional factor of $C_A/2$. Here, the identities and relations in Equations 2.20, 2.21 and 2.22 were used.

While the calculation of the vertex correction of the first topology does not need much effort since it is proportional to the corresponding Born graph, the other two topologies include various graphs up to boxes and pentagons, which have to be evaluated for all possible sequences of attached vector bosons. To simplify the calculation of all necessary correction graphs in VBFNLO, loop routines that calculate all diagrams of one topology for a given sequence of bosons are used. These have been implemented for NLO corrections to single (second topology) and double (third topology) vector boson production with two jets via VBF, $pp \rightarrow VVjj$ [52]. They can be used universally since they do not include coupling

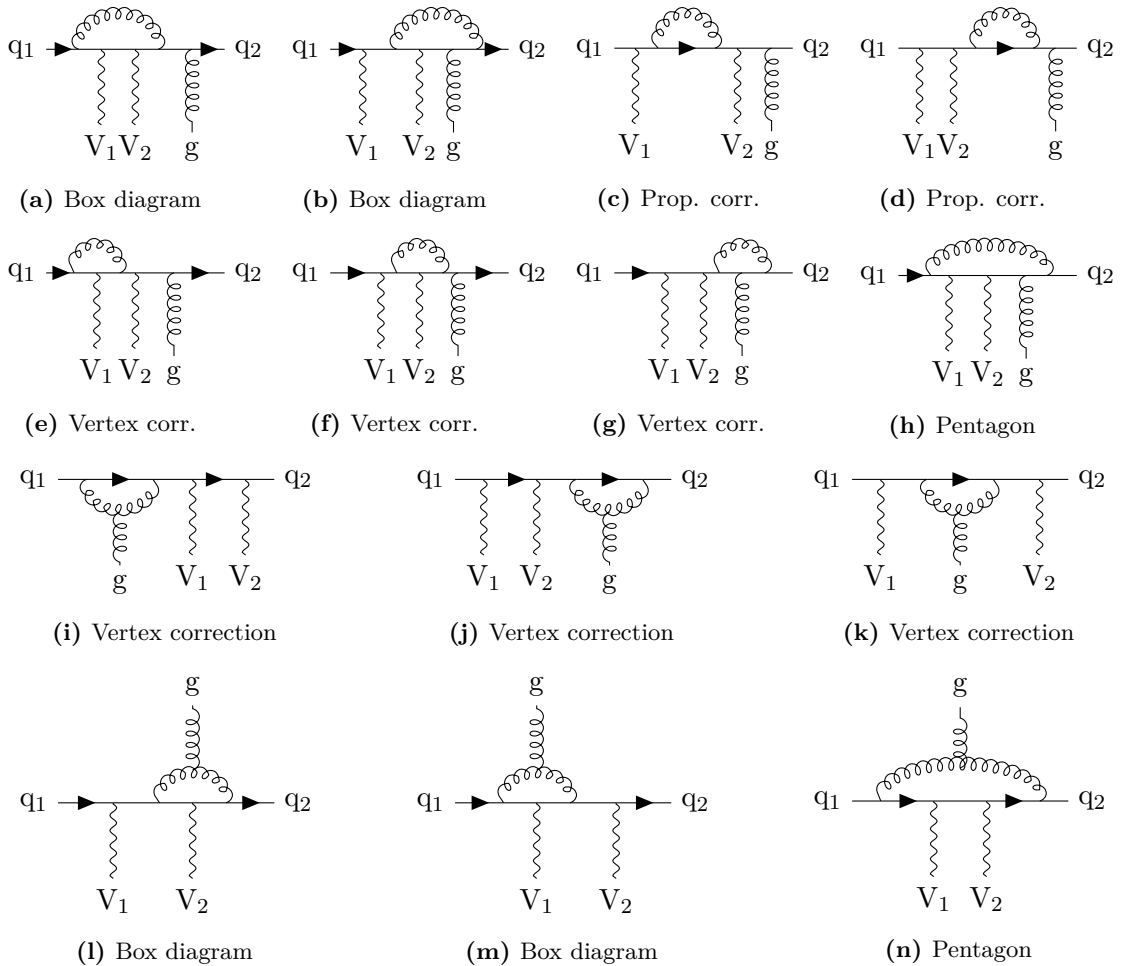


Figure 3.11: Corrections to a line with three gauge bosons attached. (a) to (h) give the abelian corrections for an emission sequence with the gluon being emitted last, while the non-abelian corrections in (i) to (n) correspond to Born graphs with the gluon being emitted at any position of the line (before, in between or after the two electroweak bosons).

factors, instead using a general coupling of vector bosons of γ_μ , and use the helicity of the quarks as input parameter. They further use generic effective currents as input, which can be both on- and off-shell polarisation vectors, or for example a current that includes another quark line, etc.

The abelian graphs of the second topology, Figure 3.9, are calculated with the `boxlineAbeTotal` routine. If one of the attached currents is a gluon, its position also has to be passed to the routine to distinguish the different colour structures, and the additional colour factor (Equations 3.34 to 3.36) has to be multiplied to the routine result. In addition, non-abelian diagrams have to be calculated by calling the routine `boxlineNoAbeTotal`. This routine computes all three diagrams shown in Figure 3.10, meaning both the ones corresponding to Born graphs where the gluon is emitted before and those where it is emitted after the electroweak current. For one call of this routine thus two calls with different sequence of gluon and electroweak current of `boxlineAbeTotal` have to be made.

Graphs of the third topology are computed via the `penlineAbeTotal` (graphs in Figures 3.11(a) to (h)) and `penlineNoAbeTotal` (Figures 3.11(i) to (n)) routines, that include all the corrections to a line with three vector bosons, meaning self-energy graphs, vertex corrections, boxes and pentagon graphs. Analogously to the abelian `boxline` routine, the position of the gluon for the abelian correction has to be passed to the abelian `penline` routine, while the non-abelian one sums the corrections to one line corresponding to Born graphs with the gluon being attached at any position of that line.

The actual calculation of the loop integrals done in the implemented routines is described in detail in Reference [52]. These one-loop calculations with multiple legs attached yield tensor integrals that have to be reduced. Such a tensor reduction is commonly done via the method of Passarino and Veltman [53], which computes the inverse of Gram and Cayley determinants in order to solve high-dimensional linear equations. However, this causes unstable results for small determinants, which is why an improved method using the LU decomposition [54, 55] method and following Reference [56] is implemented, which avoids these singularities by solving the appearing linear equations numerically. In addition, Ward identity tests are implemented which for each call of the routines check for instabilities. For the newly implemented Wjjj process it was tested that by neglecting the contributions of the loop calculations for unstable points this leads to an error in the total cross section of less than one per mill.

3.4.1 Subtraction of Infrared Singularities

The result obtained for the virtual correction matrix elements includes a finite part and a divergent part,

$$\mathcal{M}_V^{csi} = \mathcal{M}_{V,\text{div}}^{csi} + \tilde{\mathcal{M}}_V^{csi}, \quad (3.37)$$

with tilde denoting the finite part. Since all ultraviolet divergences have been handled in the loop routines by renormalisation, the divergent part solely contains infrared singularities. These are subtracted via the method by Catani and Seymour. As explained in Section 2.3.2,

the insertion operator needed for the subtraction has a process-independent form, given by Equation 2.54. The colour structure of this process in the VBF approximation – meaning the two quark lines are considered as belonging to different colour algebras – is similar to two independent processes, one involving two quarks and one gluon (e.g. $q_1 \rightarrow q_3g$), the other resembling a single quark line ($q_2 \rightarrow q_4$), meaning the insertion operator also splits into two parts proportional to the Born amplitudes of different colour structures. With the identities for the colour charge operators given in Equation 2.58 and colour conservation, the insertion operator applied to the Born matrix elements for the example of a subprocess with outgoing gluon thus simplifies to

$$\begin{aligned}
\langle \mathcal{J}(\varepsilon) \rangle = & |\mathcal{M}_B^{\text{cs1}}(p_1 p_2 \rightarrow p_3 p_4 p_5)|^2 \frac{C_F \alpha_s}{2\pi} \frac{(4\pi\mu^2)^\varepsilon}{2 \cdot \Gamma(1-\varepsilon)} \\
& \cdot \left\{ \mathcal{V}_q(\varepsilon) \left[2 \left(\frac{1}{p_2 \cdot p_4} \right)^\varepsilon + \frac{1}{2} \left(\frac{1}{p_1 \cdot p_3} \right)^\varepsilon + \frac{C_A}{2C_F} \left(\left(\frac{1}{p_1 \cdot p_5} \right)^\varepsilon + \left(\frac{1}{p_3 \cdot p_5} \right)^\varepsilon \right) \right] \right. \\
& \left. + \frac{1}{2} \mathcal{V}_g(\varepsilon) \left[\left(\frac{1}{p_1 \cdot p_5} \right)^\varepsilon + \left(\frac{1}{p_3 \cdot p_5} \right)^\varepsilon \right] \right\} \\
& + |\mathcal{M}_B^{\text{cs2}}(p_1 p_2 \rightarrow p_3 p_4 p_5)|^2 \frac{C_F \alpha_s}{2\pi} \frac{(4\pi\mu^2)^\varepsilon}{2 \cdot \Gamma(1-\varepsilon)} \\
& \cdot \left\{ \mathcal{V}_q(\varepsilon) \left[2 \left(\frac{1}{p_1 \cdot p_3} \right)^\varepsilon + \frac{1}{2} \left(\frac{1}{p_2 \cdot p_4} \right)^\varepsilon + \frac{C_A}{2C_F} \left(\left(\frac{1}{p_2 \cdot p_5} \right)^\varepsilon + \left(\frac{1}{p_4 \cdot p_5} \right)^\varepsilon \right) \right] \right. \\
& \left. + \frac{1}{2} \mathcal{V}_g(\varepsilon) \left[\left(\frac{1}{p_2 \cdot p_5} \right)^\varepsilon + \left(\frac{1}{p_4 \cdot p_5} \right)^\varepsilon \right] \right\}, \tag{3.38}
\end{aligned}$$

with \mathcal{V}_i , γ_i and K_i defined as in Section 2.3.2. The divergent terms cancel with the divergent terms of the virtual contributions, leaving only finite terms to be added to the total amplitude,

$$\begin{aligned}
2\text{Re} [\mathcal{M}_V^* \mathcal{M}_B] + \langle \mathcal{J}(\varepsilon) \rangle = & F_1 \cdot |\mathcal{M}_B^{\text{cs1}}(p_1 p_2 \rightarrow p_3 p_4 p_5)|^2 + F_2 \cdot |\mathcal{M}_B^{\text{cs2}}(p_1 p_2 \rightarrow p_3 p_4 p_5)|^2 \\
& + C_F \left(2\text{Re} \left[(\tilde{\mathcal{M}}_V^{\text{cs1}})^* \mathcal{M}_B^{\text{cs1}} \right] + 2\text{Re} \left[(\tilde{\mathcal{M}}_V^{\text{cs1}})^* \mathcal{M}_B^{\text{cs2}} \right] \right), \tag{3.39}
\end{aligned}$$

where the prefactors F_i depend on the parton momenta.

3.5 Finite Collinears

Besides the real emissions and virtual corrections, there is an additional contribution to the NLO part of the cross section for this process as it includes two partons in the initial state. As explained in Section 2.3.2, the additional initial collinear singularities arising from these partons are absorbed in the PDFs, leaving only a finite collinear remainder whose

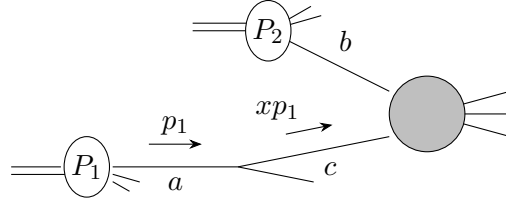
contribution to the cross section is given by (see also Equation 2.53)

$$\sigma^{\text{C}} = \sum_{a,b} \int_0^1 dx_1 \int_0^1 dx_2 f_{a/P_1}(x_1, \mu_{\text{F}}) f_{b/P_2}(x_2, \mu_{\text{F}}) \int_m d\hat{\sigma}_{a,b}^{\text{C}}(\mu_{\text{F}}). \quad (3.40)$$

The labels a and b refer to the incoming partons of the contributing partonic subprocesses and carry momenta $p_1 = x_1 P_1$ and $p_2 = x_2 P_2$, respectively, with P_i denoting the momenta of the incoming hadrons. The differential term can be written as [44, pp. 11, 47, 105]¹

$$\begin{aligned} d\hat{\sigma}_{a,b}^{\text{C}}(p_1, p_2; \mu_{\text{F}}) = & \int_0^1 dz \sum_c \left\{ \left[\mathcal{P}^{a,c}(z, zp_1, p_2, \mu_{\text{F}}) + \mathcal{K}^{a,c}(z) \right] \otimes d\hat{\sigma}_{c,b}^{\text{B}}(zp_1, p_2) \right. \\ & \left. + \left[\mathcal{P}^{c,b}(z, p_1, zp_2, \mu_{\text{F}}) + \mathcal{K}^{c,b}(z) \right] \otimes d\hat{\sigma}_{a,c}^{\text{B}}(p_1, zp_2) \right\}. \end{aligned} \quad (3.41)$$

The first line corresponds to a collinear splitting of parton a into parton c , which then interacts with parton b from another hadron in the so-called hard process giving the Born amplitude $|\mathcal{M}_{\text{B}}|^2$, which can be illustrated as follows (modified according to [57]):



Analogously, the second line gives the contribution from parton b splitting into c , which then enters the hard scattering process with parton a .

After folding $d\hat{\sigma}_{a,b}^{\text{C}}$ with the PDFs of partons a and b and inserting the explicit expressions of \mathcal{P} and \mathcal{K} , expressions for the differential finite collinear remainder for the several combinations of incoming partons can be found. Since these are rather lengthy and identical to the ones for Hjjj production which has the same QCD structure, the detailed expressions are not given here, but interested readers are referred to Reference [51].

In the program, the finite collinear terms are added to the virtual correction terms before being integrated over the Born phase space. For each phase space point a new random number has to be generated due to the additional z integration.

¹ One might take notice of the fact that in the here considered case the two incoming partons belong to separate colour algebras, thus the formula of Reference [44] for one initial state hadron has to be used.

CHAPTER 4

Verification

The implementation of the W_{jjj} cross section calculation at NLO was tested on various levels of the calculation to assure its correctness. The Born and real emission matrix elements were compared to matrix elements calculated by code that was generated by MADGRAPH. The LO calculation was crosschecked at the level of its integrated cross section with already existing and validated results. To the author's knowledge, there does not exist another calculation for the total NLO cross section of W production via vector boson fusion in association with three jets, but tests of the several building blocks of the calculation ensure a correct total result. Besides the real emission matrix elements these include tests of the dipole subtraction terms and of the loop routines as well as virtual matrix elements for the calculation of virtual corrections. Moreover, the simplification to introduce a cut on the virtuality of a t -channel photon to remove singularities has been justified with an estimation of the thereby lost contribution to the cross section.

4.1 Matrix Elements

4.1.1 Comparison of Matrix Elements with MADGRAPH

MADGRAPH [58] generates FORTRAN code and Feynman graphs for tree level amplitudes. The generated code calls HELAS subroutines to calculate each graph contributing to the process separately. For the comparison in this thesis, code generated by MADGRAPH II is used. To compare specific matrix elements, a correct helicity basis has to be constructed as MADGRAPH uses circular polarisation in contrast to VBFNLO. The sum over helicities of the squared matrix elements can be compared without modifications. As MADGRAPH also includes s -channel contributions and interference between the two quark lines, processes involving different quark generations, such as $d s \rightarrow d c g l^- \bar{\nu}_l$, are generated. These include the same contributions as the VBF approximation, since MADGRAPH also neglects CKM mixing.

The deviation between the squared LO matrix elements calculated by MADGRAPH and the newly implemented ones in VBFNLO,

$$\Delta_B = \left| \frac{|\mathcal{M}_{B, \text{MADGRAPH}}|^2 - |\mathcal{M}_{B, \text{VBFNLO}}|^2}{|\mathcal{M}_{B, \text{MADGRAPH}}|^2} \right|, \quad (4.1)$$

is below $3 \cdot 10^{-7}$ for all $2 \cdot 10^6$ matrix elements tested each for W^-jjj and for W^+jjj at randomly chosen phase space points. The logarithm to base 10 of Δ_B is approximately normally distributed with mean at -12.8 and standard deviation of 1.3 , so the results are in agreement up to statistical errors due to the numerical calculation.

For the real emission calculation, all two-gluon and six-quark subprocesses were tested both for W^+ and W^- , each subprocess class for a sample of $2 \cdot 10^6$ squared matrix elements. The relative difference Δ_R to the MADGRAPH results does not exceed $5 \cdot 10^{-7}$ for the two-gluon subprocess matrix elements, with a mean of -12.7 of the logarithmic distribution. The logarithmic distribution of the six-quark subprocess matrix elements has a mean of -12.0 with standard deviation of 1.5 .

4.1.2 Virtual Correction Matrix Elements

The calculation of the virtual correction matrix elements is based on loop routines that have already been implemented in VBFNLO, see Section 3.4. Their correctness has been assured with extensive tests explained in Reference [52]. To further verify their correct integration in the newly implemented program, a crosscheck with virtual matrix elements of the already existing code for $Zjjj$ production at QCD NLO [59] has been performed. By adjusting parameters of the electroweak theory, the couplings of the Z boson can be matched to those of the W boson, while the couplings of the photon are concurrently set to zero. With this adjustment, linear combinations of matrix element contributions of different flavour combinations can be found for which the process with final state observable $Zjjj$ shall give the same result as the $Wjjj$ process.¹ For these linear combinations l the relative difference

$$\Delta\mathcal{M}_{V,l} = \frac{|\mathcal{M}_V^{W,l} - \mathcal{M}_V^{Z,l}|}{|\mathcal{M}_V^{W,l}|} \quad (4.2)$$

has been calculated. For linear combinations only including diagrams with W/Z boson emitted from a quark leg, the relative difference is exactly zero. For linear combinations including leptonic tensor diagrams, the maximum difference is of the order 10^{-6} , with mean of the logarithmic distribution to base 10 at -11.7 . This difference is due to a dependence of results calculated with HELAS on the order in which the several partial results are calculated, which is the case for the leptonic tensors, while the results of diagrams with leg emissions are in both programs calculated using only `braket` routines. This suggests a better accuracy and precision of the `braket` routines in comparison to HELAS.

¹ These contributions include all diagrams with *either* leptonic tensor *or* leg emission of W/Z boson, since no linear combination of the complete matrix elements (including both LT and CC/NC diagrams) of different flavour combinations can be found for which $Wjjj$ and $Zjjj$ are identical.

4.2 Integrated LO Cross Section

As mentioned in Section 3.1, implementations of NLO cross section calculations in VBFNLO allow to calculate the corresponding processes with one additional jet at LO. Thus, the integrated LO cross section for $Wjjj$ can be crosschecked with the real emission (without NLO) cross section of the previously implemented and extensively validated Wjj process. This was done for W^-jjj as well as W^+jjj for the cuts and parameters listed in Section 5.1, except for the renormalisation and factorisation scale which was chosen constant at 100 GeV.¹ All processes were run over 2^{24} phase space points from which about 30% passed the cuts and gave a nonzero contribution. The cross sections are in full agreement within statistical fluctuations, both processes giving (175.843 ± 0.294) fb for W^-jjj production and (310.782 ± 0.516) fb for W^+jjj production, with their relative deviation

$$\Delta\sigma = \left| \frac{\sigma(\text{pp} \rightarrow Wjj)_{\text{RE}}}{\sigma(\text{pp} \rightarrow Wjj)_{\text{LO}}} - 1 \right| \quad (4.3)$$

being of the order 10^{-15} .

4.3 Dipole Subtraction Terms

In Section 3.3.3 the construction of dipole subtraction terms following the method proposed by Catani and Seymour to remove infrared and collinear divergences in the real emission cross section is explained. The sum over all dipole configurations for a specific flavour subprocess should in the soft ($p_i^\mu = \lambda q^\mu$, $\lambda \rightarrow 0$) and collinear ($p_i^\mu \parallel p_j^\mu$) limit exactly reproduce the singularities of the corresponding squared real emission amplitude to annihilate the divergent contribution to the cross section in Equation 3.27, that is

$$R := \left| \frac{\sum_{m=1}^{n_d} \mathcal{D}(m) - \overline{\sum} |\mathcal{M}_R|^2}{\overline{\sum} |\mathcal{M}_R|^2} \right| \xrightarrow{\lambda, p_i \cdot p_j \rightarrow 0} 0. \quad (4.4)$$

This quantity was checked separately for soft and collinear phase space points and for the different subprocess classes. Soft singularities only appear for subprocesses with a final state gluon, that is for the two-gluon subprocesses with both gluons being final as well as the ones with one initial gluon. The resulting normalised difference R over the energy of a final gluon normalised to the minimum energy of the initial partons, $E_{\min} := \min(E_1, E_2)$, is shown in Figure 4.1. R behaves as expected for small gluon energies E_g .

The collinear limit exists for all subprocesses and is tested separately for initial state and final state radiation, which corresponds to the emitter being an initial or final parton, respectively. Both cases are tested by examining quantities that are invariant under boosts

¹ At LO, these cuts and parameters affect only the phase space generation, coupling constant, PDFs, etc. Thus, both implementations are affected by a change of these parameters in the same way, which is why a test at one set of these is sufficient.

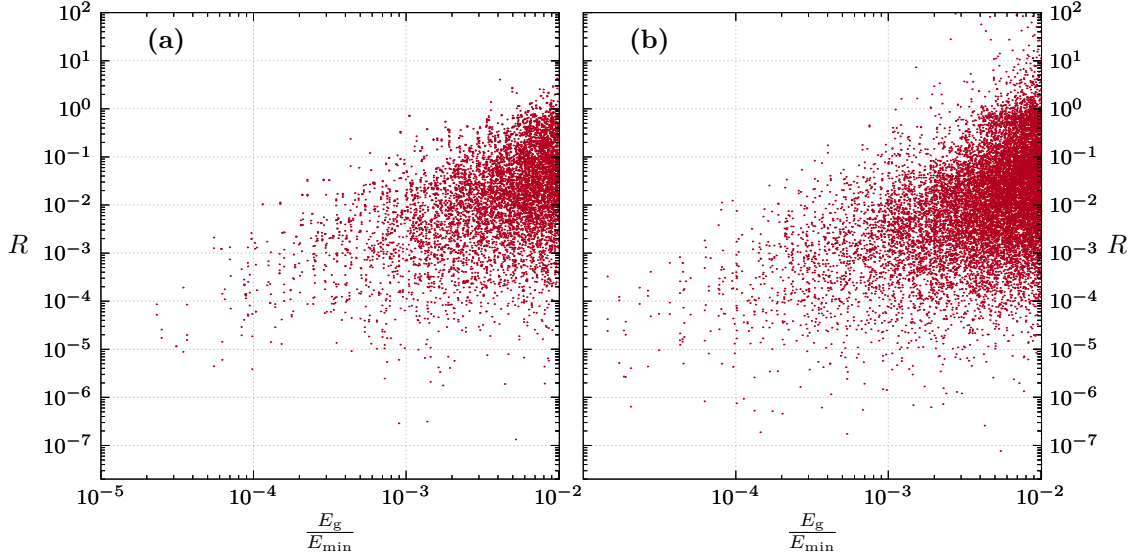


Figure 4.1: Normalised difference R between dipole terms and squared real emission amplitude for small final gluon energies. **(a)** shows the R for subprocesses with both gluons being final, **(b)** for the ones with one final state gluon. As expected, R approximates zero in the soft limit.

along the beam axis. For initial state radiation, where an emitted final parton may be collinear to the emitting initial one, the maximal rapidity $y_{\max} := \max(|y_i|)$ of all final partons is used as a measure scale for collinearity, which for massless particles coincides with its pseudorapidity

$$\eta = y := \frac{1}{2} \ln \left(\frac{E + p_z}{E - p_z} \right), \quad (4.5)$$

with p_z being the momentum component along the beam axis. For final state radiation, where two final partons may become collinear, the angular separation of a parton pair,

$$\Delta R_{ij} := \sqrt{(y_i - y_j)^2 + (\varphi_i - \varphi_j)^2}, \quad (4.6)$$

with azimuthal angle $\varphi_i = \arctan(p_y/p_x)$, is used as collinearity scale. In both cases, the tested phase space points had to pass the cuts of Section 5.1 that provide for at least three jets to form from the four final partons. In addition, restrictions were made demanding the considered phase space points for the initial dipole tests to not include partons with angular separation of $\Delta R_{ij} < 0.5$ ¹, and for the final dipole tests to not include a final parton of rapidity $y \geq 4.5$ (besides *not more than one* parton pair having $\Delta R_{ij} < 0.5$)¹. For the subprocesses with final gluons also phase space points with these gluons being

¹ For all parton pairs that can potentially cause a singularity when becoming collinear. This means that for ΔR_{34} for example no restriction is made in any subprocess.

soft have been excluded for the tests. These restrictions ensure that for the specific tests no additional singularity of another kind enters. Since the momentum configurations of a specific dipole kinematic have to pass the overall cuts also, these restrictions make it possible to control that all kinematics needed to subtract the considered kind of singularity pass these cuts and are calculated. If not, points with R being 1, 0.75, 0.5, and 0.25 appear, as it lacks a fraction of the needed subtraction terms.

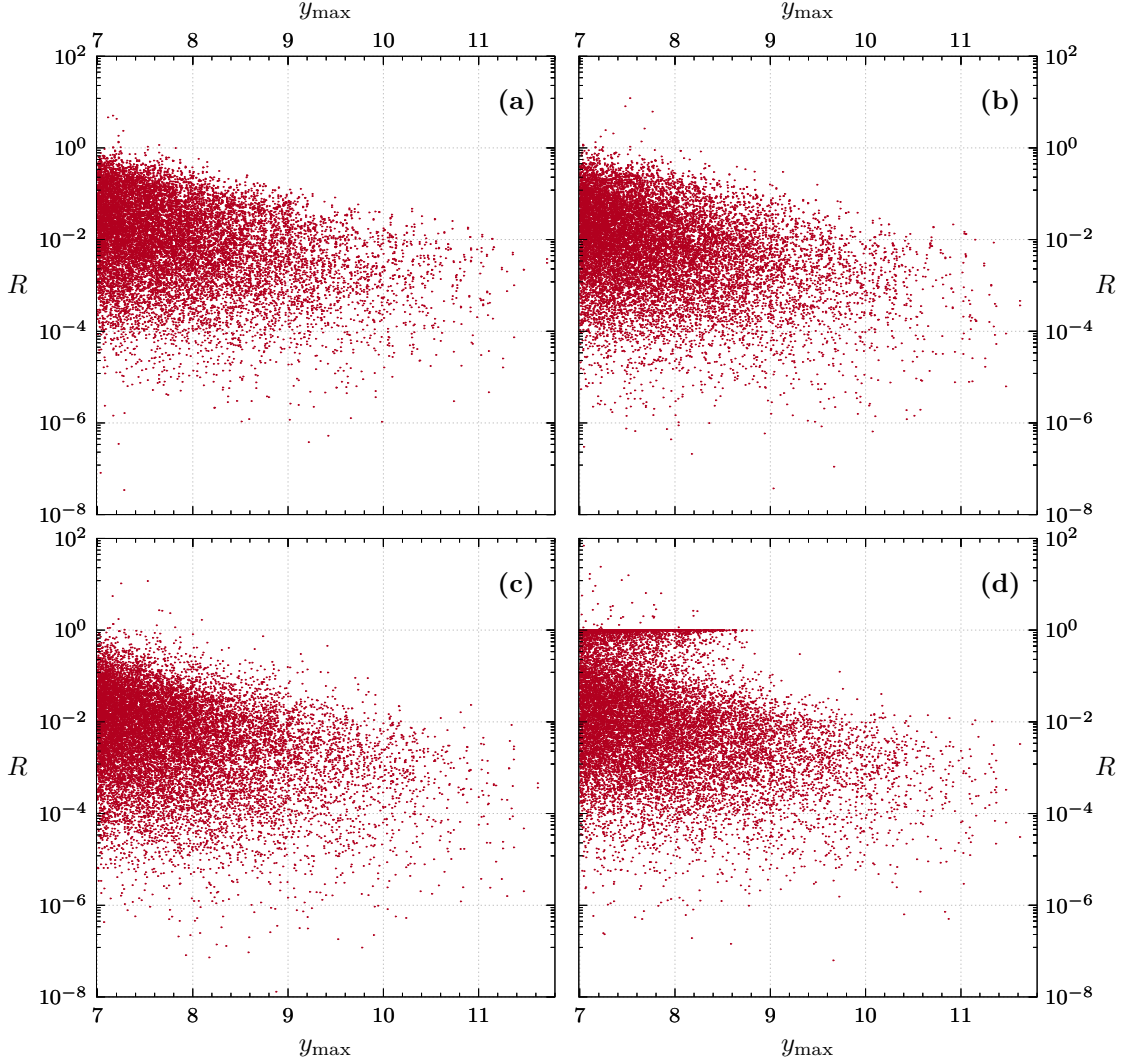


Figure 4.2: Normalised difference R for large rapidities of a final parton, meaning this parton becomes collinear to an initial state parton. (a) shows R for subprocesses with two final gluons, (b) for the ones with one initial state gluon and (c) for the subprocess with both gluons being initial. In the graph of the six-quark subprocesses, (d), a line at $R = 1$ appears, implying that not all singularities are cancelled by the dipole terms. The results of Figure 4.3 show that this is caused by divergent t -channel photon propagators which are handled by the cut on the photon virtuality.

The results of the tests of dipole terms for collinear singularities resulting from initial state radiation are shown in Figure 4.2 for all four subprocess classes. For the six-quark subprocesses, singular phase space points seem to exist where the dipole terms do not exactly cancel the divergence, leading to a straight line at $R \approx 1$. These points are due to the cut on the photon virtuality and are therefore caused by phase space points where particles 1 and 3 or 2 and 4 are collinear. In Figure 4.3 the cut on the photon virtuality was set to 30 GeV^2 , causing the line to vanish above a considerably lower value of y_{max} than before. In the two-gluon subprocesses, such points do not appear, since singularities in a quark or gluon propagator always involve at least one gluon becoming collinear to another parton, meaning at least three particles couple to this quark line. Thus, its total invariant mass cannot be singular (because of the cuts), causing the exchanged photon propagator to be off-shell.¹

There are also points where R gets much larger than 1, meaning the dipole terms are much larger than the real emission matrix element. They originate from phase space points where dipole terms of other kinematics than the one cancelling the singularity are large. This phenomenon has not been studied thoroughly so far, but similar tests with the dipole terms of the Hjjj process implementation [50, 51] – which has been verified up to the level of the integrated NLO cross section – show the same results. Consequently, this behaviour

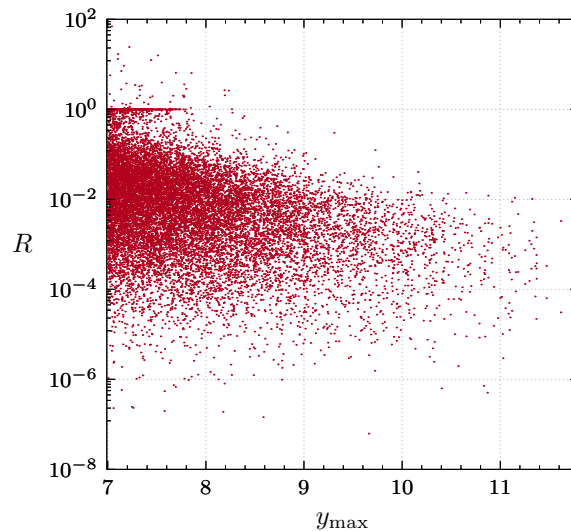


Figure 4.3: By setting the cut on the photon virtuality to 30 GeV^2 , the points at $R = 1$ stop to appear at a lower y_{max} than the ones in Figure 4.2(d), leading to the conclusion that these points are solely caused by singularities in the propagator of an exchanged t -channel photon.

¹ The only scenario where the photon virtuality cut is necessary for these processes is when particles 1 and 3 or 2 and 4 are both quarks and become collinear, but in this case no quark or gluon propagator diverges, which is relevant for the test of the dipole subtraction terms, meaning those points are not included in the shown figures.

is not connected to a failure of the newly implemented dipole subtraction terms.

In Figure 4.4, the results for the test of final state radiation dipoles are shown, which do not appear in the subprocesses with two initial gluons. Like for the initial state radiation dipoles, the dipole terms of the six-quark subprocesses contain points with R deviating from the expected result. In order to ensure that this behaviour is not correlated to an incorrect calculation of the subtraction terms, the same test was run for the above mentioned Hjjj

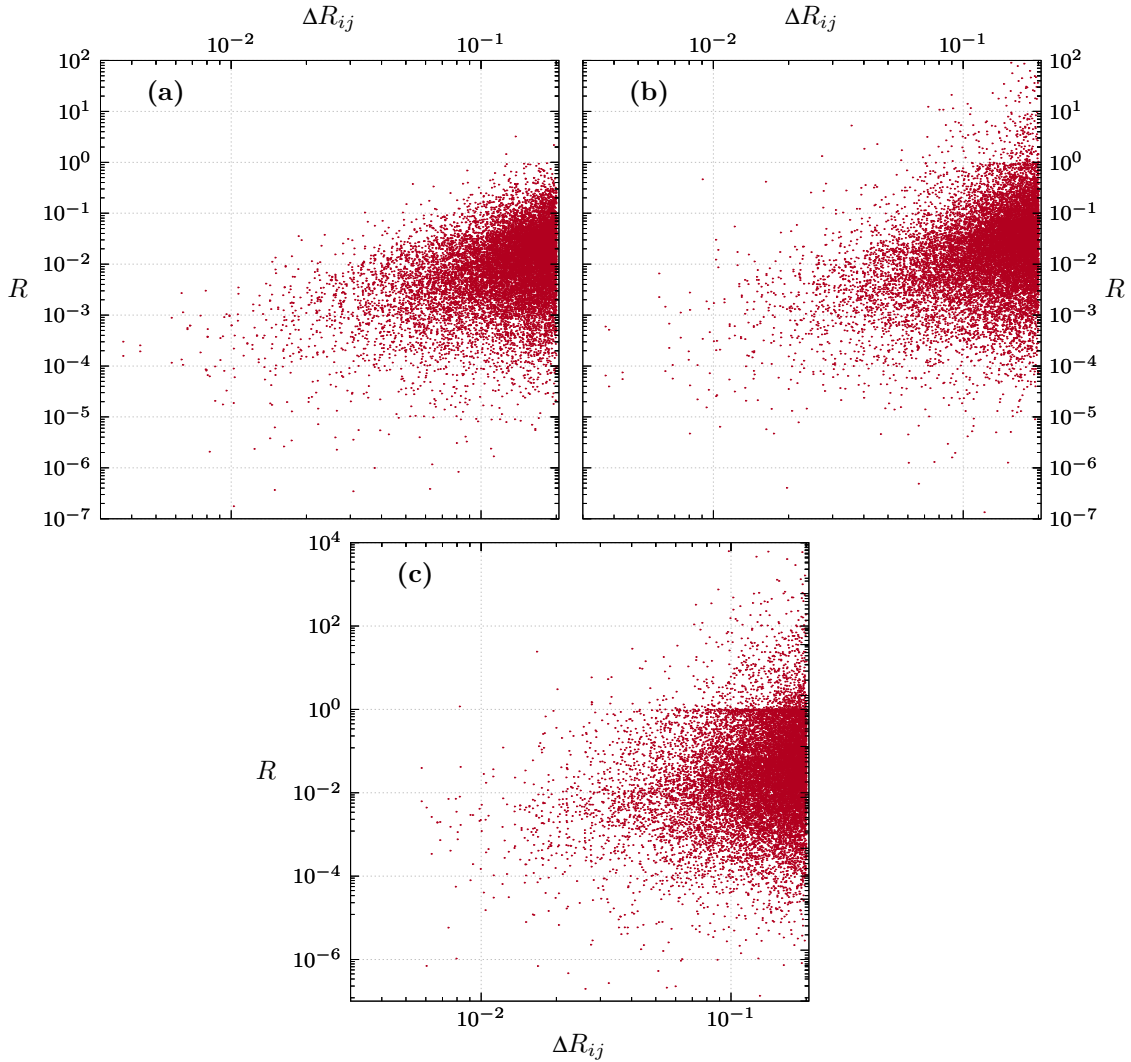


Figure 4.4: Normalised difference between dipole terms and squared real emission amplitude in dependence of the angular separation of a parton pair, meaning for final state singularities. The definition of the quantities and cuts to ensure no other singularities occur for these points are given in the text. Again, (a) shows R for subprocesses with two final gluons, (b) for the ones with one initial state gluon and (c) for the six-quark subprocesses. In the subprocess with both gluons being initial, no final state singularities exist.

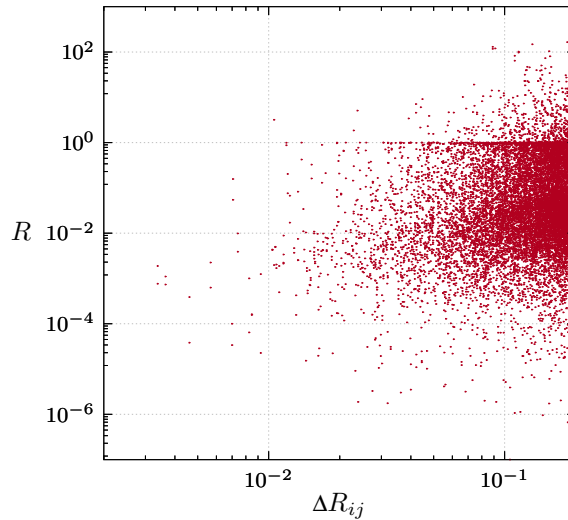


Figure 4.5: Test results for final state collinear singularities in the six-quark subprocesses of the Hjjj process, which show the same behaviour as observed in Figure 4.4(c) for the Wjjj process.

implementation. The results are shown in Figure 4.5, and reproduce the unanticipated behaviour of the dipole terms of the newly implemented Wjjj process. Nevertheless, it would be interesting for future examinations to clarify this unexpected behaviour of the dipole subtraction terms and its origin.

4.4 Influence of the Photon Virtuality Cut

In Section 3.3.3 a cut on the virtuality $Q^2 = -t$ of a t -channel current was imposed in diagrams like the one on the left of Figure 3.8, which correspond to electroweak correction diagrams to processes with an initial photon, like the one on the right of the same figure. The cut was set at $Q_{\min}^2 = 4 \text{ GeV}^2$. Shifting the cut to smaller values would cause the calculation to include regions where the perturbational QCD approach cannot be justified due to the energies getting small and the reliability of the parton model fading [60, p. 4, 61, p. 120], thus leading to the introduction of larger higher order QCD corrections. Instead, the missing part can be calculated separately as the $p\gamma \rightarrow WjjjX$ cross section with use of the correct electromagnetic proton structure functions (see Reference [60] for an analogous example).

In Figure 4.6, the differential NLO cross section in dependence of the natural logarithm of the virtuality normalised to the cut value, $\ln(Q^2/Q_{\min}^2)$, is shown for the process $pp \rightarrow W^+jjj$, run with the cuts and parameters listed in Section 5.1 at scales $\mu_R = \mu_F = p_{T,j1}$. For Q^2 approaching the cut value, the differential cross section converges to about 3fb. Since the proton has a finite mass, there exists a physical lower bound on the virtuality of the photon, which can be approximated to [45, p. 13, 61, p. 117, 62]

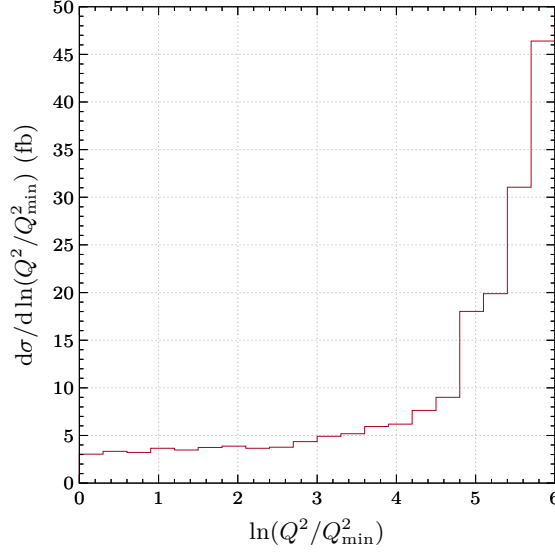


Figure 4.6: Differential cross section of W^+jjj production as a function of the virtuality of the t -channel photon.

$$Q_{\text{limit}}^2 \approx m_p^2 \frac{M^4}{s(s-M^2)} \approx m_p^2 \left(\frac{M_{Wjjj}^2}{xs} \right). \quad (4.7)$$

Here M denotes the invariant mass of the final hadron system including the $Wjjj$ system and the upper proton remnant as shown in Figure 4.7, M_{Wjjj}^2 is the invariant mass of the $Wjjj$ system only, and x is the momentum fraction of the upper proton which enters the process (so $M_{Wjjj}^2 \approx xM^2$). The invariant mass of the $Wjjj$ system at minimum contains the mass of the W boson and the invariant mass of the two tagging jets. With the information from the tagging jet invariant mass distribution presented in the next chapter, Figure 5.6, a sensible lower value of the invariant mass of the $Wjjj$ system is

$$M_{Wjjj}^2 \gtrsim 600 \text{ GeV}. \quad (4.8)$$

By using the fact that in the considered limit the photon is parallel to the proton it was emitted from, the invariant mass of the $Wjjj$ system can also be expressed as $M_{Wjjj}^2 \approx x^2 s$ [62].

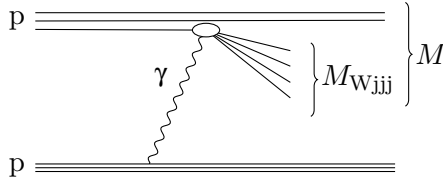


Figure 4.7: Schematic diagram for the process $pp \rightarrow WjjjX + p$.

Thus, a highly generous approximation of the lower bound on the photon virtuality for a center-of-mass energy of 14 TeV is

$$Q_{\text{limit}}^2 \approx m_{\text{p}}^2 \frac{M_{\text{Wjjj}}^2}{s} \gtrsim 1.8 \cdot 10^{-3} \text{ GeV}^2. \quad (4.9)$$

Using this bound and the asymptotic limit of the differential cross section, the total cross section lost by applying the cut may be estimated to

$$\sigma_{\text{lost}} \approx \frac{d\sigma}{d \ln \left(\frac{Q^2}{Q_{\text{min}}^2} \right)} \Big|_{Q_{\text{min}}^2} \cdot \left(\ln \left(\frac{Q_{\text{min}}^2}{Q_{\text{min}}^2} \right) - \ln \left(\frac{Q_{\text{limit}}^2}{Q_{\text{min}}^2} \right) \right) \approx 23 \text{ fb}. \quad (4.10)$$

This would give a correction of 8% to the total cross section of the process of 278.46 fb. However, this is a large overestimate of the real loss of cross section due to the cut, firstly because the invariant mass of the Wjjj system used for the calculation above is probably much underestimated, and secondly because the differential cross section does not stay constant for low Q^2 , but drops off already before reaching Q_{limit}^2 . The real lost cross section rather lies at a few per cent. This is exactly the range of the electroweak corrections to the process, which have not been treated in this work but need to be calculated separately to give a more exact result of the total cross section for Wjjj production.

CHAPTER 5

Phenomenology

With all parts of the newly implemented Wjjj cross section calculation up to NLO in QCD tested, VBFNLO can be run with a specific set of cuts and parameters to produce results, as explained in Section 3.1. Before analysing important differential cross section distributions and the scale dependence of the total cross section in the following sections, the cuts, physical parameters and *Monaco* settings used to produce these results are presented. In the last section of this chapter, the Wjjj differential cross sections and K factors are compared to the ones of the process $pp \rightarrow Hjjj$ in order to examine differences or similarities in their structure.

5.1 Cuts and Parameters

The cuts imposed on experimentally measurable quantities of the final observables can be changed in the file **cuts.dat**. The ones relevant for the considered process $pp \rightarrow Wjjj$ with leptonic decay of the W boson can be classified in jet cuts, lepton cuts, and VBF cuts. Some jet and lepton cuts resemble experimental bounds, for instance to distinguish two jets. Others, including the VBF cuts, assure for the results to not include phase space regions where the approximations made in the calculation do not hold and where other background processes, such as QCD induced processes, get significant. The several relevant cuts are listed in Table 5.1. Most of the cuts have been chosen in compliance with cuts used by the CMS and ATLAS collaborations for Wjj production via VBF, see References [63, 64]. Only events with at least three distinguishable jets are considered, which are reconstructed from final state partons using the generalised k_T algorithm [65–67] (for its application see Reference [68]). The two jets with highest transverse momentum are called tagging jets and need to be detected in opposite detector hemispheres. The common constraint that the decay lepton needs to fall inside their rapidity gap is not applied here.

As parton distributions the CTEQ6L1 PDFs [69] are used for the LO calculation and the CT10 PDFs [70] for the NLO calculation. No bottom quark contributions are considered, neither as incoming, outgoing or intermediate particles. The masses of the W and Z bosons $m_Z = 91.188 \text{ GeV}$ and $m_W = 80.398 \text{ GeV}$ along with the Fermi coupling $G_F = 1.166 \cdot 10^{-5} \text{ GeV}^{-2}$ are chosen as input parameters, from which the fine structure constant and the weak mixing angle are obtained.

Table 5.1: All relevant cuts that are applied.

Jet cuts			
Minimal R separation of two jets	R_{jj}^{\min}	=	0.4
Maximal absolute parton rapidity	$ y_p ^{\max}$	=	5
Maximal absolute jet rapidity	$ y_j ^{\max}$	=	4.5
Minimal transverse momenta of jets (sorted in p_T)	$p_{T,j}^{\min}$	=	50/30/20 GeV
Exponent of generalised k_T algorithm	P_{k_T}	=	-1
Lepton cuts (l labels the charged lepton)			
Maximal absolute lepton rapidity	$ y_l ^{\max}$	=	2.5
Minimal transverse momentum of lepton	$p_{T,l}^{\min}$	=	25 GeV
Minimal R separation of lepton and jets	R_{jl}^{\min}	=	0
Minimal missing transverse momentum	$p_{T,\text{miss}}^{\min}$	=	30 GeV
VBF cuts (applied on tagging jets)			
Minimal rapidity separation $\Delta y_{ab} = y_a - y_b $ of tag. jets	$\Delta y_{j_1 j_2}^{\min}$	=	3
Tagging jets must be in opposite det. hemispheres	$y_{j_1} \cdot y_{j_2}$	<	0
Minimum invariant mass of tagging jets	$m_{j_1 j_2}^{\min}$	=	500 GeV

The results are obtained for a center-of-mass energy of $E_{\text{cm}} = 14$ TeV. The implemented process can be calculated with incoming protons as well as antiprotons, and the decay of the W boson can be in any lepton family or summed over all three. For the presented results, the process with two initial protons and the decay of the W boson into electron/positron and respective neutrino was chosen. For the statistics to be high enough to obtain a satisfying resolution for the differential cross section distributions, the LO and virtual calculation were run over 2^{26} phase space points and the real emissions over 2^{30} phase space points, from which between 25 % to 33 % gave non-zero contributions in the last iteration. Depending on the chosen scales and with three iterations over an already improved grid, this caused runtimes of around 320 h on a single 3.2 GHz core.¹ For the analysis of scale dependences, less statistics of 2^{24} points for the LO and virtual corrections and 2^{27} points for the real emissions was used.

¹ VBFNLO supports MPI, which allows for running code in parallel. Thereby, this runtime can further be reduced largely by using multiple cores in parallel. By using the already optimised grid the same statistics can for example be reached in less than two days by doing parallel runs on four cores.

5.2 Differential Cross Section Distributions

Considering only LO, the results are expected to be highly dependent on the factorisation and renormalisation scale, as mentioned in Section 2.3.1. By including the NLO corrections, this dependence should flatten out. The detailed analysis of scale dependences follows in the next section, but by examining the differential cross section distributions of LO and NLO results at different scales, “good” scales can already be found since for these LO and NLO distributions are alike. For this reason the distributions on the following pages show the results obtained at four different scale choices $\mu_R = \mu_F = \mu$, three of them being dynamic and one being constant. The dynamic scales chosen are the transverse momenta of the three jets j_1 , j_2 , and j_3 , where the numbering of the jets here and in the following is chosen according to the magnitude of their transverse momentum. The tagging jets are the jets with highest p_T , so by definition j_1 and j_2 are always the tagging jets. The constant scale is chosen at $\mu_{\text{const}} = 100 \text{ GeV}$, and is only meant for comparison, as the chosen scale should be directly connected to the quantities where the scale enters in the calculation.

The total LO and NLO cross sections obtained for the parameters described in the preceding section are given in Table 5.2 together with their resulting K factors

$$K = \frac{\sigma_{\text{NLO}}}{\sigma_{\text{LO}}}. \quad (5.1)$$

The differences in magnitude between the processes $pp \rightarrow W^+ \text{jjj}$ and $pp \rightarrow W^- \text{jjj}$ are due to the different densities of quarks in the proton.

In Figure 5.1, the differential cross sections in dependence of the transverse momenta of jets 1, 2, and 3 are shown (that is the maximal, second largest and third largest transverse jet momenta), with the results for $W^+ \text{jjj}$ production on the left- and the ones for $W^- \text{jjj}$ on the right-hand side. The LO distributions are shown as dashed lines, while the solid lines show the NLO results. Below each distribution, the K factors for the four scales are plotted. In all three distributions, the NLO curves seem to coincide, showing only statistical deviations, except for the ones with scale $\mu = p_{T,j_3}$, which drop faster after peaking. The LO distributions on the other hand vary significantly more with the scale. This is a first sign for a high reduction in scale uncertainties and low scale dependence of the NLO calculation. The LO distributions of the scale p_{T,j_1} cannot be spotted clearly

Table 5.2: Full LO and NLO cross sections for four different scale choices $\mu_R = \mu_F = \mu$ and the parameters specified in Section 5.1.

μ	$\sigma_{\text{LO}}^{\text{W}^+}$ in fb	$\sigma_{\text{NLO}}^{\text{W}^+}$ in fb	K^{W^+}	$\sigma_{\text{LO}}^{\text{W}^-}$ in fb	$\sigma_{\text{NLO}}^{\text{W}^-}$ in fb	K^{W^-}
p_{T,j_1}	273.66 ± 0.17	278.46 ± 0.47	1.02	156.45 ± 0.13	163.62 ± 0.27	1.05
p_{T,j_2}	314.51 ± 0.19	276.14 ± 0.55	0.88	180.13 ± 0.11	162.99 ± 0.29	0.90
p_{T,j_3}	407.71 ± 0.26	241.90 ± 0.89	0.59	232.13 ± 0.15	146.01 ± 0.52	0.63
100 GeV	311.20 ± 0.20	269.41 ± 1.48	0.87	175.96 ± 0.11	160.77 ± 0.32	0.91

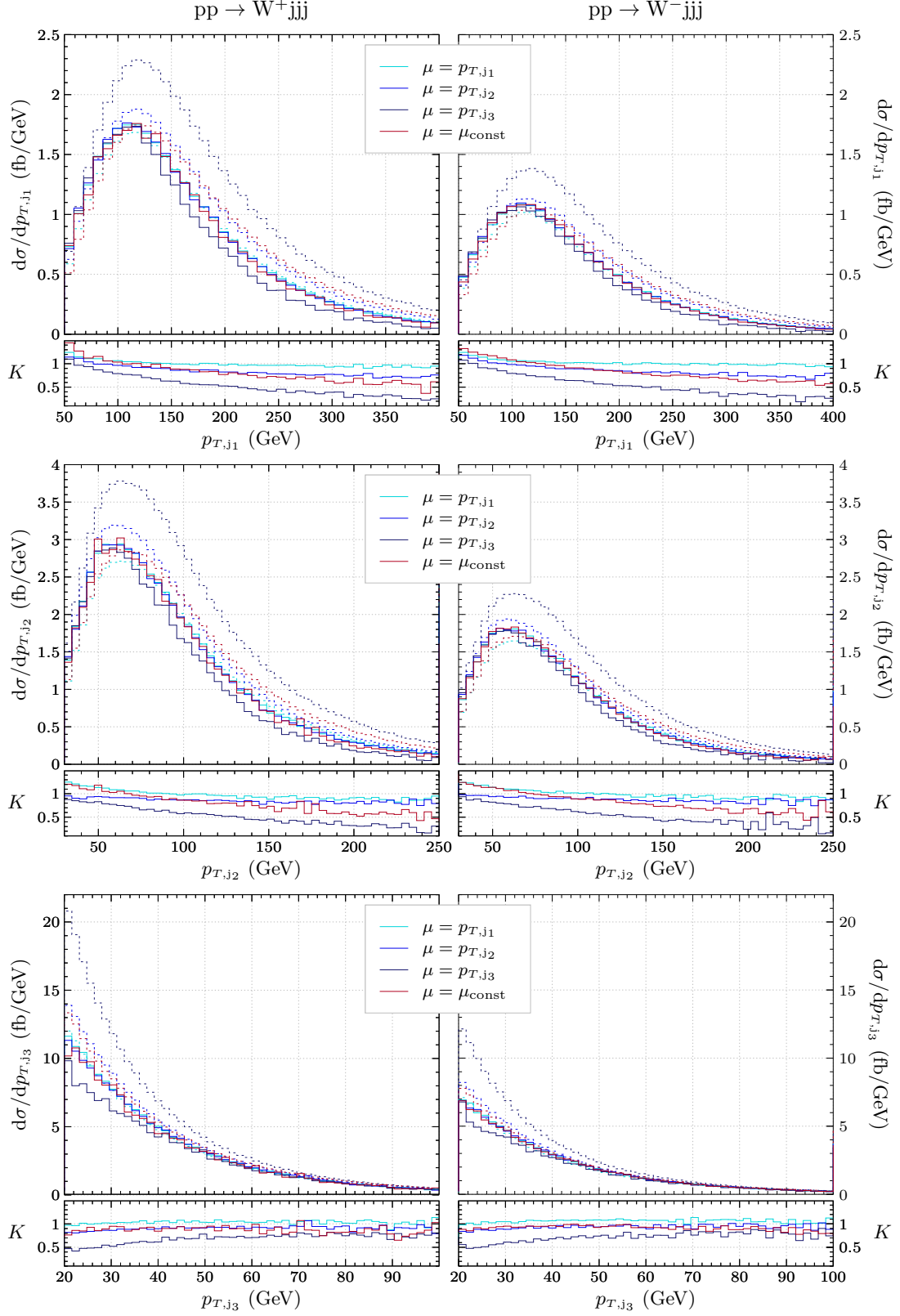


Figure 5.1: Transverse momentum distributions and respective K factors for W^+jjj (left column) and W^-jjj (right column) production, for the three jets j_1 , j_2 , and j_3 sorted in descending order according to their p_T . The dashed lines show the LO, the solid lines the NLO distributions for the four colour-distinguished scale choices $\mu_R = \mu_F = \mu$ shown in the legend (with $\mu_{\text{const}} = 100$ GeV).

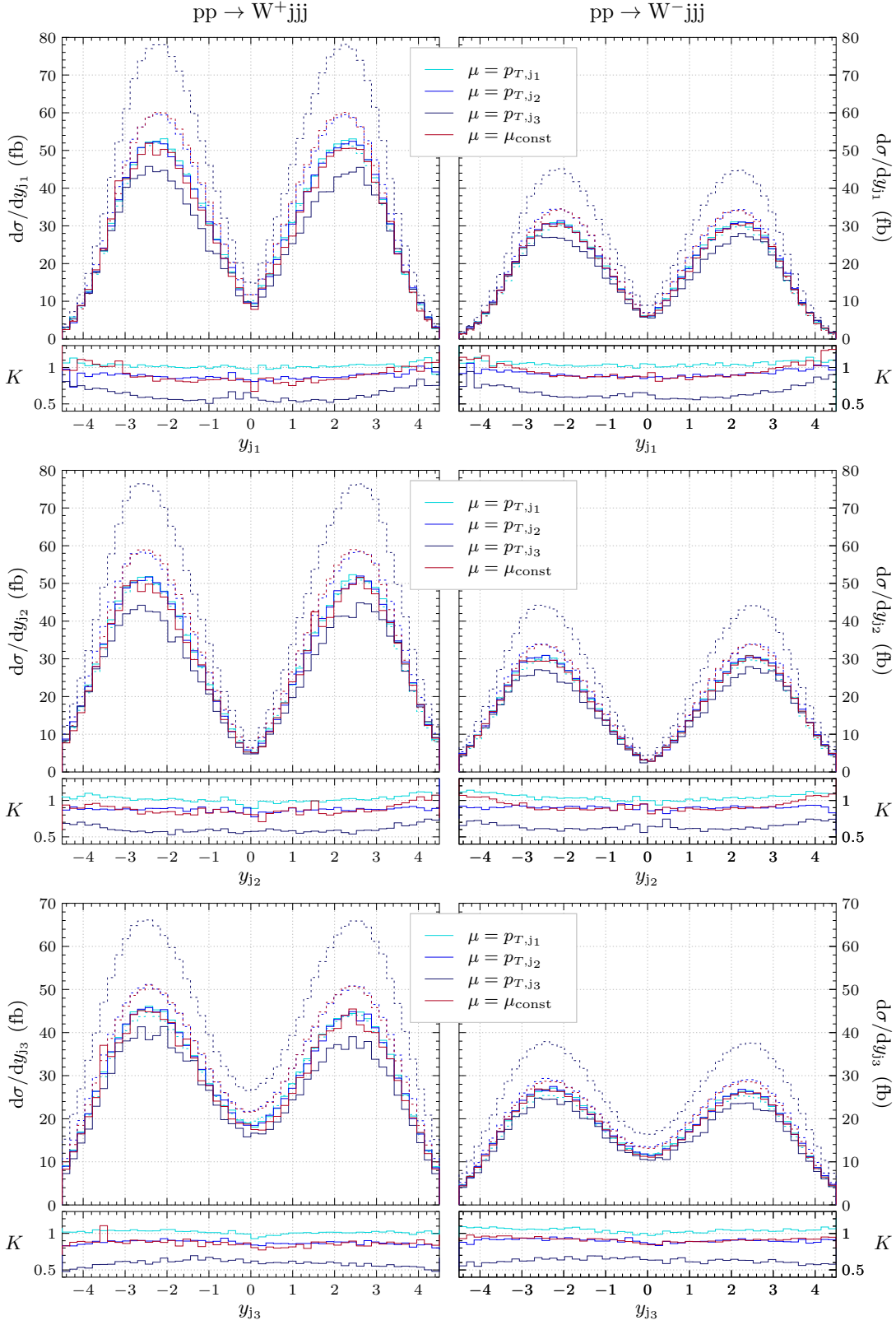


Figure 5.2: Rapidity distributions and respective K factors for $W^+ j j j$ (left column) and $W^- j j j$ (right column) production, for the three jets j_1 , j_2 , and j_3 sorted in descending order according to their p_T . The dashed lines show the LO, the solid lines the NLO distributions for the four colour-distinguished scale choices $\mu_R = \mu_F = \mu$ shown in the legend (with $\mu_{\text{const}} = 100$ GeV).

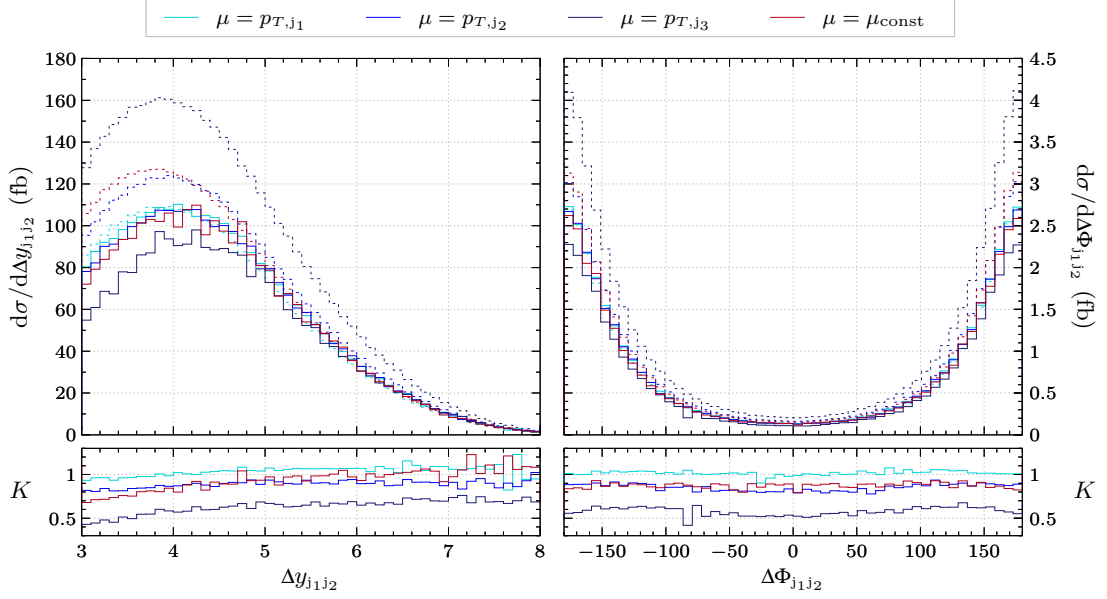


Figure 5.3: Distributions in dependence of the rapidity separation (left) and angular separation (right) between the two tagging jets for W^+jjj production. The dashed lines show the LO, the solid lines the NLO distributions for the four colour-distinguished scale choices $\mu_R = \mu_F = \mu$ shown in the legend (with $\mu_{\text{const}} = 100 \text{ GeV}$).

because of it being very similar to the respective NLO curves. This behaviour enters also in the K factors of this scale wavering around one. The maximum transverse jet momentum thus seems to be a good scale choice for these processes, at least with respect to the p_T -distributions, while $\mu = p_{T,j3}$ is much too small a scale to use.

The rapidity distributions in Figure 5.2 show the same behaviour regarding the scales, leading to the same conclusion. All K factors here are almost flat, in contrast to the transverse momentum distributions above. It is rather interesting that the constant scale choice seems to also produce very accurate results. The rapidity distributions also show the typical VBF behaviour, with the two tagging jets appearing in the forward directions of the detector, and a reduced jet activity in the central region. In the distribution of the third jet's rapidity, this dip in the central region gets less distinct.

Since a cut forces the two tagging jets to appear in different detector hemispheres, their rapidity distributions already show that the two jets are widely rapidity separated. This behaviour can be seen more directly by considering the rapidity separation of the two tagging jets,

$$\Delta y_{j1j2} = |y_{j1} - y_{j2}|, \quad (5.2)$$

which is shown on the left of Figure 5.3 for W^+jjj production (as can be seen in the preceding distributions, W^-jjj production shows analogous results). The Δy_{j1j2} distribution begins at three because of the cut that was applied, see Section 5.1. After peaking at a

maximum cross section at a rapidity separation of around four, the curves slowly decrease. In the histogram on the right-hand side of the same figure, the distribution of the angular separation of the two tagging jets, $\Delta\Phi_{j_1j_2}$, is shown. It is defined by subtracting the angle of the jet with smaller rapidity from the one with higher rapidity, meaning it is ordered in the direction of the detector. Also with respect to this coordinate the tagging jets appear in opposite directions. While the K factors of all scales are stable with respect to the angular separation, they are highly dependent on the phase space region with regard to the rapidity separation of the tagging jets. In addition, the peak in the latter distribution moves to higher rapidity separations $\Delta y_{j_1j_2}$ for the NLO corrections of all four scale choices.

To analyse the position of the third jet relative to the tagging jets, it is convenient to consider the normalised relative rapidity difference of the third jet to the tagging jets,

$$z_{j_3}^* = \frac{y_{j_3} - \frac{y_{j_1} + y_{j_2}}{2}}{\frac{1}{2}\Delta y_{j_1j_2}} = \frac{2y_{j_3} - (y_{j_1} + y_{j_2})}{\Delta y_{j_1j_2}}, \quad (5.3)$$

which is zero if the third jet's rapidity lies exactly in between the two tagging jets' ones, and one or minus one if it coincides with the rapidity of one of the tagging jets.

In the top left histogram of Figure 5.4 the distribution of $z_{j_3}^*$ is shown, this time only for W^+jjj production at the scale $\mu = p_{T,j_1}$. The LO distribution is again marked as dashed line, the NLO one as solid line. Apparently, the third jet mostly appears in the vicinity of one of the tagging jets, with regard to rapidity. The slight bumps at $z_{j_3}^* = \pm 1$ arise due to the minimum R separation of two jets to be able to distinguish them in the detector. In the bottom histograms of the same Figure the distributions of relative angular separations of the third jet to jets 1 ($\Delta\Phi_{j_3j_1}$) and 2 ($\Delta\Phi_{j_3j_2}$) are shown, in which the above mentioned bumps also appear. These in addition show that the third jet also with respect to the angle appears primarily in the vicinity of one of the tagging jets, as the differential cross section is large either if the third jet is at the position of the respective tagging jet, or in the opposite Φ direction, where the other tagging jet is most likely to be located, as follows from the $\Delta\Phi_{j_1j_2}$ distribution in combination with the rapidity and relative rapidity distributions. The increase of the cross section for the third jet being in the vicinity of a tagging jet in respect to both angle and rapidity can directly be seen in the top right histogram of Figure 5.4 showing the minimum R separation between the third jet and one of the tagging jets. To be precise, jet 3 is to appear most likely in the vicinity of the jet with second highest p_T , which gets clear when comparing the $\Delta\Phi_{j_3j_1}$ and $\Delta\Phi_{j_3j_2}$ distributions.

To further analyse the position of the produced W boson (or rather the charged decay lepton, since the neutrino cannot be detected experimentally except for its missing momentum), Figure 5.5 shows the normalised relative rapidity difference of the lepton with respect to the two tagging jets,

$$z_l^* = \frac{2y_l - (y_{j_1} + y_{j_2})}{\Delta y_{j_1j_2}}. \quad (5.4)$$

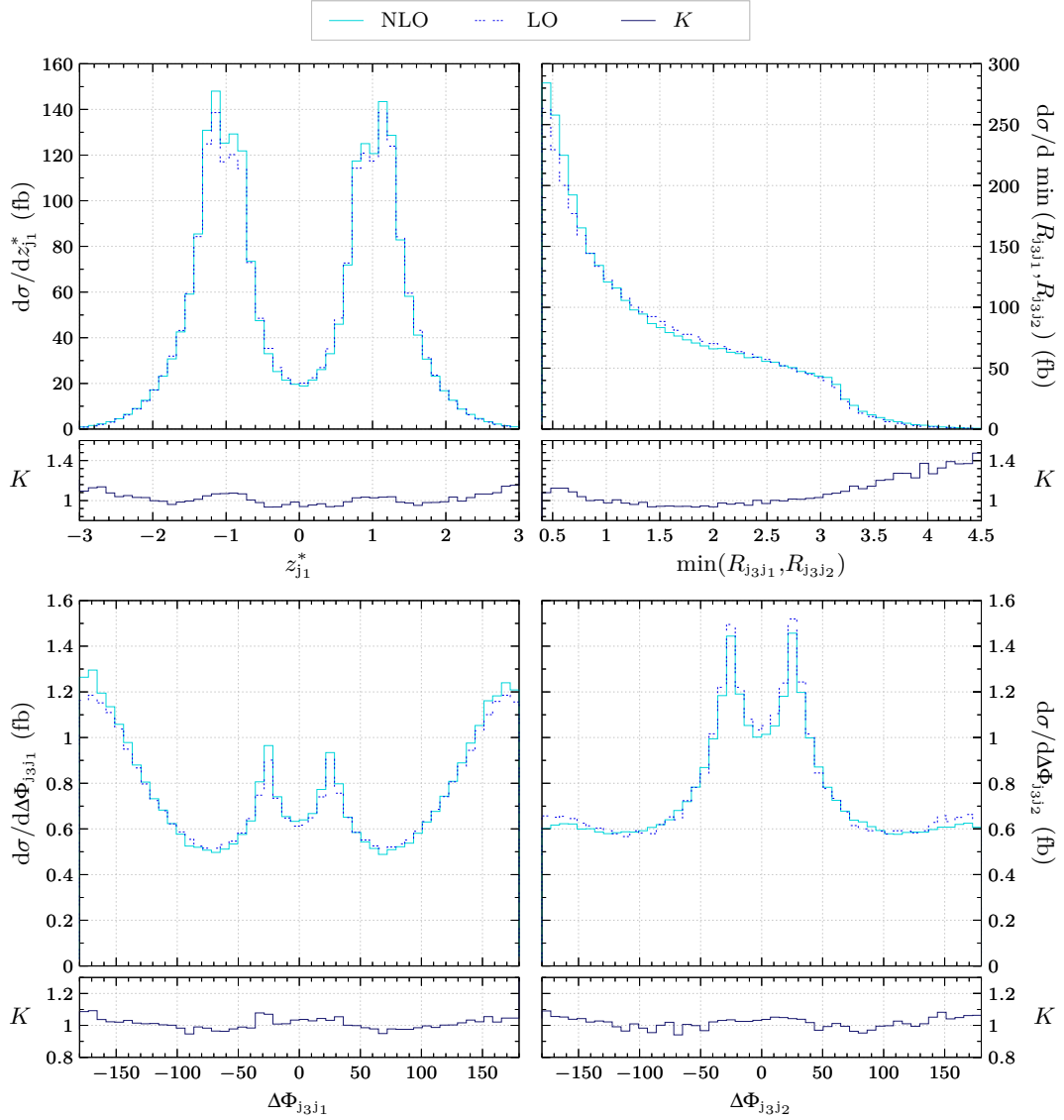


Figure 5.4: Differential cross section distributions indicating the relative position of the third jet to the tagging jets. On the upper left, the normalised relative rapidity difference z_{j3}^* is shown, on the upper right the minimum R separation between the third and one of the tagging jets. The lower plots show distributions of the angular separation between the third jet and first (left) or second (right) tagging jet (as always numbering ordered according to p_T). All distributions are obtained for W^+jjj production at the scale $\mu_R = \mu_F = p_{T,j1}$.

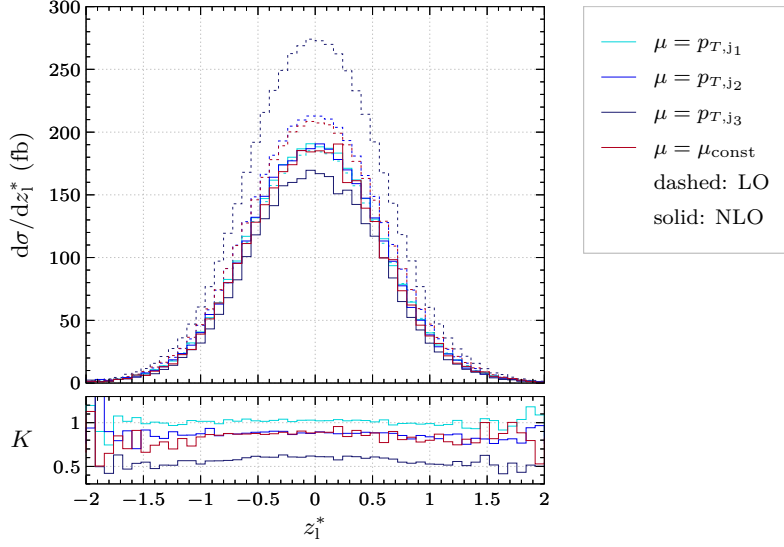


Figure 5.5: Differential cross section distributions of the normalised relative rapidity difference of the charged lepton with respect to the two tagging jets for $W^+ j j j$ production. Like in the previous figures, the dashed curves show the LO, the solid ones the NLO distributions, and the four used scales are distinguished by colour.

The largest part of the cross section is found between $z_1^* = -1$ and $z_1^* = 1$, meaning in most cases the lepton appears in between the tagging jets with respect to rapidity.

Finally, the left graph of Figure 5.6 shows the differential cross section in dependence of the invariant mass of the two tagging jets,

$$m_{j_1 j_2} = \sqrt{(p_{j_1} + p_{j_2})^2}. \quad (5.5)$$

The cutoff at 500 GeV cuts a large part of the cross section for this process, but it is necessary for removing possible overlying signals such as QCD induced background processes. The differential cross section reaches a maximum at an invariant mass of about 600 GeV before declining. The LO and NLO distributions again show striking differences in their shapes which manifests as a change in the K factor for all considered scales over the range of $m_{j_1 j_2}$. Such a phase space dependence of the K factor is also strongly visible in the p_T and $\Delta y_{j_1 j_2}$ distributions, while the K factors of the $\Delta\Phi$ and rapidity distributions are rather flat. In the $m_{j_1 j_2}$ distribution it is also noticeable that the phase space dependence of the K factor is larger for the scale $\mu = p_{T,j_3}$ than for the other scales, especially $\mu = p_{T,j_1}$. The right graph of Figure 5.6 shows the ratios between $m_{j_1 j_2}$ distributions obtained for scale choice $\mu = p_{T,j_1}$ to distributions obtained for $\mu = p_{T,j_2}$ (blue) and to those obtained for $\mu = \mu_{\text{const}}$ (red). By considering the difference in the LO and NLO ratios it gets evident that this phase space dependence results primarily from the different shapes of the LO distributions, while the NLO distributions behave fairly similar. Striking is further that the LO (to a smaller extent also the NLO) ratio between dynamic and constant scale varies much more

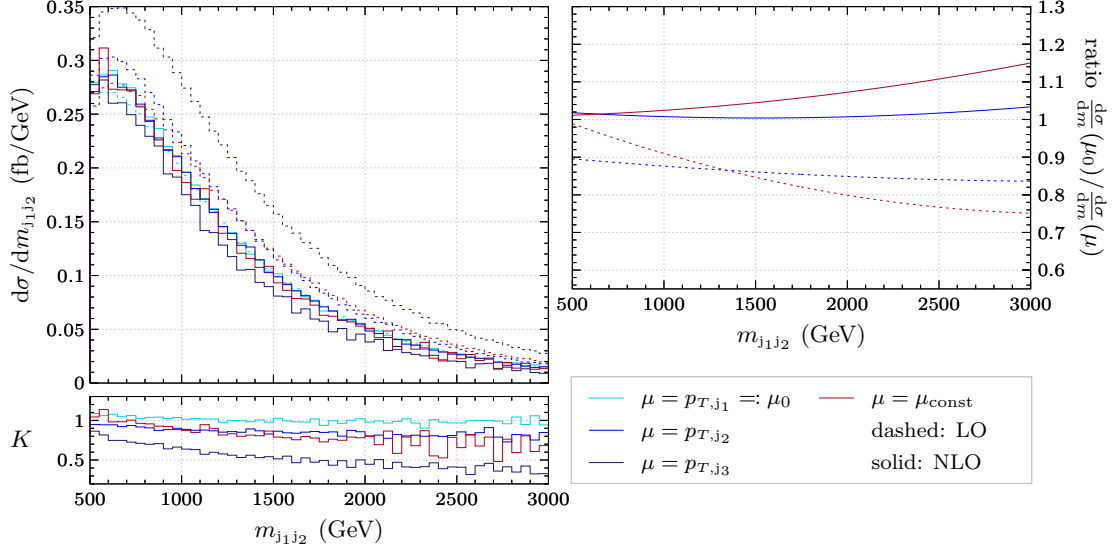


Figure 5.6: Distribution of the differential cross section in dependence of the invariant mass of the two tagging jets, $m_{j_1 j_2}$, for $W^+ j j j$ production. The dashed lines show the LO, the solid lines the NLO distributions for the four colour-distinguished scale choices $\mu_R = \mu_F = \mu$ shown in the legend (with $\mu_{\text{const}} = 100$ GeV). The right graph shows the ratio between the differential cross sections of scales $\mu = p_{T,j_1}$ and $\mu = p_{T,j_2}$ in blue and between $\mu = p_{T,j_1}$ and $\mu = \mu_{\text{const}} = 100$ GeV in red.

over phase space than the ratio between the two dynamic scales.

In conclusion, it is not recommendable to multiply LO distributions by known K factors in order to obtain the corresponding NLO distributions for $W j j j$ production, since the K factors are highly phase space dependent. The degree of this dependence further changes with different scales. The scale which shows the least phase space dependences and can, following the analysis so far, be considered as the best one of the chosen scales to describe $W j j j$ production is $\mu = p_{T,j_1}$. However, there are phase space regions where other scales lead to a better agreement of LO and NLO result.

5.3 Scale Variations

Renormalisation and factorisation scales are unphysical quantities, introduced to control ultraviolet and infrared singularities, that cancel if the full cross section including all higher order corrections would be calculated. However, this is not possible, so by calculating the NLO corrections to a process the aim is to at least reduce the scale dependences of the LO calculation by some amount. The more precise the NLO calculation is, the more the scale dependences should flatten out. This implies that the more scale dependent the NLO cross section still is, the more uncertain is the calculation up to this order.

The investigation of differential cross section distributions in the preceding section already

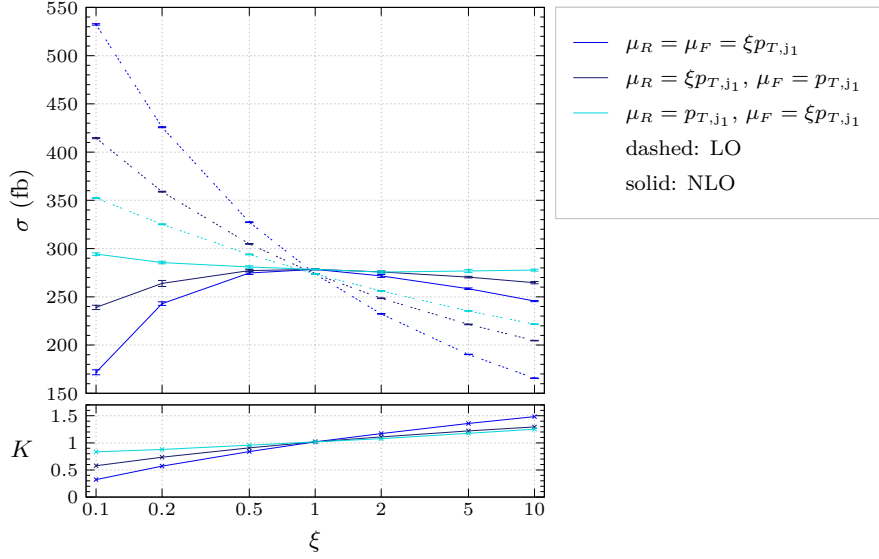


Figure 5.7: Total cross section and K factor for W^+jjj production in dependence of different variations of renormalisation and factorisation scale around $\mu = p_{T,j_1}$.

indicated a strong reduction of scale uncertainties, since the NLO distributions are strongly compatible. Solely the distributions for the lowest scale $\mu = p_{T,j_3}$ show some discrepancies in comparison to the other three. For a more precise analysis, the total cross section is examined at scales $\xi\mu$, with $\xi \in [1/10, 10]$ for $\mu \in \{p_{T,j_1}, p_{T,j_2}, \mu_{\text{const}}\}$ and $\xi \in [1/5, 20]$ for the smaller scale $\mu = p_{T,j_3}$. In Figure 5.7 the cross section for W^+jjj production is shown for variations of renormalisation scale (dark blue), factorisation scale (turquoise) and simultaneous variation of both scales (medium blue) around the scale $\mu = p_{T,j_1}$. The scale uncertainties introduced by variation of the renormalisation scale are much larger than the ones caused by varying the factorisation scale. In both cases, the inclusion of the NLO corrections compensates most of the LO scale dependences by adding to the cross section for large scales (leading to a K factor larger than one) and subtracting in the region of low scales (giving a K factor smaller than one). The NLO cross section itself is very stable for large scales, differing only by maximal 12% at $\xi = 10$ with respect to its value at $\xi = 1$, while the LO cross section for $\xi = 10$ differs up to about 40%. For low scales, where the LO cross section exceeds its central value of about 95% when varying both scales, the NLO cross section drops to 62% of its maximal value.

The variations around the scales $\mu \in \{p_{T,j_2}, p_{T,j_3}, \mu_{\text{const}}\}$, shown in Figure 5.8, lead to similar behaviours of the NLO cross section. For high scales it stabilises while it drops rapidly for low scales that are too small to describe this process correctly. The curves of $\mu = p_{T,j_2}$ and $\mu = \mu_{\text{const}}$ look almost identical for both LO and NLO, in addition to their differential cross section distributions also being similar. For the smallest scale $\mu = p_{T,j_3}$, the LO cross section exceeds 700 fb already for $\xi = 0.2$, where the NLO cross section gets negative. The variation of the NLO cross section for $0.5 \leq \xi \leq 2$ is larger than 30%. Thus,

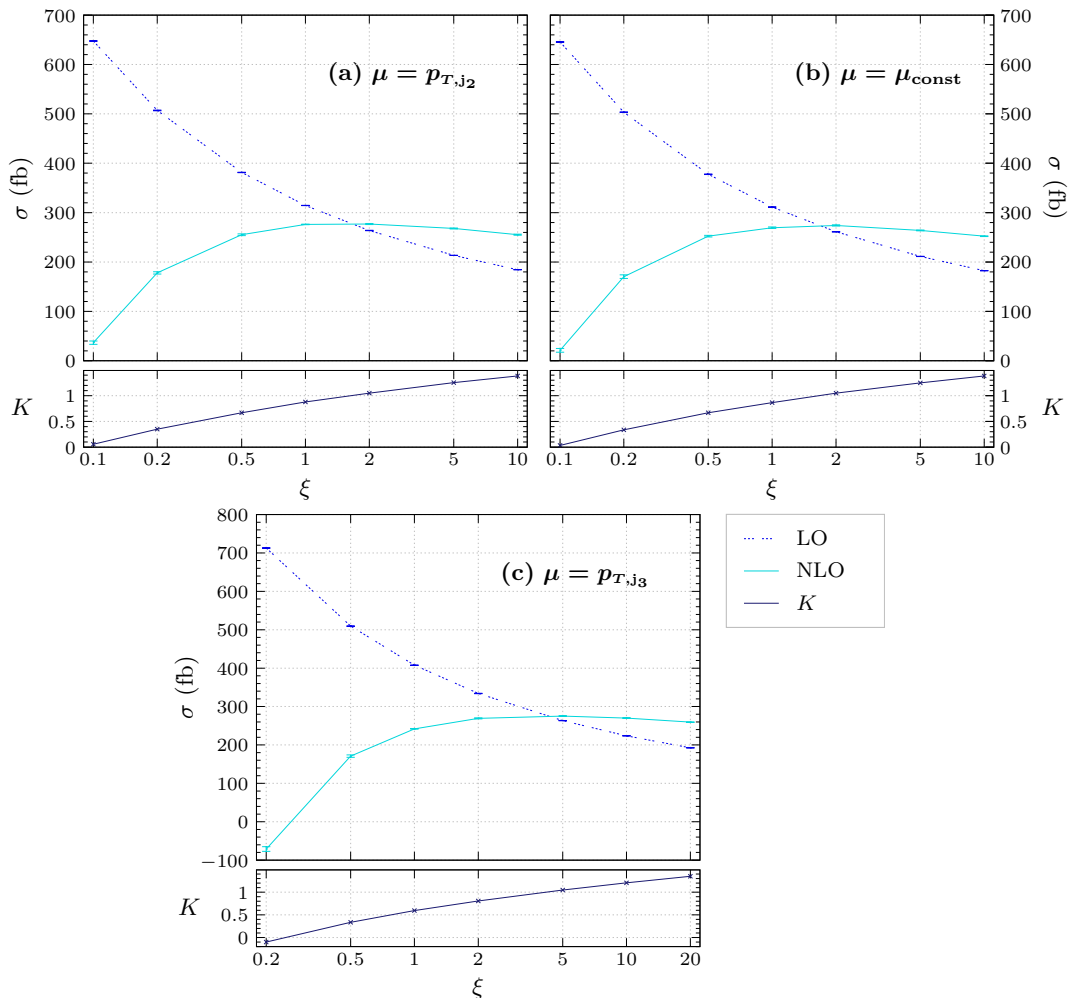


Figure 5.8: Total cross section and K factor for W^+jjj production in dependence of simultaneous variation of renormalisation and factorisation scale, $\mu_R = \mu_F = \xi\mu$, around $\mu = p_{T,j_2}$ (a), $\mu = \mu_{\text{const}} = 100$ GeV (b), and $\mu = p_{T,j_3}$ (c). (It has to be taken note of the different ranges of ξ and σ in the three graphs.)

it is obvious that this is no good scale choice for the considered process. Rather is $\mu = p_{T,j_1}$, where the variation in the same range is below 3%. This is due to the maximum of the NLO curve, marking the region with least scale uncertainties, being close to $\xi = 1$. The intersection between LO and NLO curves also coincides roughly with $\xi = 1$ for $\mu = p_{T,j_1}$, which also became apparent in the good accordance between LO and NLO differential distributions.

The similar K factor distributions in Figures 5.1 and 5.2 roughly indicate that there are no significant differences between $pp \rightarrow W^+jjj$ and $pp \rightarrow W^-jjj$ regarding the relative change between LO and NLO cross sections with respect to different scale choices and different phase space regions. To demonstrate this behaviour more precisely, the K factors

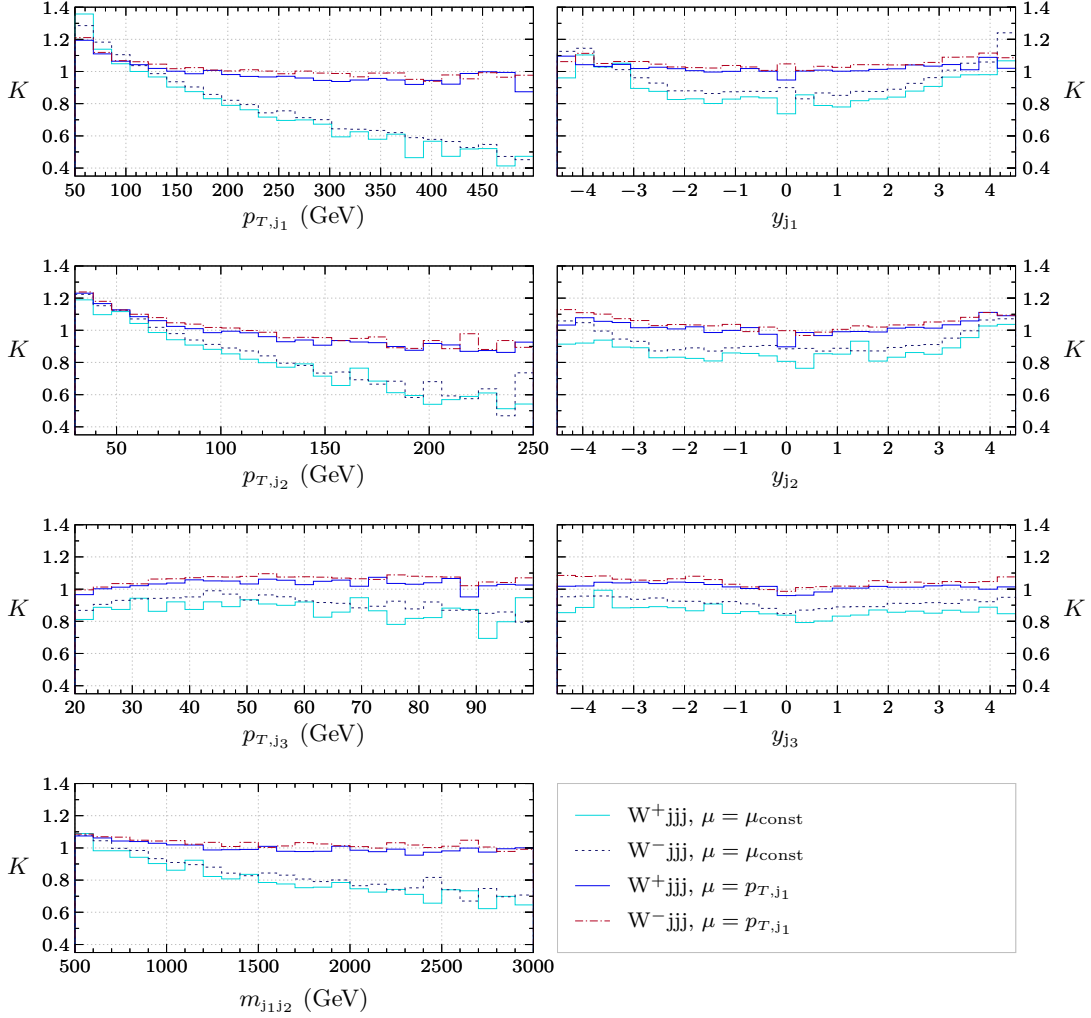


Figure 5.9: K factors for W^+jjj production in comparison to those for W^-jjj production for one dynamic scale, $\mu_R = \mu_F = p_{T,j_1}$, and one constant scale, $\mu_R = \mu_F = \mu_{\text{const}} = 100$ GeV, in dependence of the transverse momenta of the three highest p_T jets, their rapidities and the invariant mass of the tagging jets.

of W^+jjj (solid lines) and W^-jjj (dashed lines) production for one dynamic scale (p_{T,j_1}) and one constant scale (μ_{const}) in dependence of some selected kinematic variables are shown side by side in Figure 5.9. There, the analogy between the two processes distinctly manifests. As a consequence, it can rightly be assumed that the total cross sections of the two processes behave analogously under shifts in the renormalisation and factorisation scale, and therefore all results obtained above generalise to $pp \rightarrow W^-jjj$.

5.4 Comparison to H Production via VBF in Association with Three Jets

Beyond the Standard Model physics is thought to appear most likely in the Higgs sector. It is thus important to understand the structure of Higgs boson production to search for discrepancies to the Standard Model. Both W and Higgs production in association with three jets via VBF share the same QCD topology regarding their Feynman diagrams. In this section, the QCD predictions of these two processes are compared in order to gain a better understanding of their QCD structure. This might for example also be useful in the context of central jet veto, which is used to reduce the QCD induced background to electroweak Higgs or weak boson production. In contrast to their QCD topology, the electroweak topologies of Higgs and W boson production in association with three jets differ. As the Higgs' coupling to light quarks is negligible and top along with bottom quarks are not considered for this analysis, the Higgs boson can only be produced via leptonic tensor graphs. The W boson on the other hand can be emitted from the external quark legs as well. This may lead to differences in their differential cross section distributions.

The following results were obtained with the implementation of Hjjj production via VBF in VBFNLO, see References [50, 51]. The same cuts as listed in Table 5.1 have been used, except for the cuts on the decay products of the W boson, meaning the lepton and missing transverse momentum cuts. The results were obtained for on-shell Higgs production, so to obtain a comparable result to the Wjjj results with the mentioned lepton cuts, a transverse momentum cut on the produced Higgs boson of $p_{T,H} \geq 55$ GeV was used.

Figure 5.10 shows normalised transverse momentum and rapidity distributions for both W^+jjj (turquoise) and Hjjj (dark blue) production at next-to-leading order along with their respective K factor distributions for the dynamic scale $\mu_R = \mu_F = p_{T,j_1}$. For this scale choice, the K factors of W and H production in association with three jets do not coincide, and even show a slightly different phase space behaviour in the p_{T,j_1} and y_{j_3} distributions. This behaviour is however not surprising when considering the shapes of the transverse momentum distributions. For Hjjj production, the first tagging jet more probably appears with a lower transverse momentum than for Wjjj production. This behaviour is caused by the fact that the production of a Higgs boson via VBF is favoured for two incoming longitudinally polarised weak bosons, while for the production of a W boson the fusion of transverse polarised weak bosons plays a more important role, which leads to a harder jet p_T distribution for Wjjj production [71]. Consequently, a dynamic scale proportional to the transverse momentum of one of the jets is not a good choice to compare these processes.

A better choice for this aim is the constant scale $\mu_R = \mu_F = 100$ GeV, which lies in between the W boson and the Higgs boson masses. The results are presented in Figure 5.11, with the distributions for Wjjj production again marked in turquoise and those for Hjjj production marked in dark blue. Apparently, the flat K factor distributions, such as the rapidity ones, coincide for Hjjj and Wjjj production within statistical fluctuations. At first glance the K factor distributions over the transverse momenta of the two tagging jets, p_{T,j_1} and p_{T,j_2} , seem to differ. The shapes of the K factor distributions are however similar, being only

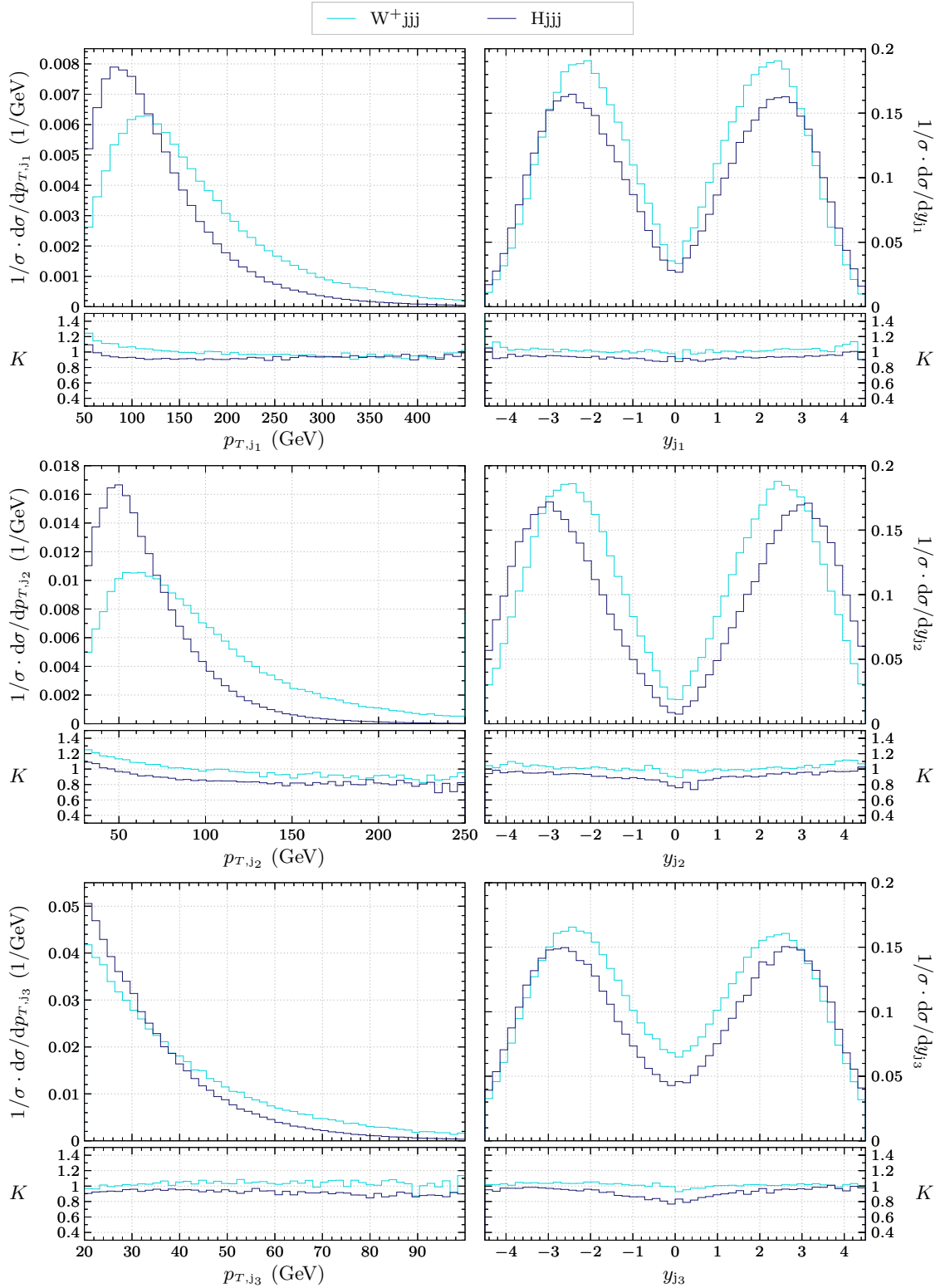


Figure 5.10: K factors and normalised differential NLO cross section distributions for W^+jjj production (turquoise) in comparison to those for $Hjjj$ production (dark blue) for the dynamic scale $\mu_R = \mu_F = p_{T,j_1}$. The transverse momentum distributions are shown on the left-hand side, the right-hand side shows the rapidity distributions.

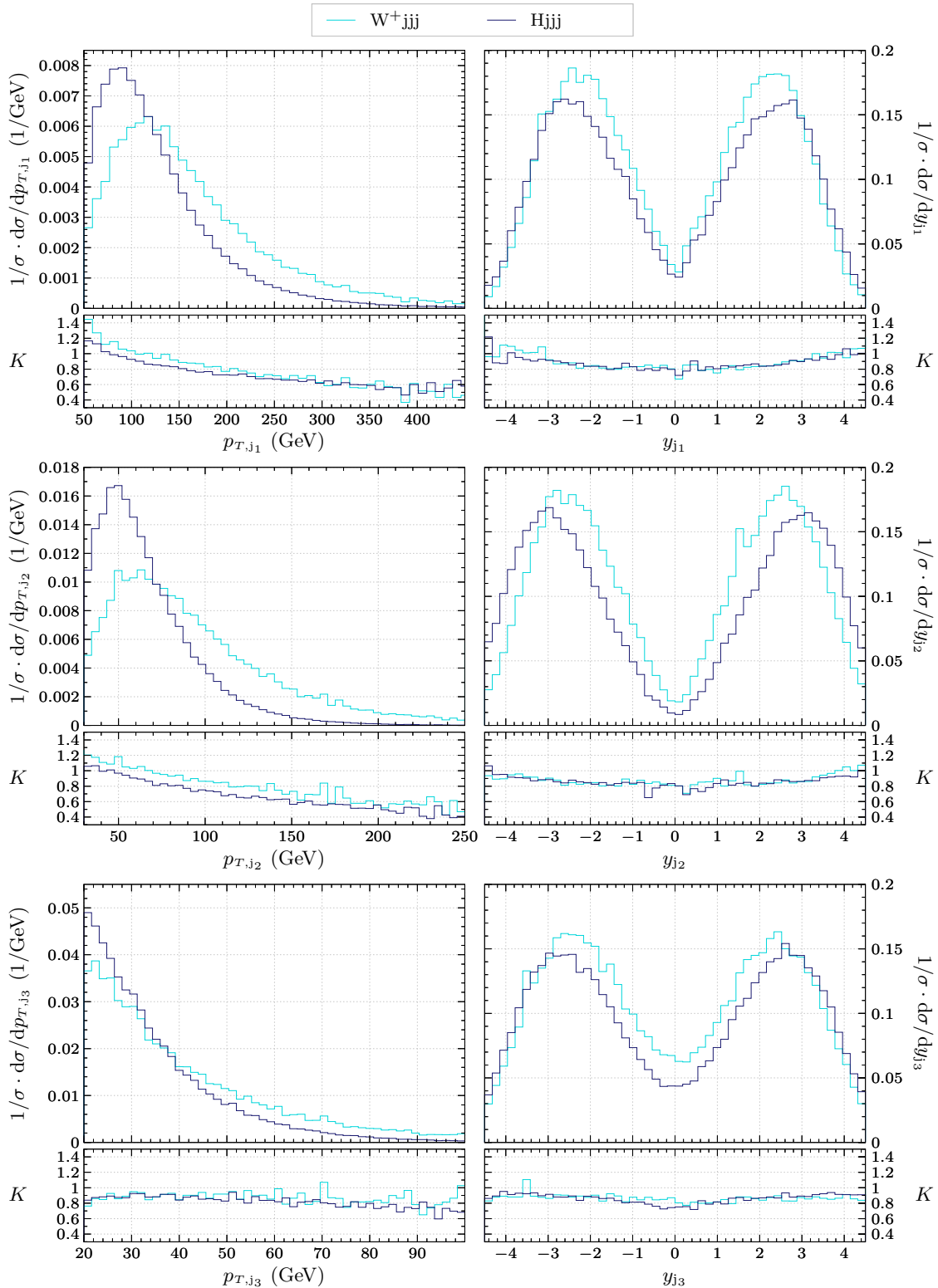


Figure 5.11: K factors and normalised differential NLO cross section distributions for $W^+ jjj$ production (turquoise) in comparison to those for $Hjjj$ production (dark blue) for the constant scale $\mu_R = \mu_F = 100$ GeV. The left-hand side shows the transverse momentum distributions, the right-hand side shows the rapidity distributions.

shifted along the p_T -axis due to the higher transverse momenta of the tagging jets for W_{jjj} production.

Noteworthy is also the differential cross section distribution with respect to the angular separation between the two tagging jets, shown in Figure 5.12. While the two tagging jets for W_{jjj} production are most probably to be found in opposite Φ directions, the differential cross section for H_{jjj} production drops to a second minimum for $\Delta\Phi_{j_1j_2} = \pi$. This behaviour can be explained by the transverse momentum cut on the Higgs boson that has been imposed. For comparison, Figure 5.13 again shows the normalised differential cross section distribution with respect to the angular separation between the two tagging jets for H_{jjj} production, but for the results shown in turquoise no cut on the transverse momentum of the Higgs boson was imposed. There is no longer a minimum for $\Delta\Phi_{j_1j_2} = \pi$ in the H_{jjj} distribution, but the maximum in this region is still significantly less pronounced than the one for W_{jjj} production, which can again be explained by the different production preferences of W and Higgs boson via VBF regarding longitudinal or transverse polarisation of the incoming weak bosons. In contrast to the differential cross section, the shape of the K factor distribution for H_{jjj} production is solely influenced up to a maximum of 5% by the cut on its transverse momentum. This was also checked for the transverse momentum and rapidity distributions, so the results concerning the similar QCD structure of W_{jjj} and H_{jjj} production obtained from Figure 5.11 are not dependent on this cut.

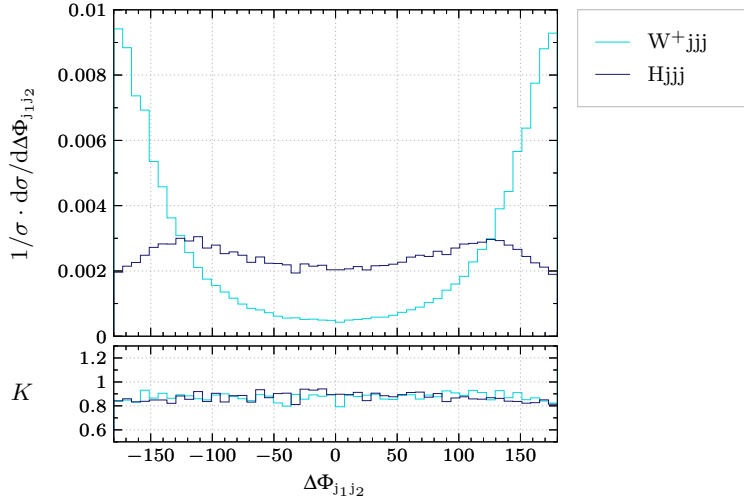


Figure 5.12: Normalised NLO and K factor distributions over the angular separation between the two tagging jets for W^+_{jjj} production (turquoise) in comparison to those for H_{jjj} production (dark blue) with transverse momentum cut on the Higgs boson of $p_{T,H} \geq 55$ GeV. The scales are chosen at the constant value $\mu_R = \mu_F = 100$ GeV.

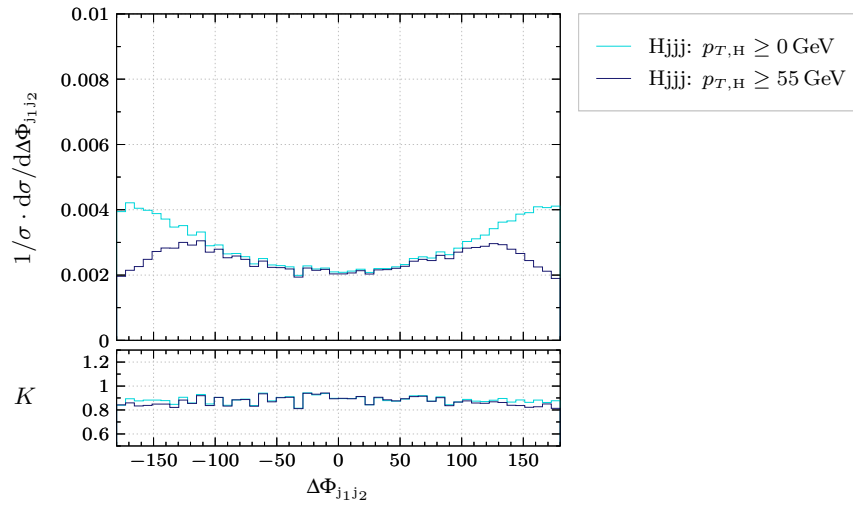


Figure 5.13: Normalised NLO and K factor distributions over the angular separation between the two tagging jets for Hjjj production with $p_{T,H} \geq 55$ GeV (dark blue) in comparison to those for Hjjj production with no transverse momentum cut on the Higgs boson (turquoise). The scales are chosen at the constant value $\mu_R = \mu_F = 100$ GeV.

CHAPTER 6

Summary

In order to find new physics and probe the limits of the Standard Model, precise predictions of Standard Model signals as well as possible backgrounds are required. Vector boson fusion and scattering processes are especially sensitive to test the electroweak sector of the Standard Model due to triple and quartic gauge boson couplings. In addition, they are an important background to searches beyond the Standard Model. The LHC [16] is the instrument of choice for acquiring the needed experimental data for comparison, performing proton-proton collisions at high center-of-mass energies. The proven approach to compute hadronic cross sections is perturbative QCD, which necessitates the calculation of higher order corrections in addition to the LO in order to obtain precise, less scale-dependent results.

This thesis presented the calculation and discussed the phenomenology of $Wjjj$ production via VBF at NLO in QCD, which was implemented in the fully flexible Monte Carlo program VBFNLO [18–21] enabling the computation of cross sections and distributions both for proton-proton and antiproton-antiproton collisions. The calculation was simplified by the use of VBF approximations and by neglecting CKM mixing. The leptonic decay of the W boson is included, which is why all resonant and non-resonant matrix elements are considered. The production of the W observable can then be described either by a leptonic tensor or an effective polarisation vector. Matrix elements are computed by combining different building blocks, such as fermion line currents and leptonic tensors, that reappear in various matrix elements. By precalculating such building blocks only once per phase space point a fast computation could be achieved.

The real emission contribution is still a very time consuming part of the calculation, because several new topologies arise due to the possibility of either two gluons taking part in the process or six external quarks, the latter leading to additional Pauli interference graphs. The virtual corrections contain loop diagrams up to pentagon level, with abelian and non-abelian contributions, which could be computed with the help of loop routines already implemented in VBFNLO for double vector boson production in association with two jets [52]. Since the real emission contributions and the virtual corrections are handled and integrated separately in the Monte Carlo program, the infrared divergences were cancelled using the dipole subtraction algorithm proposed by Catani and Seymour [44]. This procedure included the subtraction of process-specific terms in the real emission

amplitude and the addition of an insertion operator to the virtual corrections. As a final contribution, the finite collinear remainder arising from the absorption of further collinear initial splittings into the PDFs was added to the cross section.

All newly implemented parts of the calculation were thoroughly verified. LO and real emission matrix elements were crosschecked with MADGRAPH [58], virtual correction matrix elements with an already existing implementation of Zjjj production by adjusting the electroweak coupling parameters. The integrated LO cross section was compared to already validated results. Furthermore, the cancellation of infrared and collinear singularities in the real emissions due to the dipole subtraction terms was checked.

The presented results were produced for proton-proton collisions as done at the LHC, with VBF specific cuts to exclude phase space regions where other backgrounds would dominate the signal. The cross section for $pp \rightarrow W^+ jjj$ is significantly larger than for $pp \rightarrow W^- jjj$ due to the structure of the proton, being 278.5 fb for a dynamic renormalisation and factorisation scale chosen as the maximum transverse momentum of the outgoing jets. This scale emerged as the best scale choice for these processes, with its LO and NLO differential cross section distributions being similar and with a total K factor of 1.05. Other inspected scale choices were the second and third largest transverse momenta of the jets and one constant scale at 100 GeV, which produced less matching LO and NLO results. The K factor distributions show a strong phase space dependence for all analysed scale choices, meaning LO distributions cannot be multiplied with the total K factor to obtain the according NLO distributions. The largest dependences herefore are observed in the transverse momentum and tagging jet invariant mass distributions, while the rapidity K factor distributions are rather flat.

A more detailed analysis of the behaviour of the LO and NLO cross sections with varying scales demonstrated a considerable reduction of scale dependences by including the NLO contributions. By increasing and lowering the scale by a factor of two around the maximal transverse jet momentum, $\mu_F = \mu_R = \xi p_{T,j_1}$ with $0.5 \leq \xi \leq 2$, the LO cross section deviates up to 20% from its central value, whereas the variation of the NLO cross section does not exceed 3%. It was found that the NLO cross section drops considerably for particularly low scales, but stabilises at high scales, whereas the LO cross section does not stabilise at all. This stresses the importance of the inclusion of NLO corrections for eliminating higher order effects appearing in the LO cross section. Furthermore it demonstrates that with the NLO corrections at hand still a reasonable scale has to be chosen to obtain an accurate estimate of the full cross section. For $pp \rightarrow W^+ jjj$ this choice was found to be the highest transverse jet momentum.

The distributions of W production in association with three jets were further compared to distributions for H production via VBF in association with three jets [50, 51]. The processes share the same QCD topology, with a differing electroweak structure due to different production mechanisms of W and Higgs boson. It appeared that the two processes have similar K factor distributions if considering a constant scale choice in between the two boson masses. The differential cross section with respect to the angular separation

between the two tagging jets evinced dissimilar shapes in their distributions, which could be useful to distinguish weak and Higgs boson production signals.

In conclusion, the work at hand provides relevant results for future analyses of LHC data, attempting to pave the way for the discovery of new physics. The implementation is easily extendable to double W boson production in association with three jets, which is even more sensitive to new physics influencing the electroweak sector due to its quartic gauge boson couplings.

A Selected Feynman Rules of the Standard Model

A.1 Electroweak Sector

With the elementary charge $e := g'c_w$, the charge $Q = T^3 + Y/2$, and the covariant derivative with respect to the new fields,

$$D_\mu^L = \partial_\mu + i\frac{g}{\sqrt{2}} \left(W_\mu^- \frac{\sigma^-}{2} + W_\mu^+ \frac{\sigma^+}{2} \right) - i\frac{g}{c_w} Z_\mu (T^3 - s_w^2 Q) - ieA_\mu Q, \quad (\text{A.1})$$

$$D_\mu^R = \partial_\mu - i\frac{g}{c_w} Z_\mu (T^3 - s_w^2 Q) - ieA_\mu Q, \quad (\text{A.2})$$

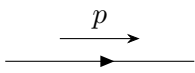
where $\sigma^\pm = \sigma^1 \pm i\sigma^2$, and mass terms for fermions resulting from Yukawa interactions of fermions and Higgs field, the Lagrangian of electroweak theory after spontaneous symmetry breaking can be expressed as

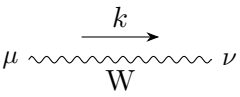
$$\begin{aligned} \mathcal{L}_{\text{EWH}} = & \bar{\psi}_f (i\not{\partial} - m_f) \psi_f + \frac{m_Z^2}{2} Z_\mu^2 + m_W^2 W_\mu^- W^{+\mu} + \frac{m_H^2}{2} H^2 + \frac{1}{2} (\partial_\mu H)^2 \\ & - \frac{1}{4} A_{\mu\nu} A^{\mu\nu} - \frac{1}{4} Z_{\mu\nu} Z^{\mu\nu} - \frac{1}{2} (\partial_\mu W_\nu^+ - \partial_\nu W_\mu^+) (\partial_\mu W^{-,\nu} - \partial_\nu W^{-,\mu}) \\ & + eQ\bar{\psi}_f A\psi_f + \frac{g}{c_w} \bar{\psi}_f \not{Z} \left(T^3 \frac{1 - \gamma_5}{2} - Qs_w^2 \right) \psi_f \\ & + \frac{g}{2\sqrt{2}} \left(\bar{\psi}_l W^- (1 - \gamma_5) \psi_{\nu_l} + \bar{\psi}_{\nu_l} W^+ (1 - \gamma_5) \psi_l \right. \\ & + \bar{\psi}_d W^- (1 - \gamma_5) \psi_u + \bar{\psi}_u W^+ (1 - \gamma_5) \psi_d \left. \right) \\ & + ie\frac{g}{g'} [Z^{\mu\nu} W_\mu^+ W_\nu^- - W_{\mu\nu}^+ Z^\mu W^{-,\nu} + W_{\mu\nu}^- Z^\mu W^{+,\nu}] \\ & + ie [A^{\mu\nu} W_\mu^+ W_\nu^- - W_{\mu\nu}^+ A^\mu W^{-,\nu} + W_{\mu\nu}^- A^\mu W^{+,\nu}] \\ & + \mathcal{L}_{\text{quartic}} + \mathcal{L}_{\text{HiggsInt}} + \mathcal{L}_{\text{fix}}. \end{aligned} \quad (\text{A.3})$$

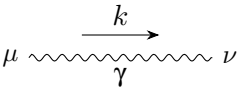
Here, $Z_{\mu\nu}$, $A_{\mu\nu}$, and $W_{\mu\nu}^{+,-}$ are defined analogously to $B_{\mu\nu}$ in Equation 2.7. The index f covers all fermions, l the three leptons electron, muon and tau, u sums over all up-type quarks and d over all down-type ones. The terms $\mathcal{L}_{\text{HiggsInt}}$ and $\mathcal{L}_{\text{quartic}}$, containing Higgs interactions and quartic couplings of gauge bosons, are not written in detail, as their resulting Feynman rules are not needed for the calculations in this thesis. The term \mathcal{L}_{fix} contains gauge fixing terms needed for a proper definition of the gauge boson propagators.

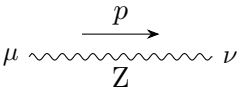
The Feynman rules for fermion and triple gauge boson interactions, as well as fermion and gauge boson propagators are presented below for an R_ξ gauge. Readers interested in a full set of Feynman rules for the Standard Model may have a look at Reference [72].

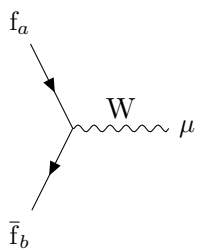
Selected Feynman Rules

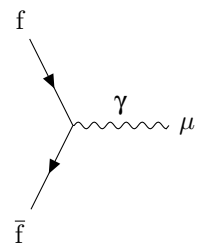
Fermion prop.:  $= \frac{i}{\not{p} - m_f + i\epsilon}$.

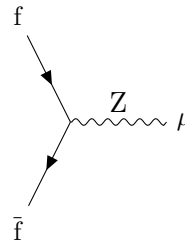
W boson prop.:  $= \frac{-i}{k^2 - m_W^2 + i\epsilon} \left[g^{\mu\nu} - (1 - \xi) \frac{k^\mu k^\nu}{k^2 - \xi m_W^2} \right]$.

Photon prop.:  $= -i \left[\frac{g^{\mu\nu}}{k^2 + i\epsilon} - (1 - \xi) \frac{k^\mu k^\nu}{(k^2)^2} \right]$.

Z boson prop.:  $= \frac{-i}{k^2 - m_Z^2 + i\epsilon} \left[g^{\mu\nu} - (1 - \xi) \frac{k^\mu k^\nu}{k^2 - \xi m_Z^2} \right]$.

CC interaction:  $= -i \frac{g}{2\sqrt{2}} (1 - \gamma_5) \gamma^\mu$.

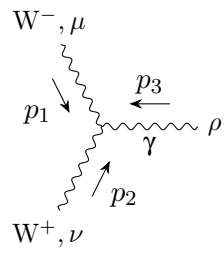
NC interactions:  $= -ieQ_f \gamma^\mu$.



A Feynman diagram showing a fermion line (f) and an antifermion line (f-bar) meeting at a vertex. A Z boson line (wavy) extends from the vertex to the right, labeled with index μ.

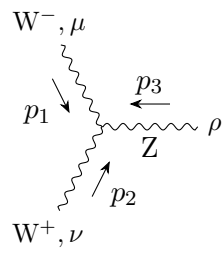
$$= -i \frac{g}{c_w} \left(T_f^3 \frac{1 - \gamma^5}{2} - Q_f s_w^2 \right) \gamma^\mu.$$

Triple gauge vertices:



A Feynman diagram for a triple gauge vertex. A W⁻ boson (wavy) enters from the top left with momentum p₁ and index μ. A W⁺ boson (wavy) enters from the bottom left with momentum p₂ and index ν. A photon (γ, wavy) exits to the right with momentum p₃ and index ρ.

$$= -e [(p_1 - p_2)^\rho g^{\mu\nu} + (p_2 - p_3)^\mu g^{\nu\rho} + (p_3 - p_1)^\nu g^{\rho\mu}].$$



A Feynman diagram for a triple gauge vertex. A W⁻ boson (wavy) enters from the top left with momentum p₁ and index μ. A W⁺ boson (wavy) enters from the bottom left with momentum p₂ and index ν. A Z boson (wavy) exits to the right with momentum p₃ and index ρ.

$$= -g c_w [(p_1 - p_2)^\rho g^{\mu\nu} + (p_2 - p_3)^\mu g^{\nu\rho} + (p_3 - p_1)^\nu g^{\rho\mu}].$$

A.2 Quantum Chromodynamics

The full Lagrangian of QCD reads

$$\mathcal{L}_{\text{QCD}} = \underbrace{\sum_{\text{quarks } q} \bar{\Psi}_q (i\not{D} - m_q) \Psi_q}_{=\mathcal{L}_{\text{quarks}}} - \underbrace{\frac{1}{4} G_{\mu\nu}^a G^{a,\mu\nu}}_{=\mathcal{L}_{\text{gauge}}} - \underbrace{\frac{1}{2\xi} (\partial^\mu A_\mu^a)^2}_{=\mathcal{L}_{\text{fix}}} - \underbrace{\bar{\eta}^a \partial^\mu \tilde{D}_\mu^{ab} \eta^b}_{=\mathcal{L}_{\text{ghost}}}, \quad (\text{A.4})$$

with the field strength tensor $G_{\mu\nu}$ and the covariant derivative D_μ defined as in Section 2.1.2. \tilde{D}_μ is the covariant derivative acting on a field in the adjoint representation, ξ is the gauge parameter and η names the ghost fields. By writing out the interaction terms explicitly, one gets

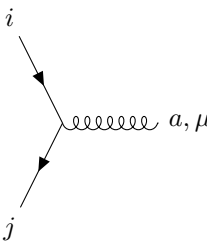
$$\begin{aligned} \mathcal{L}_{\text{QCD}} = & \underbrace{\sum_{\text{quarks } q} \bar{\Psi}_q (i\not{D} - m_q) \Psi_q + g_s \sum_{\text{quarks } q} A_\mu^a \bar{\Psi}_q \gamma^\mu t^a \Psi_q}_{=\mathcal{L}_{\text{quarks}}} \\ & - \underbrace{\frac{1}{4} (\partial_\mu A_\nu^a - \partial_\nu A_\mu^a)^2}_{=\mathcal{L}_{\text{gauge, abelian part}}} - \underbrace{\frac{1}{2\xi} (\partial^\mu A_\mu^a)^2}_{=\mathcal{L}_{\text{fix}}} \\ & - \underbrace{g_s f^{abc} (\partial_\mu A_\nu^a) A^{b,\mu} A^{c,\nu} - \frac{1}{4} g_s^2 (f^{abc} A_\mu^b A_\nu^c) (f^{ade} A_\mu^d A_\nu^e)}_{=\mathcal{L}_{\text{gauge, non-abelian part}}} \\ & - \underbrace{\bar{\eta}^a \partial^\mu \partial_\mu \eta^a - g_s f^{abc} (\partial^\mu \bar{\eta}^a) \eta^b A_\mu^c}_{=\mathcal{L}_{\text{ghost}}}. \end{aligned} \quad (\text{A.5})$$

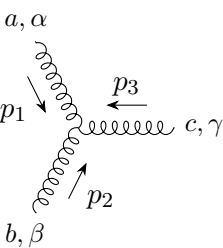
In the following, the Feynman rules for propagators, interactions and external lines of quarks and gluons are listed, where the indices i and j name the colour charges of quarks and thus go from 1 to 3, while a , b and c refer to the gluon fields and thus go from 1 to 8. Feynman rules involving ghosts are spared, as they are not needed for the calculations in this thesis.

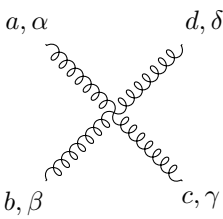
Selected Feynman Rules

Quark propagator: $i \xrightarrow{p} j = \frac{i\delta_{ij}}{\not{p} - m_q + i\varepsilon}.$

Gluon propagator: $a, \mu \xrightarrow{k} b, \nu = -i\delta_{ab} \left[\frac{g^{\mu\nu}}{k^2 + i\varepsilon} - (1 - \xi) \frac{k^\mu k^\nu}{(k^2)^2} \right].$

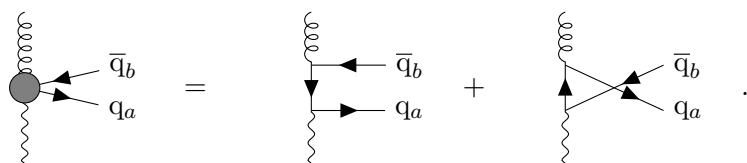
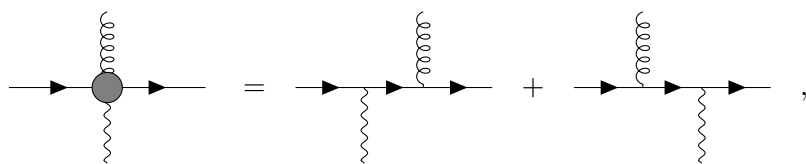
Quark-gluon vertex:  $= -ig_s t_{ji}^a \gamma^\mu.$

Three gluon vertex:  $= -g_s f^{abc} \left[(p_1 - p_2)^\gamma g^{\alpha\beta} + (p_2 - p_3)^\alpha g^{\beta\gamma} + (p_3 - p_1)^\beta g^{\gamma\alpha} \right].$

Four gluon vertex:  $= -ig_s^2 \left[f^{abe} f^{cde} (g^{\alpha\gamma} g^{\beta\delta} - g^{\alpha\delta} g^{\beta\gamma}) + f^{ace} f^{bde} (g^{\alpha\beta} g^{\gamma\delta} - g^{\alpha\delta} g^{\gamma\beta}) + f^{ade} f^{bce} (g^{\alpha\beta} g^{\delta\gamma} - g^{\alpha\gamma} g^{\delta\beta}) \right].$

B Notation in Feynman Diagrams

The diagrams shown in Figures 3.2, 3.3, 3.6, and 3.7 each comprise two kinds of diagrams, which is denoted by the grey circle. The explicit meaning of this notation is explained by the following diagrams:



C Colour Factors for the Two-Gluon Subprocesses

The colour factors $C^{(nm)}$ for the colour structure subamplitudes of the two-gluon subprocesses are given by the colour sums over the products of the colour structure tensors $\mathcal{T}^{(i)}$. In the following calculation, a and b denote the colour charges of the gluons, i and j the colour charges of the upper line quarks and k and l the colour charges of the lower line quarks. The relations used during the calculation are given by Equation 2.20.

$$\begin{aligned}
C^{(11)} &= \left(\mathcal{T}_{jilk}^{(1)ab} \right)^* \mathcal{T}_{jilk}^{(1)ab} \\
&= \frac{1}{4} \left(\delta_{lk} \left\{ t^b, t^a \right\}_{ij} \right) \left(\delta_{lk} \left\{ t^a, t^b \right\}_{ji} \right) \\
&= \frac{N}{4} \text{Tr} \left(2t^a t^b t^a t^b + 2t^b t^a t^a t^b \right) \\
&= \frac{N}{2} \left(-\frac{1}{4N} (N^2 - 1) + NC_F^2 \right) \\
&= \frac{NC_F}{2} \left(NC_F - \frac{1}{2} \right).
\end{aligned} \tag{C.1}$$

In the first step it was used that the generators t^a are hermitian, $(t^a)^\dagger = t^a$, which implies $\{t^a, t^b\}_{ji}^\dagger = \{t^b, t^a\}_{ij}$.

$$\begin{aligned}
C^{(22)} &= \left(\mathcal{T}_{jilk}^{(2)ab} \right)^* \mathcal{T}_{jilk}^{(2)ab} \\
&= \frac{1}{4} \left(\delta_{lk} [t^b, t^a]_{ij} \right) \left(\delta_{lk} [t^a, t^b]_{ji} \right) \\
&= \frac{N}{4} \text{Tr} \left(-2t^a t^b t^a t^b + 2t^b t^a t^a t^b \right) \\
&= \frac{N}{2} \left(\frac{1}{4N} (N^2 - 1) + NC_F^2 \right) \\
&= \frac{NC_F}{2} \left(NC_F + \frac{1}{2} \right).
\end{aligned} \tag{C.2}$$

$$\begin{aligned}
C^{(33)} &= \left(\mathcal{J}_{jilk}^{(3)ab} \right)^* \mathcal{J}_{jilk}^{(3)ab} \\
&= \left(t_{ji}^a \hat{t}_{lk}^b \right)^* \left(t_{ji}^a \hat{t}_{lk}^b \right) \\
&= t_{ij}^a \hat{t}_{kl}^b t_{ji}^a \hat{t}_{lk}^b \\
&= \hat{t}_{kl}^b t_{ij}^a t_{ji}^a \hat{t}_{lk}^b \\
&= \text{Tr} \left(t^a t^a \right) \text{Tr} \left(\hat{t}^b \hat{t}^b \right) \\
&= N^2 C_F^2,
\end{aligned} \tag{C.3}$$

where in the third step the commutativity of the two different colour structures was used.

$$\begin{aligned}
C^{(34)} &= \left(\mathcal{J}_{jilk}^{(3)ab} \right)^* \mathcal{J}_{jilk}^{(4)ab} \\
&= \left(t_{ji}^a \hat{t}_{lk}^b \right)^* \left(t_{ji}^b \hat{t}_{lk}^a \right) \\
&= \hat{t}_{kl}^b t_{ij}^a t_{ji}^b \hat{t}_{lk}^a \\
&= \text{Tr} \left(t^a t^b \right) \text{Tr} \left(\hat{t}^b \hat{t}^a \right) \\
&= \frac{1}{2} \delta_{ab} \frac{1}{2} \delta_{ab} \\
&= \frac{N C_F}{2}.
\end{aligned} \tag{C.4}$$

$$\begin{aligned}
C^{(15)} &= \left(\mathcal{J}_{jilk}^{(1)ab} \right)^* \mathcal{J}_{jilk}^{(5)ab} \\
&= \frac{1}{4} \left(\delta_{lk} \left\{ t^b, t^a \right\}_{ij} \right) \left(\delta_{ji} \left\{ \hat{t}^a, \hat{t}^b \right\}_{lk} \right) \\
&= \text{Tr} \left(t^b t^a \right) \text{Tr} \left(\hat{t}^a \hat{t}^b \right) \\
&= \frac{1}{4} \delta_{ab} \delta_{ab} \\
&= \frac{N C_F}{2}.
\end{aligned} \tag{C.5}$$

$$\begin{aligned}
C^{(16)} &= \left(\mathcal{J}_{jilk}^{(1)ab} \right)^* \mathcal{J}_{jilk}^{(6)ab} \\
&= \frac{1}{4} \left(\delta_{lk} \left\{ t^b, t^a \right\}_{ij} \right) \left(\delta_{ji} \left[\hat{t}^a, \hat{t}^b \right]_{lk} \right) \\
&= \text{Tr} \left(t^b t^a \right) \text{Tr} (0) \\
&= 0.
\end{aligned} \tag{C.6}$$

$C^{(26)} = C^{(62)}$ and $C^{(25)} = C^{(52)}$ can analogously be shown to give zero, as they also include the trace over a commutator.

List of Figures

2.1	All diagrams contributing to Bhaba scattering at LO (a) and some virtual correction diagrams (b)	14
2.2	Some example diagrams contributing to W boson production via vector boson fusion.	22
2.3	The three different channels for a $2 \rightarrow 2$ process defining the Mandelstam variables s , t and u	23
3.1	Schematic diagram of the operation sequence in VBFNLO [partially adapted from 47, p. 24].	28
3.2	All LO subprocesses that have contributions from colour structure 1.	29
3.3	Diagrams for the flavour combination $u D \rightarrow u U g l^- \bar{\nu}_l$	31
3.4	Leptonic tensors $\mathcal{L}^{\mu\nu}$ that produce the W^- final state observable.	31
3.5	Diagrams contributing to colour structures 1 and 2 for a two-gluon subprocess with W boson production as leptonic tensor.	35
3.6	Diagram types for the six-quark subprocesses for colour structure 1.	40
3.7	Diagram types for the six-quark subprocesses for colour structure 2.	40
3.8	Example diagram where collinear quarks cause a singularity in the t -channel photon propagator.	43
3.9	Virtual one-loop corrections to a line with two electroweak gauge bosons attached.	49
3.10	Additional non-abelian one-loop diagrams for a quark line coupling to a gluon and an electroweak current.	49
3.11	One-loop virtual corrections to a line with three gauge bosons attached.	50
4.1	Normalised difference R between dipole terms and squared real emission amplitude for small final gluon energies.	58
4.2	Normalised difference R for large rapidities of a final parton.	59
4.3	Normalised difference R for large rapidities of a final parton in the six-quark subprocesses with photon virtuality cut set to 30 GeV^2	60
4.4	Normalised difference between dipole terms and squared real emission amplitude for final state collinear singularities.	61
4.5	Test results for final state collinear singularities in the six-quark subprocesses of the Hjjj process.	62
4.6	Differential cross section of $W^+ \text{jjj}$ production as a function of the virtuality of the t -channel photon.	63
4.7	Schematic diagram for the process $pp \rightarrow W \text{jjjX} + p$	63

5.1	Transverse momentum distributions and respective K factors for W^+ jjj and W^- jjj production for the three highest p_T jets.	68
5.2	Rapidity distributions and respective K factors for W^+ jjj and W^- jjj production for the three highest p_T jets.	69
5.3	Distributions in dependence of the rapidity and angular separation between the two tagging jets for W^+ jjj production.	70
5.4	Differential cross section distributions indicating the relative position of the third jet to the tagging jets.	72
5.5	Differential cross section distributions of the normalised relative rapidity difference of the charged lepton with respect to the two tagging jets for W^+ jjj production.	73
5.6	Distribution of the differential cross section in dependence of the invariant mass of the two tagging jets for W^+ jjj production.	74
5.7	Total cross section and K factor for W^+ jjj production in dependence of different variations of renormalisation and factorisation scale around $\mu = p_{T,j_1}$	75
5.8	Total cross section and K factor for W^+ jjj production in dependence of simultaneous variation of renormalisation and factorisation scale around $\mu = p_{T,j_2}$, $\mu = 100$ GeV, and $\mu = p_{T,j_3}$	76
5.9	K factors for W^+ jjj production in comparison to those for W^- jjj production for one dynamic and one constant scale.	77
5.10	K factors and normalised differential NLO cross section distributions for W^+ jjj production in comparison to those for Hjjj production for $\mu_R = \mu_F = p_{T,j_1}$	79
5.11	K factors and normalised differential NLO cross section distributions for W^+ jjj production in comparison to those for Hjjj production for $\mu_R = \mu_F = 100$ GeV.	80
5.12	Normalised NLO and K factor distributions over the angular separation between the two tagging jets for W^+ jjj production in comparison to those for Hjjj production.	81
5.13	Normalised NLO and K factor distributions over the angular separation between the two tagging jets for Hjjj production with differing cuts on the transverse momentum of the Higgs boson.	82

List of Tables

2.1 Fermions of the Standard Model and their electroweak quantum numbers. . .	5
3.1 Flavour combinations for the real emission subprocesses with six external quarks.	39
3.2 Dipoles for $q_a(p_1) Q_c(p_2) \rightarrow q_b(p_3) Q_d(p_4) \bar{q}'_5(p_5) q'_6(p_6) W(P_W)$ processes and the corresponding Born kinematics.	46
3.3 Dipoles for $\bar{q}_a(p_1) \bar{Q}_c(p_2) \rightarrow \bar{q}_b(p_3) \bar{Q}_d(p_4) \bar{q}'_5(p_5) q'_6(p_6) W(P_W)$ processes and the corresponding Born kinematics.	47
5.1 All relevant cuts that are applied.	66
5.2 Full LO and NLO cross sections for four different scale choices and the parameters specified in Section 5.1.	67

Bibliography

The precluding quote of Albert Einstein originates from p. 315 of ‘Physik und Realität’, published in the *Journal of the Franklin Institute* (1936), **221**: pp. 313-347.

In this thesis, citations of the form [X, p. xx] were occasionally used, which refer to page xx of Reference X. In the case of articles that have been published in journals and are also available as e-print on arXiv, the page number refers to the arXiv e-print.

The Feynman diagrams displayed in this thesis were drawn using the L^AT_EX package TikZ-Feynman, see Reference [73].

1. POINCARÉ, HENRI: *The Value of Science*. New York: Dover Publications, 1958 (cit. on p. 1).
2. HAWKING, STEPHEN: *A Brief History of Time: From the Big Bang to Black Holes*. New York: Bantam Dell, 1988 (cit. on p. 1).
3. DALTON, JOHN: *A New System of Chemical Philosophy*. London: Henderson & Spalding, 1808 (cit. on p. 1).
4. RUTHERFORD, ERNEST: ‘The Scattering of α and β Particles by Matter and the Structure of the Atom’. *Phil. Mag. Ser. 6* (1911), **21** (125): pp. 669–688. DOI: [10.1080/14786440508637080](https://doi.org/10.1080/14786440508637080) (cit. on p. 1).
5. PLANCK, MAX: ‘Ueber das Gesetz der Energieverteilung im Normalspectrum’. *Annalen Phys.* (1901), **4** (4): pp. 553–563. DOI: [10.1002/andp.19013090310](https://doi.org/10.1002/andp.19013090310) (cit. on p. 1).
6. EINSTEIN, ALBERT: ‘Über einen die Erzeugung und Verwandlung des Lichtes betreffenden heuristischen Gesichtspunkt’. *Annalen Phys.* (1905), **17**: pp. 132–148. DOI: [10.1002/andp.19053220607](https://doi.org/10.1002/andp.19053220607) (cit. on p. 1).
7. ZWEIG, GEORGE: ‘An SU(3) model for strong interaction symmetry and its breaking. Version 2’. *Developments in the Quark Theory of Hadrons. Vol. 1. 1964 - 1978*. Ed. by LICHTENBERG, D.B. and SIMON PETER ROSEN. 1964: pp. 22–101 (cit. on pp. 1, 9).
8. GELL-MANN, MURRAY: ‘A Schematic Model of Baryons and Mesons’. *Phys. Lett.* (1964), **8** (3): pp. 214–215. DOI: [10.1016/S0031-9163\(64\)92001-3](https://doi.org/10.1016/S0031-9163(64)92001-3) (cit. on pp. 1, 5, 9).
9. BJORKEN, JAMES and EMMANUEL PASCHOS: ‘Inelastic Electron-Proton and γ -Proton Scattering and the Structure of the Nucleon’. *Phys. Rev.* (1969), **185** (5): pp. 1975–1982. DOI: [10.1103/PhysRev.185.1975](https://doi.org/10.1103/PhysRev.185.1975) (cit. on pp. 1, 9, 19).

10. FRITZSCH, HARALD, MURRAY GELL-MANN, and HEINRICH LEUTWYLER: ‘Advantages of the Color Octet Gluon Picture’. *Phys. Lett. B* (1973), **47** (4): pp. 365–368. DOI: [10.1016/0370-2693\(73\)90625-4](https://doi.org/10.1016/0370-2693(73)90625-4) (cit. on pp. 1, 9).
11. SALAM, ABDUS and JOHN WARD: ‘Weak and Electromagnetic Interactions’. *Nuovo Cim.* (1959), **11** (4): pp. 568–577. DOI: [10.1007/BF02726525](https://doi.org/10.1007/BF02726525) (cit. on pp. 1, 5).
12. WEINBERG, STEVEN: ‘A Model of Leptons’. *Phys. Rev. Lett.* (1967), **19** (21): pp. 1264–1266. DOI: [10.1103/PhysRevLett.19.1264](https://doi.org/10.1103/PhysRevLett.19.1264) (cit. on pp. 1, 5).
13. VAN DYCK, ROBERT, PAUL SCHWINBERG, and HANS DEHMELT: ‘New High-Precision Comparison of Electron and Positron g Factors’. *Phys. Rev. Lett.* (1987), **59** (1): pp. 26–29. DOI: [10.1103/PhysRevLett.59.26](https://doi.org/10.1103/PhysRevLett.59.26) (cit. on p. 1).
14. KAUL, ROMESH: ‘Naturalness and Electro-weak Symmetry Breaking’. (2008), arXiv: [0803.0381 \[hep-ph\]](https://arxiv.org/abs/0803.0381) (cit. on p. 2).
15. DIJKSTRA, CASPER: ‘Naturalness as a Reasonable Scientific Principle in Fundamental Physics’. (2019), arXiv: [1906.03036 \[physics.hist-ph\]](https://arxiv.org/abs/1906.03036) (cit. on p. 2).
16. EVANS, LYNDON and PHILIP BRYANT: ‘LHC Machine’. *JINST* (2008), **3**. DOI: [10.1088/1748-0221/3/08/S08001](https://doi.org/10.1088/1748-0221/3/08/S08001) (cit. on pp. 2, 83).
17. CHEN, XIN (On behalf of the ATLAS and CMS COLLABORATIONS): ‘Prospects of LHC Higgs Physics at the end of Run III’. *Proceedings, International Workshop on Future Linear Colliders 2016 (LCWS2016): Morioka, Iwate, Japan, December 05-09, 2016*. 2017. arXiv: [1703.07689 \[hep-ex\]](https://arxiv.org/abs/1703.07689) (cit. on p. 2).
18. ARNOLD, KEN et al.: ‘VBFNLO: A parton level Monte Carlo for processes with electroweak bosons’. *Comput. Phys. Commun.* (2009), **180**: pp. 1661–1670. DOI: [10.1016/j.cpc.2009.03.006](https://doi.org/10.1016/j.cpc.2009.03.006). arXiv: [0811.4559 \[hep-ph\]](https://arxiv.org/abs/0811.4559) (cit. on pp. 3, 25, 83).
19. ARNOLD, KEN et al.: ‘Release Note – Vbfno-2.6.0’. (2012), arXiv: [1207.4975 \[hep-ph\]](https://arxiv.org/abs/1207.4975) (cit. on pp. 3, 25, 83).
20. BAGLIO, JULIEN et al.: ‘VBFNLO: A parton level Monte Carlo for processes with electroweak bosons – Manual for Version 2.7.0’. (2011), arXiv: [1107.4038 \[hep-ph\]](https://arxiv.org/abs/1107.4038) (cit. on pp. 3, 25, 83).
21. BAGLIO, JULIEN et al.: ‘Release Note – VBFNLO 2.7.0’. (2014), arXiv: [1404.3940 \[hep-ph\]](https://arxiv.org/abs/1404.3940) (cit. on pp. 3, 25, 83).
22. CHATRCHYAN, SERGUEI et al. (CMS COLLABORATION): ‘Observation of a new boson at a mass of 125 GeV with the CMS experiment at the LHC’. *Phys. Lett. B* (2012), **716** (1): pp. 30–61. DOI: [10.1016/j.physletb.2012.08.021](https://doi.org/10.1016/j.physletb.2012.08.021). arXiv: [1207.7235 \[hep-ex\]](https://arxiv.org/abs/1207.7235) (cit. on p. 5).
23. AAD, GEORGES et al. (ATLAS COLLABORATION): ‘Observation of a new particle in the search for the Standard Model Higgs boson with the ATLAS detector at the LHC’. *Phys. Lett. B* (2012), **716** (1): pp. 1–29. DOI: [10.1016/j.physletb.2012.08.020](https://doi.org/10.1016/j.physletb.2012.08.020). arXiv: [1207.7214 \[hep-ex\]](https://arxiv.org/abs/1207.7214) (cit. on p. 5).
24. GLASHOW, SHELDON: ‘Partial-Symmetries of Weak Interactions’. *Nucl. Phys.* (1961), **22** (4): pp. 579–588. DOI: [10.1016/0029-5582\(61\)90469-2](https://doi.org/10.1016/0029-5582(61)90469-2) (cit. on p. 5).

-
25. SCHWARTZ, MATTHEW: *Quantum Field Theory and the Standard Model*. New York: Cambridge University Press, 2014 (cit. on pp. 6, 10).
 26. HIGGS, PETER: ‘Broken Symmetries and the Masses of Gauge Bosons’. *Phys. Rev. Lett.* (1964), **13** (16): pp. 508–509. DOI: [10.1103/PhysRevLett.13.508](https://doi.org/10.1103/PhysRevLett.13.508) (cit. on p. 7).
 27. HIGGS, PETER: ‘Broken Symmetries, Massless Particles and Gauge Fields’. *Phys. Lett.* (1964), **12** (2): pp. 132–133. DOI: [10.1016/0031-9163\(64\)91136-9](https://doi.org/10.1016/0031-9163(64)91136-9) (cit. on p. 7).
 28. ENGLERT, FRANCOIS and ROBERT BROUT: ‘Broken Symmetry and the Mass of Gauge Vector Mesons’. *Phys. Rev. Lett.* (1964), **13** (9): pp. 321–323. DOI: [10.1103/PhysRevLett.13.321](https://doi.org/10.1103/PhysRevLett.13.321) (cit. on p. 7).
 29. GURALNIK, GERALD, CARL HAGEN, and TOM KIBBLE: ‘Global Conservation Laws and Massless Particles’. *Phys. Rev. Lett.* (1964), **13** (20): pp. 585–587. DOI: [10.1103/PhysRevLett.13.585](https://doi.org/10.1103/PhysRevLett.13.585) (cit. on p. 7).
 30. HAN, MOO-YOUNG and YOICHIRO NAMBU: ‘Three-Triplet Model with Double $SU(3)$ Symmetry’. *Phys. Rev.* (1965), **139** (4B): pp. 1006–1010. DOI: [10.1103/PhysRev.139.B1006](https://doi.org/10.1103/PhysRev.139.B1006) (cit. on p. 9).
 31. PESKIN, MICHAEL and DANIEL SCHROEDER: *An Introduction to Quantum Field Theory*. Boulder, Col.: Westview Press, 1995 (cit. on pp. 10–12, 14, 19).
 32. CHENG, TA-PEI and LING-FONG LI: *Gauge Theory of Elementary Particle Physics*. Oxford: Clarendon Press, 1984 (cit. on pp. 10, 18).
 33. WICK, GIAN-CARLO: ‘The Evaluation of the Collision Matrix’. *Phys. Rev.* (1950), **80** (2): pp. 268–272. DOI: [10.1103/PhysRev.80.268](https://doi.org/10.1103/PhysRev.80.268) (cit. on p. 12).
 34. LEHMANN, HARRY, KURT SYMANZIK, and WOLFHART ZIMMERMANN: ‘Zur Formulierung quantisierter Feldtheorien’. *Nuovo Cim.* (1955), **1** (1): pp. 205–225. DOI: [10.1007/BF02731765](https://doi.org/10.1007/BF02731765) (cit. on p. 13).
 35. TANABASHI, MASAHARU et al. (PARTICLE DATA GROUP): ‘The Review of Particle Physics’. *Phys. Rev. D* (2018), **98**. DOI: [10.1103/PhysRevD.98.030001](https://doi.org/10.1103/PhysRevD.98.030001) (cit. on p. 15).
 36. ’T HOOFT, GERARD and MARTINUS VELTMAN: ‘Regularization and Renormalization of Gauge Fields’. *Nucl. Phys. B* (1972), **44** (1): pp. 189–213. DOI: [10.1016/0550-3213\(72\)90279-9](https://doi.org/10.1016/0550-3213(72)90279-9) (cit. on p. 16).
 37. CALLAN Jr., CURTIS: ‘Broken Scale Invariance in Scalar Field Theory’. *Phys. Rev. D* (1970), **2** (8): pp. 1541–1547. DOI: [10.1103/PhysRevD.2.1541](https://doi.org/10.1103/PhysRevD.2.1541) (cit. on p. 17).
 38. SYMANZIK, KURT: ‘Small Distance Behavior in Field Theory and Power Counting’. *Commun. Math. Phys.* (1970), **18** (3): pp. 227–246. DOI: [10.1007/BF01649434](https://doi.org/10.1007/BF01649434) (cit. on p. 17).
 39. KINOSHITA, TOICHIRO: ‘Mass Singularities of Feynman Amplitudes’. *J. Math. Phys.* (1962), **3** (4): pp. 650–677. DOI: [10.1063/1.1724268](https://doi.org/10.1063/1.1724268) (cit. on p. 19).

40. LEE, TSUNG-DAO and MICHAEL NAUENBERG: ‘Degenerate Systems and Mass Singularities’. *Phys. Rev.* (1964), **133** (6B): pp. 1549–1562. DOI: [10.1103/PhysRev.133.B1549](https://doi.org/10.1103/PhysRev.133.B1549) (cit. on p. 19).
41. GRIBOV, VLADIMIR and LEV LIPATOV: ‘Deep Inelastic ep-Scattering In Perturbation Theory’. *Sov. J. Nucl. Phys.* (1972), **15**: pp. 438–450. [Original: *Yad. Fiz.* (1972), **15** (4): pp. 781-807] (cit. on p. 19).
42. ALTARELLI, GUIDO and GIORGIO PARISI: ‘Asymptotic Freedom in Parton Language’. *Nucl. Phys. B* (1977), **126** (2): pp. 298–318. DOI: [10.1016/0550-3213\(77\)90384-4](https://doi.org/10.1016/0550-3213(77)90384-4) (cit. on p. 19).
43. DOKSHITZER, YURI: ‘Calculation of the Structure Functions for Deep Inelastic Scattering and e^+e^- Annihilation by Perturbation Theory in Quantum Chromodynamics.’ *Sov. Phys. JETP* (1977), **46**: pp. 641–653. [Original: *Zh. Eksp. Teor. Fiz.* (1977), **73**: pp. 1216-1240] (cit. on p. 19).
44. CATANI, STEFANO and MICHAEL SEYMOUR: ‘A General Algorithm for Calculating Jet Cross Sections in NLO QCD’. *Nucl. Phys. B* (1997), **485** (1-2): pp. 291–419. DOI: [10.1016/S0550-3213\(96\)00589-5](https://doi.org/10.1016/S0550-3213(96)00589-5). arXiv: [hep-ph/9605323](https://arxiv.org/abs/hep-ph/9605323) [[hep-ph](#)]. [Erratum: *Nucl. Phys. B* (1998), **510** (1-2): pp. 503-504] (cit. on pp. 20–22, 42–44, 53, 83).
45. OLEARI, CARLO and DIETER ZEPPENFELD: ‘QCD corrections to electroweak $l\nu_l jj$ and $l^+l^- jj$ production’. *Phys. Rev. D* (2004), **69**. DOI: [10.1103/PhysRevD.69.093004](https://doi.org/10.1103/PhysRevD.69.093004). arXiv: [hep-ph/0310156](https://arxiv.org/abs/hep-ph/0310156) [[hep-ph](#)] (cit. on pp. 23, 44, 62).
46. LEPAGE, G. PETER: ‘A New Algorithm for Adaptive Multidimensional Integration’. *J. Comput. Phys.* (1978), **27** (2): pp. 192–203. DOI: [10.1016/0021-9991\(78\)90004-9](https://doi.org/10.1016/0021-9991(78)90004-9) (cit. on p. 26).
47. SCHLIMPERT, OLIVER: ‘Anomale Kopplungen bei der Streuung schwacher Eichbosonen’. MA thesis. Karlsruhe: Karlsruhe Institute of Technology, Feb. 2013 (cit. on p. 28).
48. HAGIWARA, KAORU and DIETER ZEPPENFELD: ‘Amplitudes for Multiparton Processes Involving a Current at e^+e^- , $e^\pm p$, and Hadron Colliders’. *Nucl. Phys.* (1989), **B313**: pp. 560–594. DOI: [10.1016/0550-3213\(89\)90397-0](https://doi.org/10.1016/0550-3213(89)90397-0) (cit. on p. 28).
49. MURAYAMA, HITOSHI, ISAMU WATANABE, and KAORU HAGIWARA: *HELAS: HELicity Amplitude Subroutines for Feynman Diagram Evaluations*. Tech. rep. KEK-91-11. Japan: National Laboratory for High Energy Physics, Jan. 1992 (cit. on p. 31).
50. FIGY, TERRANCE, VERA HANKELE, and DIETER ZEPPENFELD: ‘Next-to-leading order QCD corrections to Higgs plus three jet production in vector-boson fusion’. *JHEP* (2008), **2**. DOI: [10.1088/1126-6708/2008/02/076](https://doi.org/10.1088/1126-6708/2008/02/076). arXiv: [0710.5621](https://arxiv.org/abs/0710.5621) [[hep-ph](#)] (cit. on pp. 37, 60, 78, 84).
51. FIGY, TERRANCE: ‘NLO QCD Corrections to the Jet Activity in Higgs Boson Production via Vector-Boson Fusion’. PhD thesis. University of Wisconsin-Madison, 2006 (cit. on pp. 44, 53, 60, 78, 84).

-
52. CAMPANARIO, FRANCISCO: ‘Towards $pp \rightarrow VVjj$ at NLO QCD: Bosonic contributions to triple vector boson production plus jet’. *JHEP* (2011), **10**. DOI: [10.1007/JHEP10\(2011\)070](https://doi.org/10.1007/JHEP10(2011)070). arXiv: [1105.0920](https://arxiv.org/abs/1105.0920) [[hep-ph](#)] (cit. on pp. 50, 51, 56, 83).
 53. PASSARINO, GIAMPERO and MARTINUS VELTMAN: ‘One-Loop Corrections for e^+e^- Annihilation Into $\mu^+\mu^-$ in the Weinberg Model’. *Nucl. Phys. B* (1979), **160** (1): pp. 151–207. DOI: [10.1016/0550-3213\(79\)90234-7](https://doi.org/10.1016/0550-3213(79)90234-7) (cit. on p. 51).
 54. BANACHIEWICZ, TADEUSZ: ‘Etudes d’analyse pratique’. *Bull. Acad. Pol. Ser. A* (1938), pp. 393–404 (cit. on p. 51).
 55. CROUT, PRESCOTT: ‘A Short Method for Evaluating Determinants and Solving Systems of Linear Equations With Real or Complex Coefficients’. *Trans. Amer. Inst. Elec. Eng.* (1941), **60**: pp. 1235–1240. DOI: [10.1109/T-AIEE.1941.5058258](https://doi.org/10.1109/T-AIEE.1941.5058258) (cit. on p. 51).
 56. DENNER, ANSGAR and STEFAN DITTMAYER: ‘Reduction schemes for one-loop tensor integrals’. *Nucl. Phys. B* (2006), **734** (1-2): pp. 62–115. DOI: [10.1016/j.nuclphysb.2005.11.007](https://doi.org/10.1016/j.nuclphysb.2005.11.007). arXiv: [hep-ph/0509141](https://arxiv.org/abs/hep-ph/0509141) [[hep-ph](#)] (cit. on p. 51).
 57. KERNER, MATTHIAS: ‘Next-to-Leading Order QCD Corrections to Vector Boson Pair Production in Association with two Jets at the LHC’. PhD thesis. Karlsruhe Institute of Technology, 2014 (cit. on p. 53).
 58. STELZER, TIMOTHY and WILLIAM LONG: ‘Automatic generation of tree level helicity amplitudes’. *Comput. Phys. Commun.* (1994), **81** (3): pp. 357–371. DOI: [10.1016/0010-4655\(94\)90084-1](https://doi.org/10.1016/0010-4655(94)90084-1). arXiv: [hep-ph/9401258](https://arxiv.org/abs/hep-ph/9401258) [[hep-ph](#)] (cit. on pp. 55, 84).
 59. ENGEMANN, AMON: ‘Next-To-Leading Order QCD Corrections to Z Boson Production via Vector-Boson Fusion in Association with Three Jets’. MA thesis. Karlsruhe: Karlsruhe Institute of Technology, Sept. 2016 (cit. on p. 56).
 60. BAUR, ULRICH, JOZEF VERMASEREN, and DIETER ZEPPENFELD: ‘Electroweak vector boson production in high-energy ep collisions’. *Nucl. Phys. B* (1992), **375** (1): pp. 3–44. DOI: [10.1016/0550-3213\(92\)90332-6](https://doi.org/10.1016/0550-3213(92)90332-6) (cit. on p. 62).
 61. HAGIWARA, KAORU, DIETER ZEPPENFELD, and SACHIO KOMAMIYA: ‘Excited Lepton Production at LEP and HERA’. *Z. Phys. C* (1985), **29** (1): pp. 115–122. DOI: [10.1007/BF01571391](https://doi.org/10.1007/BF01571391) (cit. on p. 62).
 62. ZEPPENFELD, DIETER: *Private communication* (cit. on pp. 62, 63).
 63. AABOUD, MORAD et al. (ATLAS COLLABORATION): ‘Measurements of electroweak Wjj production and constraints on anomalous gauge couplings with the ATLAS detector’. *Eur. Phys. J. C* (2017), **77** (7): p. 474. DOI: [10.1140/epjc/s10052-017-5007-2](https://doi.org/10.1140/epjc/s10052-017-5007-2). arXiv: [1703.04362](https://arxiv.org/abs/1703.04362) [[hep-ex](#)] (cit. on p. 65).
 64. SIRUNYAN, ALBERT et al. (CMS COLLABORATION): ‘Measurement of electroweak production of a W boson in association with two jets in proton-proton collisions at $\sqrt{s} = 13$ TeV’. (2019), arXiv: [1903.04040](https://arxiv.org/abs/1903.04040) [[hep-ex](#)] (cit. on p. 65).

65. CATANI, STEFANO, YURI DOKSHITZER, and BRYAN WEBBER: ‘The k_{\perp} -clustering algorithm for jets in deep inelastic scattering and hadron collisions’. *Phys. Lett. B* (1992), **285** (3): pp. 291–299. DOI: [10.1016/0370-2693\(92\)91467-N](https://doi.org/10.1016/0370-2693(92)91467-N) (cit. on p. 65).
66. ELLIS, STEPHEN and DAVISON SOPER: ‘Successive combination jet algorithm for hadron collisions’. *Phys. Rev. D* (1993), **48** (7): pp. 3160–3166. DOI: [10.1103/PhysRevD.48.3160](https://doi.org/10.1103/PhysRevD.48.3160). arXiv: [hep-ph/9305266](https://arxiv.org/abs/hep-ph/9305266) [[hep-ph](#)] (cit. on p. 65).
67. CATANI, STEFANO, YURI DOKSHITZER, MICHAEL SEYMOUR, and BRYAN WEBBER: ‘Longitudinally-invariant k_{\perp} -clustering algorithms for hadron-hadron collisions’. *Nucl. Phys. B* (1993), **406** (1-2): pp. 187–224. DOI: [10.1016/0550-3213\(93\)90166-M](https://doi.org/10.1016/0550-3213(93)90166-M) (cit. on p. 65).
68. BLAZEY, GERALD et al.: ‘Run II Jet Physics’. *QCD and weak boson physics in Run II. Proceedings, Batavia, USA, March 4-6, June 3-4, November 4-6, 1999*. 2000: pp. 47–77. arXiv: [hep-ex/0005012](https://arxiv.org/abs/hep-ex/0005012) [[hep-ex](#)] (cit. on p. 65).
69. PUMPLIN, JONATHAN et al.: ‘New Generation of Parton Distributions with Uncertainties from Global QCD Analysis’. *JHEP* (2002), **7**. DOI: [10.1088/1126-6708/2002/07/012](https://doi.org/10.1088/1126-6708/2002/07/012). arXiv: [hep-ph/0201195](https://arxiv.org/abs/hep-ph/0201195) [[hep-ph](#)] (cit. on p. 65).
70. LAI, HUNG-LIANG et al.: ‘New parton distributions for collider physics’. *Phys. Rev. D* (2010), **82**. DOI: [10.1103/PhysRevD.82.074024](https://doi.org/10.1103/PhysRevD.82.074024). arXiv: [1007.2241](https://arxiv.org/abs/1007.2241) [[hep-ph](#)] (cit. on p. 65).
71. DAWSON, SALLY: ‘The Effective W Approximation’. *Nucl. Phys. B* (1985), **249** (1): pp. 42–60. DOI: [10.1016/0550-3213\(85\)90038-0](https://doi.org/10.1016/0550-3213(85)90038-0) (cit. on p. 78).
72. ROMAÑO, JORGE and JOÃO SILVA: ‘A Resource for Signs and Feynman Diagrams of the Standard Model’. *Int. J. Mod. Phys. A* (2012), **27** (26). DOI: [10.1142/S0217751X12300256](https://doi.org/10.1142/S0217751X12300256). arXiv: [1209.6213](https://arxiv.org/abs/1209.6213) [[hep-ph](#)] (cit. on p. 88).
73. ELLIS, JOSHUA: ‘TikZ-Feynman: Feynman diagrams with TikZ’. *Comput. Phys. Commun.* (2017), **210**: pp. 103–123. DOI: [10.1016/j.cpc.2016.08.019](https://doi.org/10.1016/j.cpc.2016.08.019). arXiv: [1601.05437](https://arxiv.org/abs/1601.05437) [[hep-ph](#)] (cit. on p. 103).

Acknowledgements

This thesis would not have come about if Prof. Dr. Dieter Zeppenfeld had not given me the opportunity to work on this topic. I am very grateful for this opportunity and would further like to thank him very much for readily providing professional advice at any time.

I would like to extend my thanks to our working group for sharing useful ideas and inspiration during our meetings. My special thanks in this regard go to Heiko Schäfer-Siebert for introducing me to the program VBFNLO and to Dr. Seraina Glaus for proofreading this thesis.

Thanks to the whole institute for always being friendly and supportive. The interesting and sometimes amusing discussions in the master students' room were very refreshing, thanks for that to my office mates Jannis, David, Tigran, ...

... and Tizian Römer, whom I, besides this, owe much more gratitude. I would only have gained a fraction of my understanding of Quantum Field Theory if it had not been for the endless discussions we had. He proofread my thesis, giving me plenty of constructive and invaluable comments. On top of that, he was also a great emotional support in tough times I encountered during the work done for this thesis. Thank you!

Da diese Arbeit den Abschluss meines Studiums markiert, möchte ich an dieser Stelle auch meinen Großeltern, meinen Eltern sowie meinem Bruder danken, die immer überzeugt waren, dass ich alle Ziele, die ich mir setze, erreichen und alle Schwierigkeiten erfolgreich meistern würde. Damit, sowie durch ihre bedingungslose Unterstützung bei allem, was ich mir vornehme, haben sie mir den Weg meiner akademischen Ausbildung geebnet.

